Terahertz Field Enhancement by Optimized Coupling and Adiabatic Tapering

by

Robert Levi Smith
B.Sc., University of Victoria, 2011

A Thesis Submitted in Partial Fulfillment of the
Requirements for the Degree of

MASTER OF APPLIED SCIENCE

in the Department of Electrical and Computer Engineering

Terahertz Field Enhancement by Optimized Coupling and Adiabatic Tapering

by

Robert Levi Smith
B.Sc., University of Victoria, 2011

Supervisory Committee

Dr. Thomas Darcie, Supervisor
(Department of Electrical and Computer Engineering)

Dr. Jens Bornemann, Departmental Member
(Department of Electrical and Computer Engineering)

Supervisory Committee

Dr. Thomas Darcie, Supervisor
(Department of Electrical and Computer Engineering)

Dr. Jens Bornemann, Departmental Member
(Department of Electrical and Computer Engineering)

ABSTRACT

Waveguides are desirable components for energy transmission throughout the electromagnetic spectrum. This thesis experimentally examines a thick slot waveguide for THz guiding and field enhancement. The waveguide is machined from planar copper sheets using the novel technique of femtosecond laser micromachining. In-plane photoconductive THz coupling to a thick slot waveguide is demonstrated using Discontinuous Galerkin Time Domain (DGTD) simulation. The results reveal positive implications for broadband low-loss/dispersion transmission lines up to 1.5 THz.

Contents

List of Figures

ACKNOWLEDGEMENTS

I would like to thank:

My family, friends, and all others who are special to me for supporting me throughout my studies

My supervisor, Ted Darcie for mentoring, support, encouragement, and patience.

My colleagues Jinye (James) Zhang, Afshin Jooshesh, Barmak Heshmat, and Hamid Pahlevaninezhad for many interesting and relevant discussions regarding THz.

Collaborators Dr. Thomas Tiedje's group (Vahid Bahrami Yekta and Mostafa Masnadi Shirazi) for their work growing LT-GaAs samples and many valuable conversations.

Dr. Martin Jun's group (Farid Ahmed and Max Rukosuyev) for their work laser machining and micromachining my samples.

NSERC This work was supported by funding from the Natural Science and Engineering Research Council (NSERC) Canada.

Tl'etinqox-T'in government for helping support me with my education.

DEDICATION

I would like to dedicate this to everyone special to me. I wouldn't have accomplished this without you all.

Acronyms

AR Anti-reflection. 12, 14, 48, 54

CCD Charge Coupled Device. 59

CPS Coplanar Strip. 29–37, 39–41, 47, 49, 52, 54

CW Continuous Wave. 6, 7, 10, 15, 39, 50, 54

DC Direct Current. 47, 48

DI Deionized. 58

EBL Electron Beam Lithography. 58

FEM Finite Element Method. 27, 29, 30, 32, 35–37, 40, 52

FFT Fast Fourier Transform. 1, 2, 62

FIB Focus Ion Beam. 58

GVD Group Velocity Dispersion. 21

HRFZ-Si High Resistivity Float Zone Silicon. 5, 10, 43, 44

HT-GaAs High Temperature Grown Gallium Arsenide. 58

Hz Hertz. 1

LT-GaAs Low Temperature Grown Gallium Arsenide. 5, 9, 48, 57–60

MBE Molecular Beam Epitaxy. 5, 58

MoM Method of Moments. 55

PCA Photoconductive Antenna. 5–7, 10, 12, 42–44, 46, 47, 64

PEC Perfect Electric Conductor. 29

PMMA Poly(methyl methacrylate). 48, 59

PPWG Parallel Plate Waveguide. 21, 22

PSD Phase Sensitive Detector. 61

RTA Rapid Thermal Annealer. 58

SI-GaAs Semi-insulating Gallium Arsenide. 5, 9, 58

SL Slotline. 25, 34–37

SNR Signal to Noise Ratio. 61

TE Transverse Electric. 18, 20, 21, 24–26, 28, 34

TEM Transverse Electromagnetic. 17, 19–23, 40, 52

THz Terahertz. 1, 2, 4–10, 12, 15, 16, 20, 24, 25, 31, 32, 37, 39, 42–45, 47–50, 52, 54, 56–60, 64, 65

THz-TDS Terahertz Time Domain Spectroscopy. 1, 2, 4, 9, 15, 56, 63, 65

TIR Total Internal Reflection. 24

TM Transverse Magnetic. 18, 20, 21, 24

UV Ultraviolet. 57, 58

Chapter 1

Introduction

The oscillatory nature of waves is used to explain many physical interactions such as sound, the ocean tide, light, and radio communications. Light and radio communications are commonly analyzed in terms of the electromagnetic spectrum. Visible light wavelengths range from 380nm to 740nm and radio communications range from 1mm to an infinite distance.

This thesis focuses on a region in the electromagnetic spectrum called the THz gap. The THz gap is commonly defined as the range of frequencies between 0.3×10^{12} Hertz (Hz) and 10×10^{12} Hz. This THz gap is inaccessible by decreasing the optical frequencies or increasing electrical frequencies primarily due to material limitations.

The goal of this thesis is to evaluate in-plane coupling to a thick slot waveguide (Section 4). This technique offers advantages such as low-loss and minimal dispersion in comparison to conventional Terahertz Time Domain Spectroscopy (THz-TDS) which utilizes a radiating Photoconductive Antenna (PCA).

1.1 Applications

The main application for THz waves is chemical analysis using a technique called Terahertz Time Domain Spectroscopy (THz-TDS). Using THz-TDS, solid/gas phase chemicals can be analyzed by transmitting a THz pulse through a sample material. The transmitted pulse is detected and the spectral response is obtained by applying the Fast Fourier Transform (FFT). Figure 1.1 plots a typical THz-TDS measurement for water vapor, Figure 1.1a illustrates the detected temporal response, and the Figure 1.1b plots the spectral response obtained by applying the FFT. In Figure

1.1b the sharp dips for the sample measurement correspond to the various rotational absorption lines of water vapor.

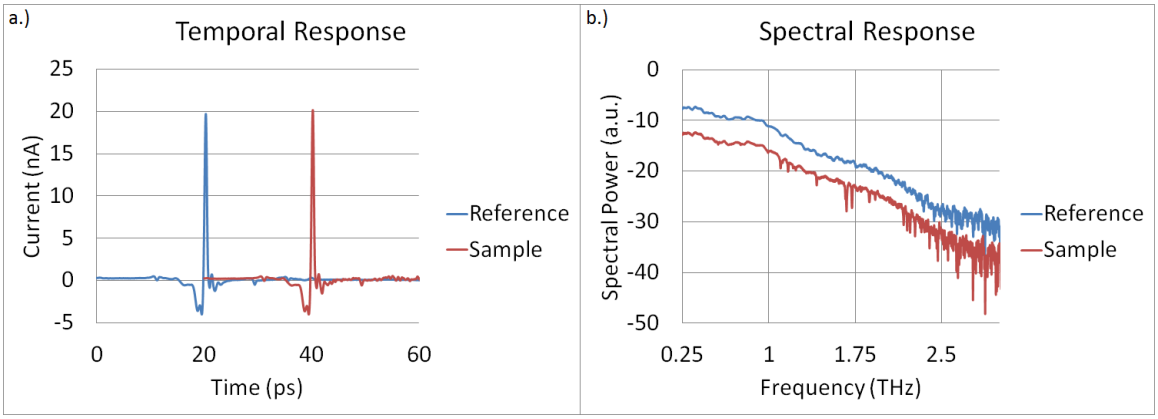

Figure 1.1: Experimental THz-TDS sample measurement a.) detected THz pulse with/without sample b.) FFT of the detected THz pulse with/without samples

Key properties of THz-TDS are: quick measurement times (<30 seconds), transmissive and reflective absorption measurements, and coherent detection of THz E-field. Coherent detection allows for the measurement of the complex propagation constant (γ); hence, the material attenuation and dielectric constant can be obtained.

In conventional THz-TDS, a THz beam which is radiated by a PCA is directed through a sample material. This thesis will focus on an unconventional method of THz-TDS which uses the concept of in-plane coupling to a thick slot waveguide. This method allows for low-loss, low-dispersion, and high sensitivity measurements.

1.2 Agenda

Chapter 2 describes the engineering techniques which are used for THz waveguide engineering.

Chapter 3 is a copy of a published paper [1] which describes antenna coupling to a thick slot waveguide and provides experimental and complementary simulation results.

Chapter 4 describes in-plane coupling to a thick slot waveguide and provides simulations which are used for constructing the physical waveguide. Transient simulations are evaluated for the entire structure to give insight into future experimental results.

Chapter 2

Terahertz Engineering

THz waves and guiding mechanisms can be analyzed using a combination of existing microwave and optical engineering techniques. This section introduces concepts which are complementary to the scope of this thesis. THz generation and detection are discussed to provide the reader with an understanding of photoconductive THz components. A brief introduction to molecular spectroscopy is provided to familiarize the reader with the principal THz-TDS application. Various waveguides are discussed from a microwave engineering prospective to provide the necessary background information. Finally optical engineering concepts are discussed for the THz ($\lambda \approx 300\mu m$) and optical ($\lambda \approx 0.78\mu m$) regions.

2.1 Terahertz Generation and Detection

THz waves can be generated using a number of methods: photoconductive switching, photoconductive mixing, difference frequency generation, far-IR gas lasers, microwave frequency multiplication, backward wave oscillator, free-electron laser, and quantum cascade lasers. Each method has its benefits (typically high output power at a single frequency) but the price can vary substantially - from a couple thousand of dollars for the photoconductive methods, to millions of dollars for free-electron lasers. For the low-cost reason, this thesis will focus on enhancing and guiding the THz field generated and detected by photoconductive switching.

2.1.1 Photoconductive Antennas

Figure 2.1 illustrates a typical Photoconductive Antenna (PCA). In principle PCAs are simple structures. They consist of a metalization deposited on a photoconductive substrate coupled to a THz lens. The substrate material is selected such that photo-excited carriers can trap in sub-picosecond time scales corresponding to THz frequencies. A common substrate material is Low Temperature Grown Gallium Arsenide (LT-GaAs) which is grown by Molecular Beam Epitaxy (MBE) on a Semi-insulating Gallium Arsenide (SI-GaAs) base substrate.

The metalization is used to apply an electric field, which is required to accelerate photo-carriers generated in the active area. The metalization arms extending into the active area (very short dipole arms) radiate a broad range of frequencies. Figure 2.1 illustrates a simple dipole PCA, although, to note, many other designs are viable such as a bow-tie and log-spiral PCAs.

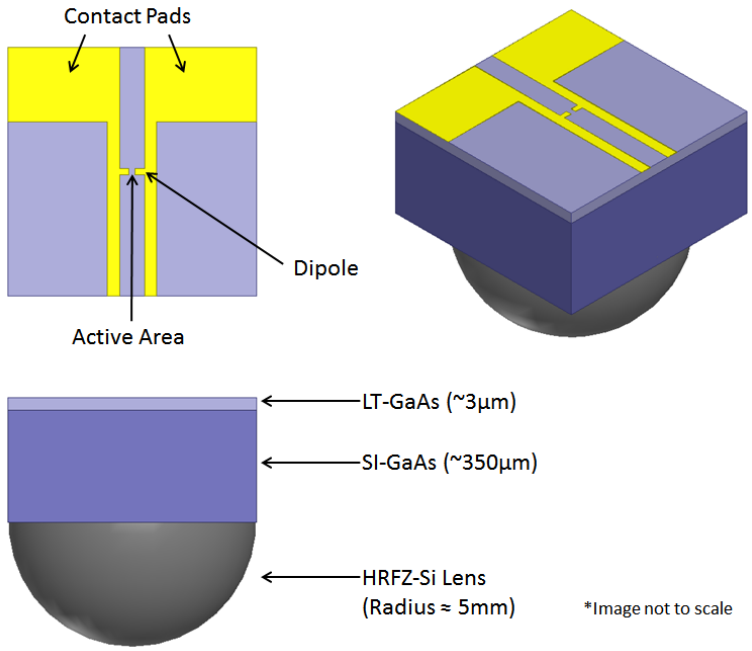

Figure 2.1: Illustration of a THz PCA

The High Resistivity Float Zone Silicon (HRFZ-Si) lens is not related to THz generation, but it has significant impact on the efficiency of the PCA (Figure 2.2). The lens is constructed of HRFZ-Si for two reasons: first, HRFZ-Si has relatively low-loss at THz frequencies; second, HRFZ-Si and SI-GaAs have similar refractive

indices, which minimizes the reflection at the material interface.

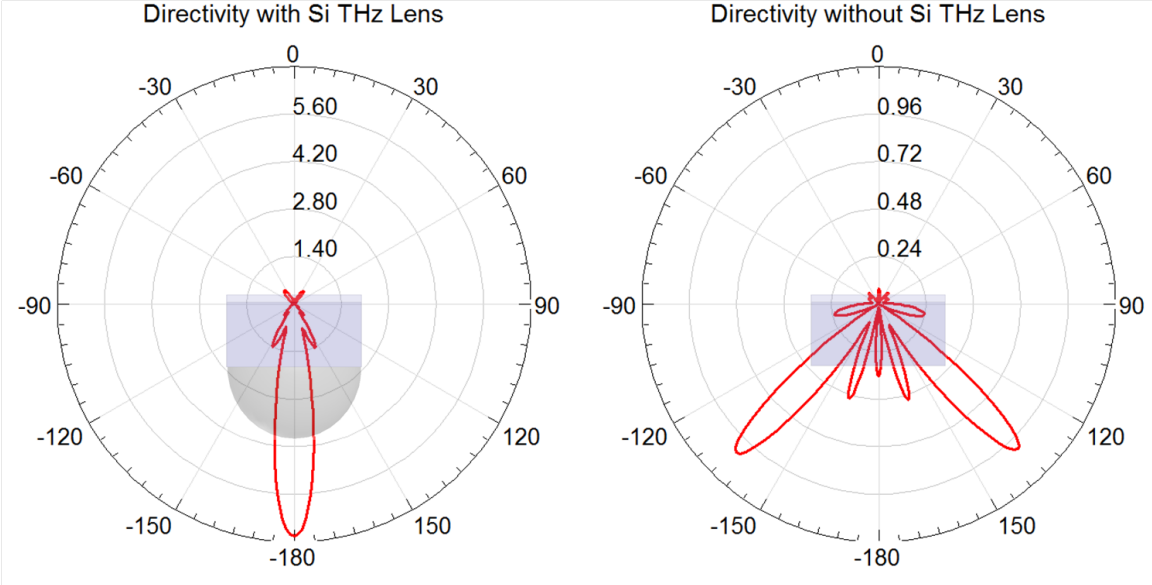

Figure 2.2: Radiation pattern for a PCA with and without a THz lens, obtained with FEM simulation [2]

The HRFZ-Si lens focuses the THz beam but its primary purpose is to allow the THz wave to escape the substrate. The LT-GaAs substrate has a high refractive index ($n \approx 3.6$), which, according to Snell's Law results in a critical angle of $\theta_c = sin^{-1}(1/3.6) \approx 16°$ at the dielectric/air interface. Due to the divergent nature of small dipole's only a small amount ($\approx 4\%$) of THz radiation can escape the substrate and the rest is bound by Total Internal Reflection (TIR). A HRFZ-Si lens ensures that the majority of radiation can escape by altering the incident ray angle at the dielectric/air interface.

Photoconductive Mixing

Photoconductive mixing is the process of generating a Continuous Wave (CW) THz signal. CW THz is generated by mixing two lasers, ν_1 and ν_2, separated by nanometer-scale wavelengths, $\Delta\lambda$, and focusing the combined beam onto the active area of a PCA. Optimal mixing occurs when the spatial distribution and polarization state of the two lasers are identical [3]. Figure 2.3 illustrates a standard photomixer.

$$f_{beat} = \Delta\nu = \frac{c\Delta\lambda}{\left(\lambda_c - \frac{\Delta\lambda}{2}\right)\left(\lambda_c + \frac{\Delta\lambda}{2}\right)} = \frac{c|\lambda_1 - \lambda_2|}{\lambda_1\lambda_2}.$$

where c is the speed of light in a vacuum. For example, to get a beat frequency of 1 THz at center wavelength of $\lambda_c = 854nm$ a wavelength separation of $\Delta\lambda = 2.431nm$ is required.

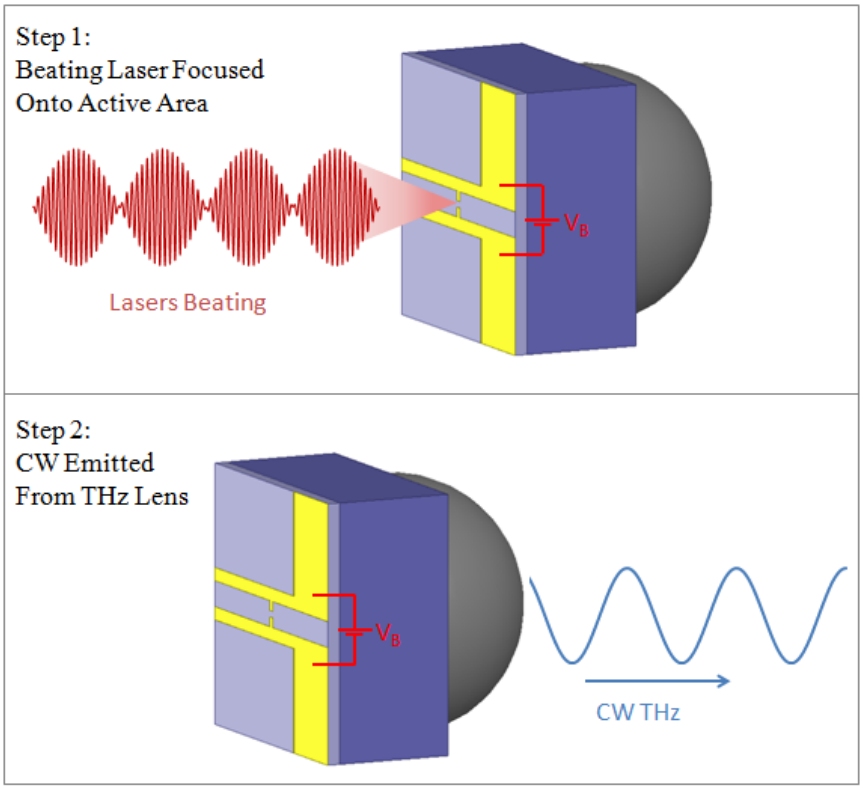

Figure 2.3: Photoconductive mixing a.) incident beating CW lasers focused onto biased active area b.) CW THz emitted from the back of the substrate

Photomixing was initially investigated by [4], which states that the THz emission is dependent on the photocarrier density [5]:

$$\frac{dn}{dt} = \frac{\eta}{h\nu_c Ad} P(\omega, t) - \frac{n}{\tau}, \tag{2.1}$$

where $\omega = 2\pi\Delta\nu$, n is the photocarrier density, η is the quantum efficiency, A is the active area, d is the absorption depth, and $h\nu_c$ is the photon energy. The incident optical power is given by:

$$P(\omega, t) \approx P_1 + P_2 + 2\sqrt{mP_1P_2}cos(\omega t), \tag{2.2}$$

where P_1 and P_2 are the laser powers at ν_1 and ν_2, respectively. Modulation depth

$(0 \leq m \leq 1)$ accounts for the polarization overlap between the two lasers.

THz radiation is generated by driving an antenna with an oscillating current source. This is achieved by applying a fixed voltage across a modulated conductance which is given by:

$$G(\omega, t) \approx \frac{\mu e d\sqrt{A}}{r} n(\omega, t) \approx G_0[1 + \beta sin(\omega t + \phi)], \tag{2.3}$$

where μ is the effective carrier mobility, e is the elementary charge, r is the width of the photoconductive gap. The second part of Eqn. 2.3 is used to simplify the concept of photomixing; G_0 is the average photoconductance and β represents the modulation of the photoconductance.

Photomixing is conceptually simple but its performance is limited by a key difficulty: the average source resistance, G_0^{-1}, is much larger than the antennas radiation resistance, R_A. Typical values for G_0 are in the $0.5M\Omega^{-1}$ region whereas $R_A < 200\Omega$. This results in poor transmitter and receiver antenna efficiency, thereby limiting the practicality of a radiating photomixing source.

This concept is illustrated by considering the following circuit (Figure 2.4) which models an ideal (no capacitance) photomixer:

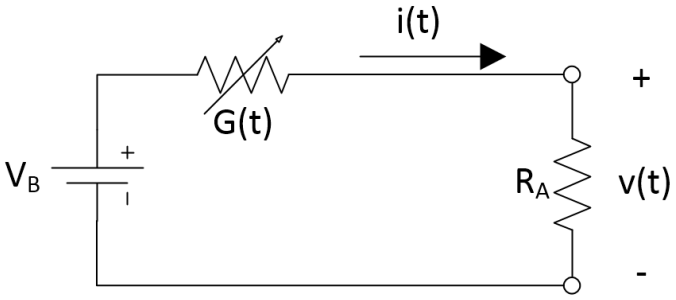

Figure 2.4: Photomixer circuit equivalent

where:

$$i(t) = \frac{G(t)V_B}{G(t)R_A + 1}, \tag{2.4a}$$

$$v(t) = i(t)R_A = \frac{G(t)V_B R_A}{G(t)R_A + 1}, \tag{2.4b}$$

the total radiated power, is given by:

$$P_{rad} = \left(\frac{i_{p-p}}{2\sqrt{2}}\right)^2 R_A, \tag{2.5}$$

where i_{p-p} is the peak-to-peak current. In a realistic situation (except ignoring C) we can select: $G_0 = 0.5M\Omega^{-1}$, $\beta = 1$, $R_A = 100\Omega$, $f = 1\ THz$, and $V_B = 20V$ which results in 80nW of radiated power. For reasons discussed in Section 4.1 we expect 15% of the radiated power at the output of the PCA lens; hence, at most, we expect 12nW of radiated power directed to the receiver. Introduction of the gap capacitance would further reduce output power.

Another difficulty arises from substrate material parameters. A reduction in THz power will occur if the substrate carrier lifetime is longer than the THz period. This implies that the substrate's response time may be too large for operation in the THz region; thus, further limiting the viability of a high efficiency photomixer system.

Photoconductive Switching

Photoconductive switching is the process of generating a pulsed THz signal. Pulsed THz signals are generated by focusing a femtosecond optical pulse onto the active area of a PCA as shown in Figure 2.5. The semiconductor's conductivity sharply rises when the optical pulse is absorbed and falls as the carriers trap and recombine when the optical pulse dissipates.

During excitation photocarriers are generated and accelerated along the electric field, E_B, established by V_B towards the antenna electrodes. The emitted THz field is proportional to the current surge produced by the carriers. Eqn. 2.6 illustrates this relationship [6]:

$$E_{THz} = \frac{1}{4\pi\epsilon_0}\frac{A}{c^2 z}\frac{\partial j(t)}{\partial t} = \frac{1}{4\pi\epsilon_0}\frac{A}{c^2 z}\frac{\partial n(t)}{\partial t} e\mu_e E_B, \tag{2.6}$$

where $j(t)$ is the current density, $n(t)$ is the photocarrier density, A is the laser spot size in the active area, E_B is the electric field established by V_B, c is the speed of light in a vacuum, z is the distance from the active area, e is the elementary charge, and μ_e is the electron mobility.

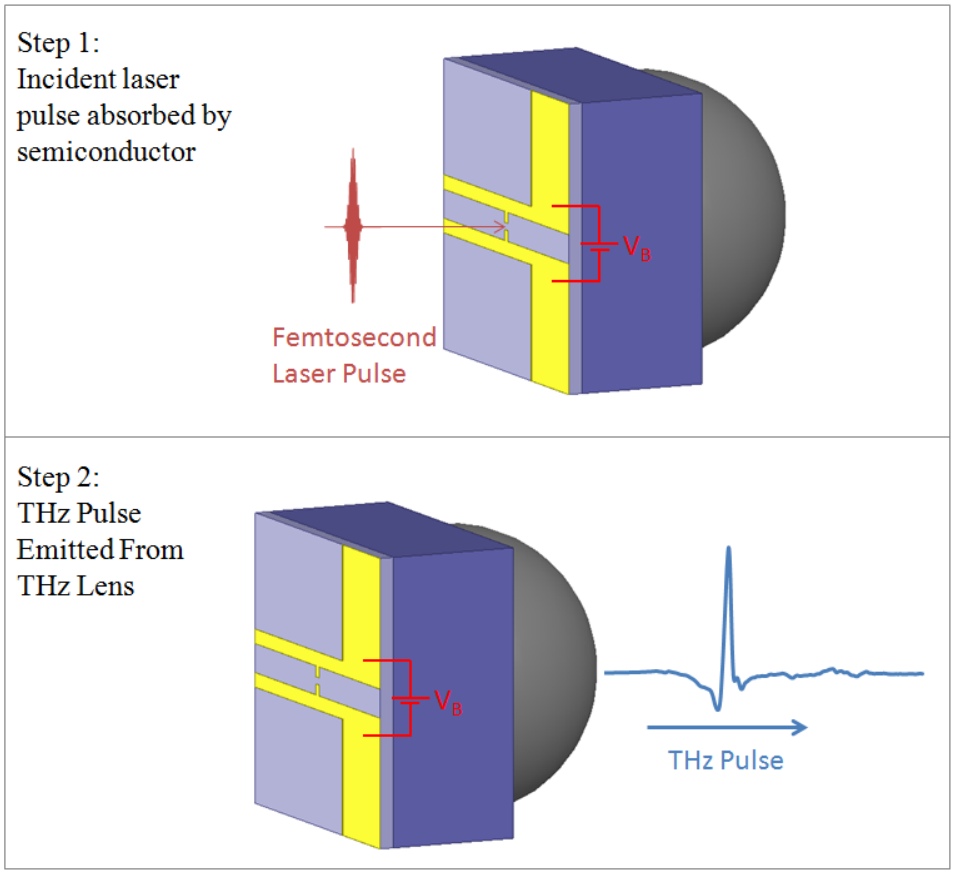

Figure 2.5: Photoconductive switching a.) incident femtosecond pulse focused onto biased active area b.) THz pulse emitted from the back of the substrate

As with photomixing, the conductance is dependent on the incident optical power. For photoswitching the instantaneous peak pulse power is large, $P_{peak} \approx 4kW$, as opposed to photomixing where $P_{max}(\omega, t) \approx 50mW$. The conductance of the photoconductive switch becomes comparable to the radiation resistance during the illumination time, hence more current is driven through the antenna, resulting in higher THz output powers.

Pulsed-Wave THz Detection

Figure 2.6 illustrates the photoconductive detection process. Photoconductive detection of the THz field is reciprocal to the generation process; the THz pulse is transmitted through free-space and focused on the receiver PCA. The incident THz field induces a current in the receiving PCA which is dependent on the transient

conductivity of the receiver.

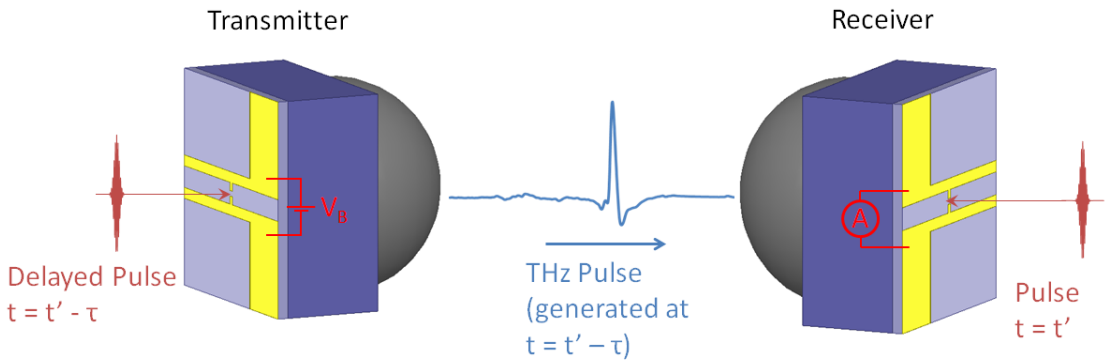

Figure 2.6: THz pulse detection

Mathematically speaking, we are convolving the THz pulse and the receiver's impulsed conductivity which is given by [7]:

$$J_{rx}(t) = \int_{-\infty}^{t} \sigma_s(t-\tau) E_{THz}(\tau) d\tau. \tag{2.7}$$

To provide a better understanding, consider the convolution of an impulse, $\delta(t)$, with another function, $f(t)$:

$$\int_{-\infty}^{t} \delta(t-\tau) f(\tau) d\tau = H(0) f(t) = \frac{f(t)}{2}, \tag{2.8}$$

where $H(0)$ is the Heaviside step function: $H(t<0) = 0$ and $H(t>=0) = 1$.

Referring to Equation 2.7, if σ_s closely approximates an impulse then J_{rx} will be directly proportional to E_{THz}. For this reason we desire to have a short carrier lifetime with respect to the E_{THz} pulse width (≈1-2ps). Typical carrier lifetimes for SI-GaAs are >20ps, which is undesirable. For LT-GaAs lifetimes are in the 0.3-0.7ps range [8].

2.1.2 Photoexcitation of Carriers

To radiate an electromagnetic field a change in current is required. For THz radiation, the change in current originates from carrier excitation in the active area. Free electrons and holes are generated using a laser with photon energies exceeding the band-gap energy of the material (i.e. $E_G(GaAs) = 1.43eV$). The excited carriers are

accelerated by the electric field established by the bias voltage resulting in a change in current. Figure 2.7 illustrates the carrier generation process.

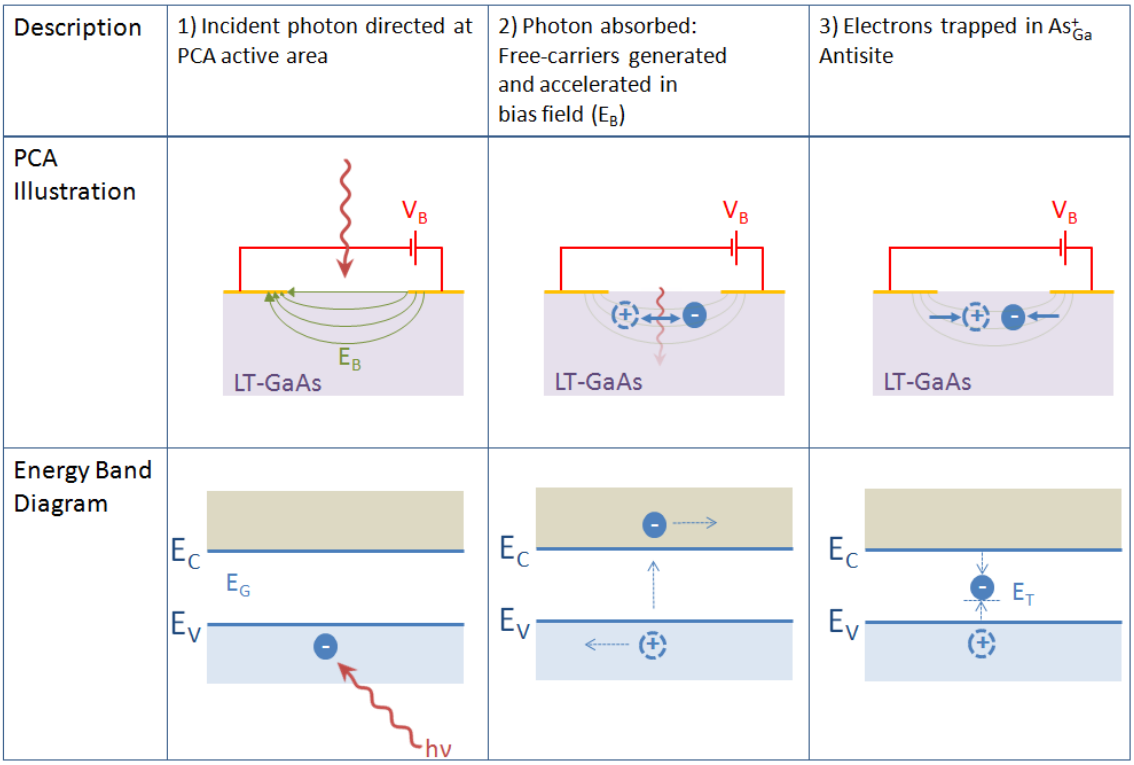

Figure 2.7: Photon absorption, free-carrier generation, and non-radiative recombination

Carrier Screening

Figure 2.8 illustrates the concept of bias field screening. Under steady-state conditions a uniform E-field exists in the active area (see Figure 2.8a). Upon excitation by a femtosecond pulse free-carriers are generated and accelerated by the bias field. The separation of the space-charges results in an induced field of the opposite polarity (see Figure 2.8b). The magnitude of the induced field is proportional to the number of generated carriers and is thus proportional to the incident optical power. The induced field "screens" the bias field which reduces the net force applied to the free-carriers. Carrier screening saturates the optical-to-THz efficiency. Therefore higher optical power does not always result in higher THz power [9]. For the photoconductive sources discussed in this thesis, carrier screening is not an issue because of the relatively low pump powers.

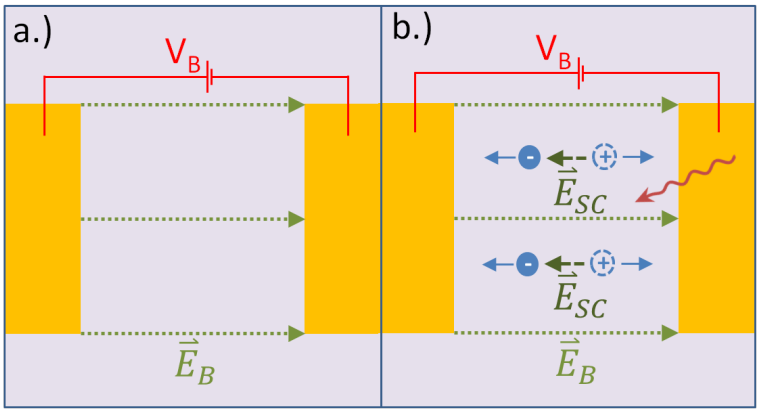

Figure 2.8: Bias field screening a.) The PCAs active area prior to excitation b.) The PCAs active area after the carriers have been generated, $\vec{E}_{SC}$ points in the opposite direction to $\vec{E}_B$ thus decreasing the overall field and force applied to the carriers

2.1.3 Terahertz optics

Optical guiding and focusing mechanisms are commonly used in the THz frequency domain. Reflective (metallic) or transmissive (typically silicon or Teflon) lenses are generally used in commonplace THz-TDS to focus the THz beam into a sample region [1].

Figure 2.9 illustrates a typical Gaussian beam where the beam parameters are overlaid. Gaussian beam theory is used to obtain a first approximation for the THz wavefront and beam shape [3]:

$$E(r,z) = E_0 \frac{w_0}{w(z)} \exp\left(-\frac{r^2}{w^2(z)}\right) \exp\left(-i\left[kz - \tan^{-1}\left(\frac{z}{z_R}\right) + \frac{kr^2}{2R(z)}\right]\right), \quad (2.9)$$

where:

$$\text{Waist size: } w_0 = \frac{\lambda}{\pi\theta},$$
$$\text{Rayleigh length: } z_R = \frac{\pi w_0^2}{\lambda},$$
$$w(z) = w_0\sqrt{1 + (z/z_R)^2},$$
$$R(z) = z[1 + (z_R/z)^2].$$

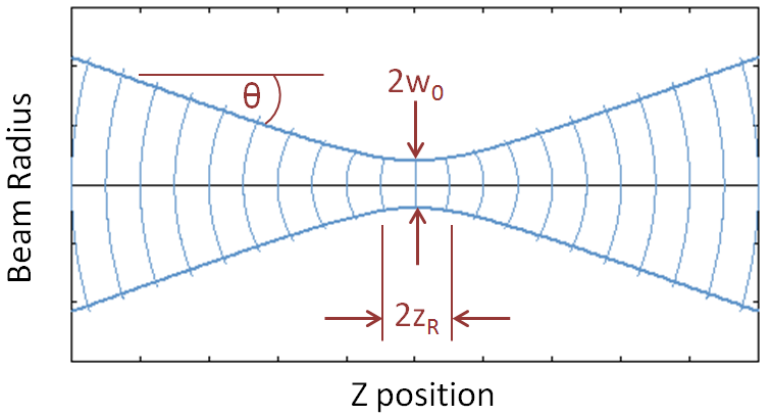

Figure 2.9: Gaussian Beam [3]

Figure 2.10 illustrates the approximate THz field emitted by a photomixer coupled to a HRFZ-Si aspheric focusing lens. The illustrated Gaussian beams are for a CW THz system but still provide useful insight for a pulsed THz system.

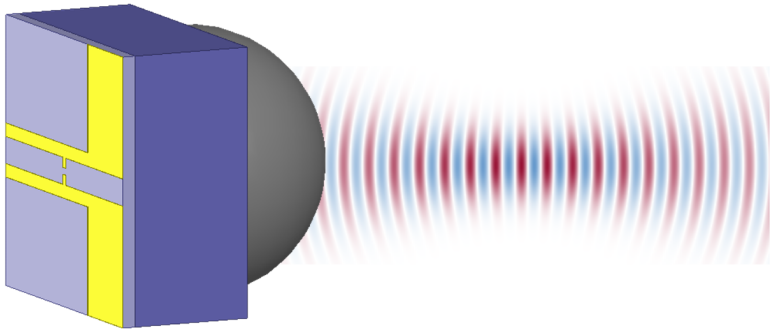

Figure 2.10: Photomixer with Gaussian THz beam [3]

2.1.4 Dielectric Interfaces

Propagating electromagnetic waves experience reflections at dielectric interfaces. Equation 2.6 states that the THz field amplitude is proportional to power absorbed in the substrate. Therefore it is desirable to maximize the power transmitted into the substrate which can be accomplished by implementing an Anti-reflection (AR) coating.

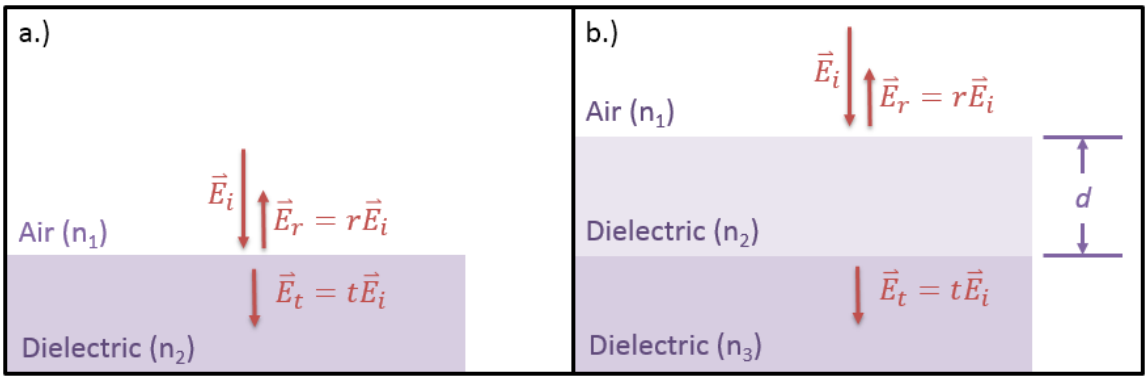

Figure 2.11: AR coating definition a.) Dielectric interface b.) Single-layer etalon

Simple Air-Dielectric Interface

First we will investigate a simple air-dielectric interface similar to that illustrated in Figure 2.11a. The incident, reflected and transmitted fields are given by [10]:

incident field,

$$\vec{E}_i = \hat{x} E_0 e^{-jk_0 z}, \tag{2.10a}$$

$$\vec{H}_i = \hat{y} \frac{E_0}{\eta_0} e^{-jk_0 z}, \tag{2.10b}$$

reflected field,

$$\vec{E}_r = \hat{x} E_0 \Gamma e^{jk_0 z}, \tag{2.11a}$$

$$\vec{H}_r = -\hat{y} \frac{E_0 \Gamma}{\eta_0} e^{jk_0 z}, \tag{2.11b}$$

and transmitted field,

$$\vec{E}_t = \hat{x} E_0 T e^{-\gamma z}, \tag{2.12a}$$

$$\vec{H}_t = \hat{y} \frac{E_0 T}{\eta} e^{-\gamma z}, \tag{2.12b}$$

where Γ and T are the respective reflection and transmission coefficients. The propagation constant and intrinsic impedance for the dielectric region are represented by:

$$\gamma = \alpha + j\beta = \alpha + jnk_0, \tag{2.13}$$

and,

$$\eta = \frac{j\omega\mu}{\gamma} = \frac{j\omega\mu}{\alpha + jnk_0}, \tag{2.14}$$

respectively.

After applying the boundary conditions - the tangential components are continuous across the interface - we arrive at expressions for the reflection and transmission coefficients:

$$\Gamma = \frac{\eta - \eta_0}{\eta + \eta_0}, \tag{2.15a}$$

$$T = 1 + \Gamma = \frac{2\eta}{\eta + \eta_0}. \tag{2.15b}$$

In a non-magnetic material the transmission coefficient can be written as:

$$T = 1 + \Gamma = \frac{2\eta}{\eta + \eta_0} = \frac{2k_0}{\alpha^2 + k_0^2(n+1)^2}[(n+1)k_0 + i\alpha]. \tag{2.16}$$

Application of Equation 2.16 to GaAs at 780nm ($n \approx 3.6$ and $\alpha \approx 1.45 \times 10^4 cm^{-1}$) reveals that we can only achieve $|T| = 0.68$. We can increase the transmission significantly by incorporating an AR coating on the dielectric.

Anti-Reflection Coating

AR coatings are used to minimize the reflection from a dielectric interface. AR coatings operate on the principle of constructive and destructive interference; and therefore exhibit wavelength dependent characteristics. An ideal AR coating is capable of achieving $\Gamma \approx 0$ for the designed wavelength.

Figure 2.11b illustrates a single layer dielectric etalon which is the basis of a simple AR coating. A full derivation for the reflection and transmission coefficients can be found in [11], which states:

$$\Gamma = \frac{\left(\frac{n_1 - n_2}{n_1 + n_2}\right) + \left(\frac{n_2 - n_3}{n_2 + n_3}\right) e^{-j2\phi}}{1 + \left(\frac{n_1 - n_2}{n_1 + n_2}\right)\left(\frac{n_2 - n_3}{n_2 + n_3}\right) e^{-j2\phi}}, \tag{2.17a}$$

$$T = \frac{\left(\frac{2n_1}{n_1 + n_2}\right)\left(\frac{2n_2}{n_2 + n_3}\right) e^{-j\phi}}{1 + \left(\frac{n_1 - n_2}{n_1 + n_2}\right)\left(\frac{n_2 - n_3}{n_2 + n_3}\right) e^{-j2\phi}}, \tag{2.17b}$$

where:

$$\phi = \frac{2\pi n_2 d}{\lambda}. \tag{2.18}$$

Referring to Equation 2.17a, we can design an AR coating by specifying $\Gamma = 0$:

$$\Gamma = 0 = \left(\frac{n_1 - n_2}{n_1 + n_2}\right) + \left(\frac{n_2 - n_3}{n_2 + n_3}\right) e^{-j2\phi} \tag{2.19}$$

which can be satisfied given that:

$$n_2 = \sqrt{n_1 n_3} \quad and \quad \phi = \pi/2, 3\pi/2, 5\pi/2, \cdots \tag{2.20}$$

Applying Equation 2.20 to an air-GaAs interface at an excitation wavelength of 780nm reveals the ideal parameters for a simple AR coating.

$$n_2 = \sqrt{3.6} = 1.8974 \tag{2.21}$$

$$\pi/2 = \frac{2\pi n_2 d}{\lambda} \Rightarrow d = \frac{\lambda}{4n_2} = \frac{780nm}{4 \times 1.8974} = 101.4nm \tag{2.22}$$

We cannot easily make a material with the ideal refractive index, so a viable material needs to be selected. Glass-like materials are viable options where $n_2 \approx 1.48$ at 780nm; thus $d = 131nm$. Figure 2.12 plots the reflection and transmission coefficients around the excitation wavelength given that $n_2 = 1.48$.

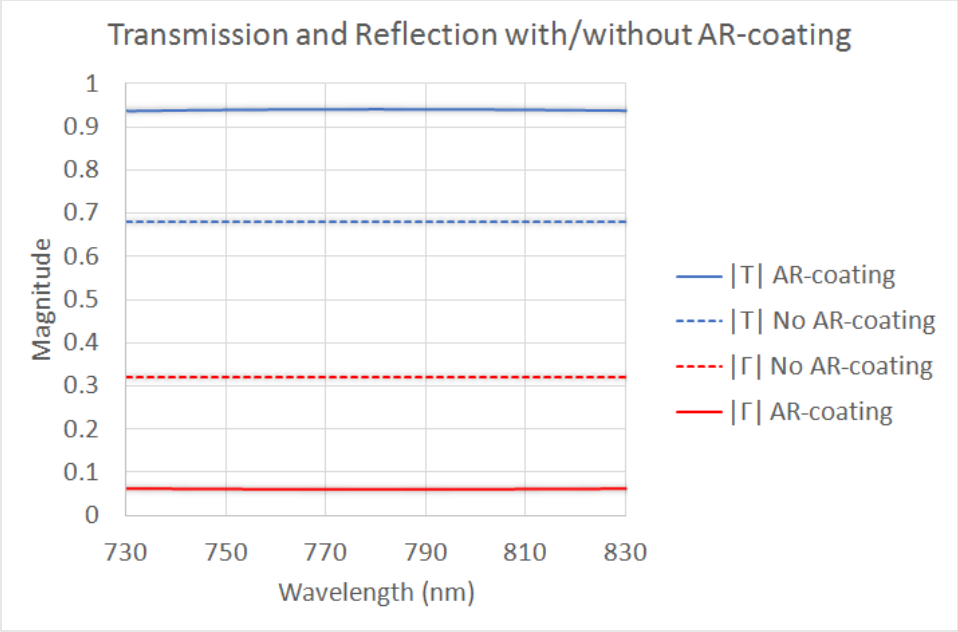

Figure 2.12: Transmission and reflection coefficients for 131nm thick glass-like ($n_2 = 1.48$) AR-coating on GaAs ($n_3 = 3.6$) for $\lambda_c \pm 50nm$

2.2 Vibrational and Rotational Molecules

Terahertz Time Domain Spectroscopy (THz-TDS) is a main application for THz waves. THz-TDS is used to classify polar molecules by measuring the absorption related to either vibrational or rotational modes. Both pulsed THz or CW THz can be used for THz-TDS, although pulsed is typically used due to higher THz powers.

THz-TDS probes the spectral absorption corresponding to molecular vibrational and rotational states [7, 12]. Vibrational and rotational absorption spectra can be derived from the molecular Schrödinger equation. The equation is simplified by the Born-Oppenheimer approximation which decouples the fast electron motion and the slow nuclear motion. The slow nuclear motion describes the molecular inter-nuclei displacements from which the vibrational and rotational states originate.

Molecular rotations can be excited by THz photon energies. Rotational spectroscopy is performed on gas phase molecules because intermolecular forces are minimized. In a liquid or solid phase medium the rotations are damped and become "vibrations"[12].

To excite rotations the molecule has to be polarized for the electric field to induce motion. To determine if a gas can be excited by a THz wave the molecular dipole moment is examined. Molecules with large dipole moments (water 1.85D, acetone 2.91D, methanol 1.69D) will show rotational absorption lines. Chemicals with small dipole moments (carbon monoxide 0.112D, carbon dioxide 0D) will show negligible absorption.

2.3 Transmission Line Theory

Transmission line theory [10] is used to analyze complex power transfer between a source and load when conductor lengths are near or above the electrical wavelength. Under these circumstances transmission line theory is required because a non-uniform charge distribution exists on the conductors. The primary focus of this theory is to develop a scalable distributed model which describes the unique voltage and current characteristics for conductors in a medium. For most conductors the current-voltage relationship is described as a function of conductor resistance, capacitance, and inductance. The difference between transmission line and waveguide theory (Section 2.4) is that a transmission line requires two or more conductors, hence it can support a Transverse Electromagnetic (TEM) mode. Figure 2.13 illustrates the distributed

model for a generic transmission line:

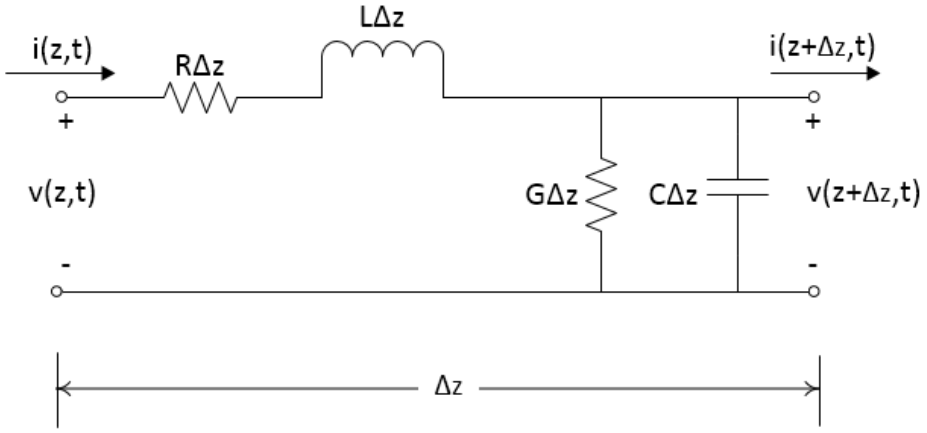

Figure 2.13: Distributed Transmission Line Model

where each of the parameters; resistance per meter (R), inductance per meter (L), conductance per meter (G), and capacitance per meter (C) are used to describe wave propagation along the length of the transmission line.

By applying Kirchhoff's voltage and current laws to Figure 2.13 and taking the limit ($\Delta z \to 0$), the telegraphers equations are obtained:

$$\frac{\partial v(z,t)}{\partial z} = -Ri(z,t) - L\frac{\partial i(z,t)}{\partial t} \tag{2.23a}$$

$$\frac{\partial i(z,t)}{\partial z} = -Gv(z,t) - C\frac{\partial v(z,t)}{\partial t} \tag{2.23b}$$

If the excitation source is a steady-state sinusoid, Eqn. (2.23) can be represented by the following wave equation:

$$\frac{d^2V(z)}{\partial z} - \gamma^2 V(z) = 0 \tag{2.24a}$$

$$\frac{d^2I(z)}{\partial z} - \gamma^2 I(z) = 0 \tag{2.24b}$$

Where $\gamma = \sqrt{(R + j\omega L)(G + j\omega C)}$ is referred to as the propagation constant. The solution to Eqn. (2.24) is expressed as:

$$V(z) = V_0^+ e^{-\gamma z} + V_0^- e^{\gamma z} \tag{2.25a}$$

$$I(z) = I_0^+ e^{-\gamma z} + I_0^- e^{\gamma z} \tag{2.25b}$$

Eqn. 2.25 describes the voltage and current on a transmission line where the relationship between them is referred to as the characteristic impedance (Z_0):

$$Z_0 = \frac{V_0^+}{I_0^+} = -\frac{V_0^-}{I_0^-} = \sqrt{\frac{R + j\omega L}{G + j\omega C}} \tag{2.26}$$

For a TEM waveguide - such as two parallel plates - the parameters from Eqn. 2.26 can be obtained by field analysis in the transverse plane.

Figure 2.14 illustrates a typical transmission line diagram, where: V_S and Z_S are the source voltage and impedance; Z_0 is the characteristic impedance of the transmission line; and Z_L is the load impedance.

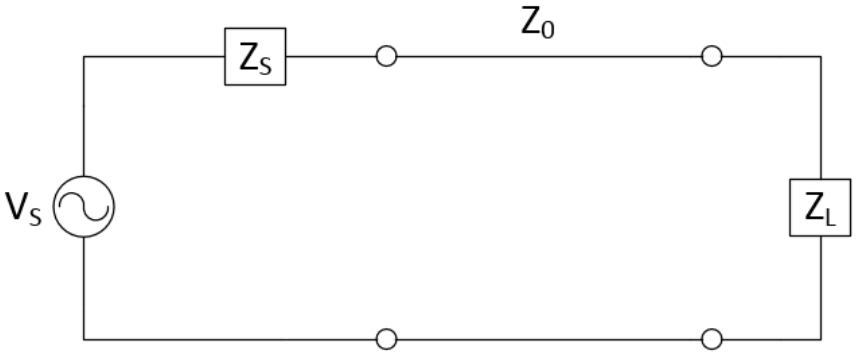

Figure 2.14: Generic Transmission Line

2.4 Waveguides

Waveguides confine and guide electromagnetic energy in a structure defined by its boundary conditions. Waveguides can utilize conductors or other media (such as dielectric boundaries); for this document we will focus on waveguides which utilize conductive boundaries.

Transverse Electromagnetic (TEM) waves are field configurations that do not have electric or magnetic field components in the propagation direction. Transverse Electric (TE) or Transverse Magnetic (TM) waves have the respective magnetic or

electric field component in the direction of propagation. Both TE and TM waves are not ideal for broadband THz since they experience non-uniform characteristics with respect to frequency - meaning they have dispersive properties. Ideally a broadband THz signal should propagate in a dispersionless medium (such as air) or a TEM transmission line.

TEM waves are derived from the source-free Maxwell equations shown in Eqn. 2.27 [10]. After equating the individual field components in Eqn. 2.27 we arrive at Eqn. 2.28 (assuming the wave is propagating in the $\hat{z}$ direction as $e^{-j\beta z}$).

$$\nabla \times \vec{E} = -j\omega\mu\vec{H} \tag{2.27a}$$

$$\nabla \times \vec{H} = j\omega\epsilon\vec{E} \tag{2.27b}$$

$$\frac{\partial E_z}{\partial y} + j\beta E_y = -j\omega\mu H_x \tag{2.28a}$$

$$-j\beta E_x - \frac{\partial E_z}{\partial x} = -j\omega\mu H_y \tag{2.28b}$$

$$\frac{\partial E_y}{\partial x} - \frac{\partial E_x}{\partial y} = -j\omega\mu H_z \tag{2.28c}$$

$$\frac{\partial H_z}{\partial y} + j\beta H_y = j\omega\epsilon E_x \tag{2.28d}$$

$$-j\beta H_x - \frac{\partial H_z}{\partial x} = j\omega\epsilon E_y \tag{2.28e}$$

$$\frac{\partial H_y}{\partial x} - \frac{\partial H_x}{\partial y} = j\omega\epsilon E_z \tag{2.28f}$$

As mentioned previously, a TEM wave has no field components in the direction of propagation ($E_z = H_z = 0$), therefore Eqn. 2.28 reduces to:

$$\beta E_y = -\omega\mu H_x, \tag{2.29a}$$

$$\beta E_x = \omega\mu H_y, \tag{2.29b}$$

$$\frac{\partial E_y}{\partial x} = \frac{\partial E_x}{\partial y}, \tag{2.29c}$$

$$\beta H_y = \omega\epsilon E_x, \tag{2.29d}$$

$$-\beta H_x = \omega\epsilon E_y, \tag{2.29e}$$

$$\frac{\partial H_y}{\partial x} = \frac{\partial H_x}{\partial y}. \tag{2.29f}$$

By substitution in Eqn. 2.29 we find the dispersion relation: $\beta = \omega\sqrt{\mu\epsilon} = k$, meaning that there is no Group Velocity Dispersion (GVD) since $\frac{\partial\beta}{\partial\omega} = \sqrt{\mu\epsilon}$ is a constant (providing that $\epsilon(\omega)$ remains relatively constant). Next we take the curl of Eqn. 2.27 to find Helmholtz wave equations:

$$\nabla^2\vec{E} + \omega^2\mu\epsilon\vec{E} = \nabla^2\vec{E} + k^2\vec{E} = 0, \tag{2.30a}$$

$$\nabla^2\vec{H} + \omega^2\mu\epsilon\vec{H} = \nabla^2\vec{H} + k^2\vec{H} = 0. \tag{2.30b}$$

Again, given a e^{-jkz} dependence we find that Eqn. 2.30 reduces to expressions involving only transverse fields:

$$\nabla_t^2\vec{e}_t(x,y) = 0, \tag{2.31a}$$

$$\nabla_t^2\vec{h}_t(x,y) = 0. \tag{2.31b}$$

Given that the longitudinal field components are zero, $e_z = 0$ and $h_z = 0$, the transverse fields are expressed as an electrostatic field:

$$\vec{e}_t(x,y) = -\nabla_t\Phi(x,y), \tag{2.32}$$

$$\nabla_t^2\Phi(x,y) = 0. \tag{2.33}$$

For a TEM wave to exist a voltage (or difference in static potential) must exist in the transverse plane. This imposes a restriction: two conductors are required for TEM waveguide propagation - this restriction doesn't apply to TE or TM waveguide modes. General field equations for TE and TM modes are not discussed here but can be found in [10].

2.4.1 Parallel Plate Waveguide

A Parallel Plate Waveguide (PPWG) is investigated because it supports a TEM wave [13, 14, 15]. Figure 2.15 illustrates a PPWG which consists of two thin conductive plates of height T, separated by distance S.

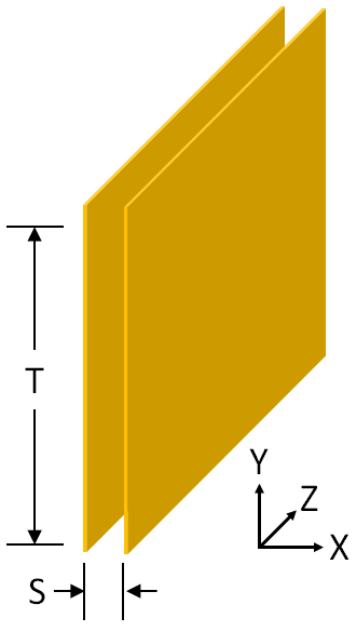

Figure 2.15: Parallel Plate Waveguide

The electrostatic solution for a PPWG (neglecting fringing fields and $T \gg S$) is obtained from Laplace's equation (Eqn. 2.33) [10]. One plate is at potential $\Phi(x = -\frac{S}{2}, y) = -\frac{V_0}{2}$ and the other is at $\Phi(x = \frac{S}{2}, y) = \frac{V_0}{2}$. Laplace's equation can be simplified to:

$$\nabla_t^2 \Phi(x,y) = \left[\frac{\partial^2}{\partial x^2} + \frac{\partial^2}{\partial y^2}\right] \Phi(x,y) \quad \Rightarrow \quad \frac{d^2\Phi(x)}{dx^2} = 0, \tag{2.34}$$

therefore the solution to the differential equation is given by:

$$\Phi(x) = c_1 + c_2 x \tag{2.35}$$

$$\Phi\left(x = -\frac{S}{2}\right) = c_1 + c_2\left(-\frac{S}{2}\right) = -\frac{V_0}{2}, \tag{2.36a}$$

$$\Phi\left(x = \frac{S}{2}\right) = c_1 + c_2\left(\frac{S}{2}\right) = \frac{V_0}{2}, \tag{2.36b}$$

which results in $c_1 = 0$ and $c_2 = \frac{V_0}{S}$.

$$\Phi(x) = \frac{V_0 x}{S} \tag{2.37}$$

From Eqn. 2.32 we find that the transverse field is:

$$\vec{e}_t(x) = -\nabla_t \Phi(x) = -\left[\hat{x}\frac{\partial}{\partial x} + \hat{y}\frac{\partial}{\partial y}\right]\frac{V_0 x}{S} = -\hat{x}\frac{V_0}{S} \tag{2.38a}$$

$$\vec{h}_t(x) = \frac{1}{\eta}\hat{z} \times \vec{e}_t(x) = \hat{y}\frac{1}{\eta}\frac{V_0}{S} \tag{2.38b}$$

A TEM wave does not experience cut-off ($k = \omega\sqrt{\mu\epsilon} = \beta$), therefore the fields are given by:

$$\vec{E}(x, y, z) = \vec{e}_t e^{-jkz} = -\hat{x}\frac{V_0}{S}e^{-jkz} \tag{2.39a}$$

$$\vec{H}(x, y, z) = \vec{h}_t e^{-jkz} = \hat{y}\frac{1}{\eta}\frac{V_0}{S}e^{-jkz} \tag{2.39b}$$

The previous equations are used for determining the field profiles provided that the gap aspect ratio is sufficient ($T \gg S$). Figure 2.16 illustrates the simulated field for $\frac{T}{S} = 30$. Fringing fields interfere with the legitimacy of the approximation as $\frac{T}{S} \to 0$. At the limit of small $\frac{T}{S}$, the parallel plate waveguide becomes a free-space slotline waveguide.

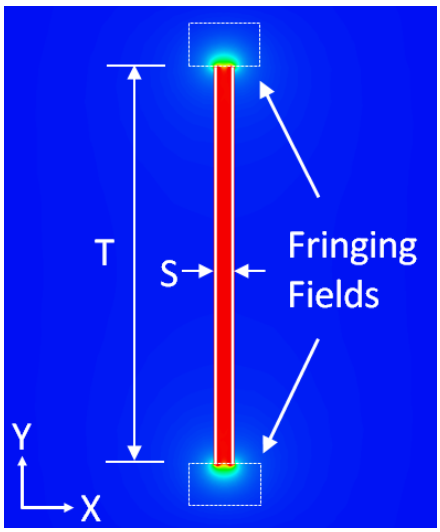

Figure 2.16: Parallel Plate Waveguide, $|E|$

2.4.2 Dielectric Waveguide

A dielectric waveguide has similar properties to an optical fiber, this concept will be relevant in the next two sections. Certain waveguides (slotline and coplanar strips)

are metalizations on top of a dielectric substrate. For these waveguides the substrate can operate as a parasitic dielectric waveguide. This concept is typically discussed using the terminology "surface wave modes" [16]. Figure 2.17 illustrates the concept of surface waves which are confined to the substrate by Total Internal Reflection (TIR).

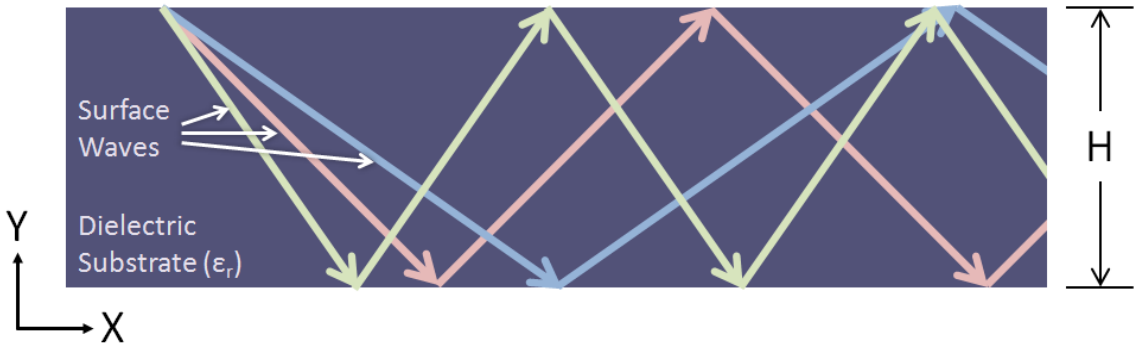

Figure 2.17: Surface wave

Surface waves are not supported by conductors and have TE or TM field configurations. As with typical TE and TM waves, cut-off inhibits mode propagation below a specific frequency given by:

$$TE_n \ \& \ TM_n: \quad f_c = \frac{(n-1)c_0}{2H\sqrt{\epsilon_r - 1}}, \quad n = 1, 2, 3, ... \tag{2.40}$$

At microwave frequencies surface waves are not heavily excited because $H \ll \lambda_d$; this is untrue for THz waves. A typical THz substrate is GaAs with $\epsilon_r = 12.89$ and $H = 350\mu m$; therefore, at 3 THz up to 25 THz TE and TM modes can be excited. While the dielectric slab supports many modes, they will not be excited unless the source shares field symmetry. In the following sections surface waves will be considered a parasitic loss mechanism.

2.4.3 Slotline Waveguide

A Slotline (SL) waveguide is a printed or etched metalization on a dielectric substrate commonly used at microwave frequencies. Figure 2.18 illustrates a typical slotline waveguide. A slotline is typically used because it only requires a single-sided metalization on a substrate. Alternatives requiring a dielectric with a two-sized metalization have limited usefulness in the THz region due to the thick substrate

($H \gg \lambda_d$). Slotlines on dielectric substrates are prone to losses which originate from radiation, parasitic modes, and from finite metalization conductivity. Methods are available to mitigate some of these losses, although it may not be possible to design a practical broadband low-loss slotline on a dielectric substrate that is capable of traversing many wavelengths.

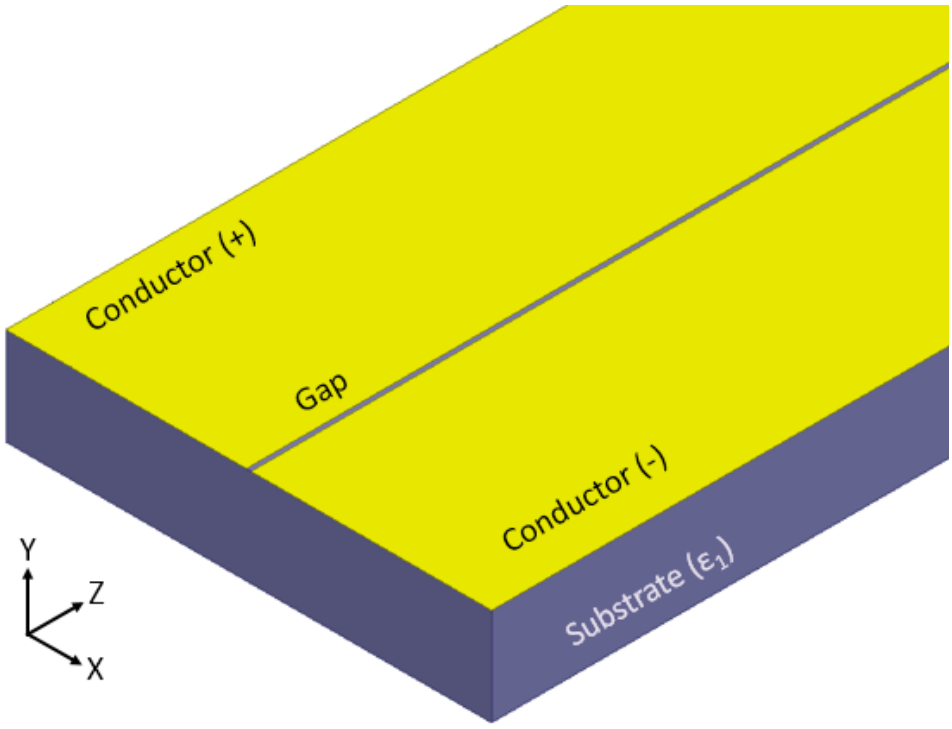

Figure 2.18: Slotline Waveguide

A slotline supports a quasi-TEM field in the gap between the conductors and surrounding medium. Figure 2.19 illustrates the quasi-TEM field distribution of the slotline. This field distribution is not subject to cut-off because of the field is supported by two conductors [16].

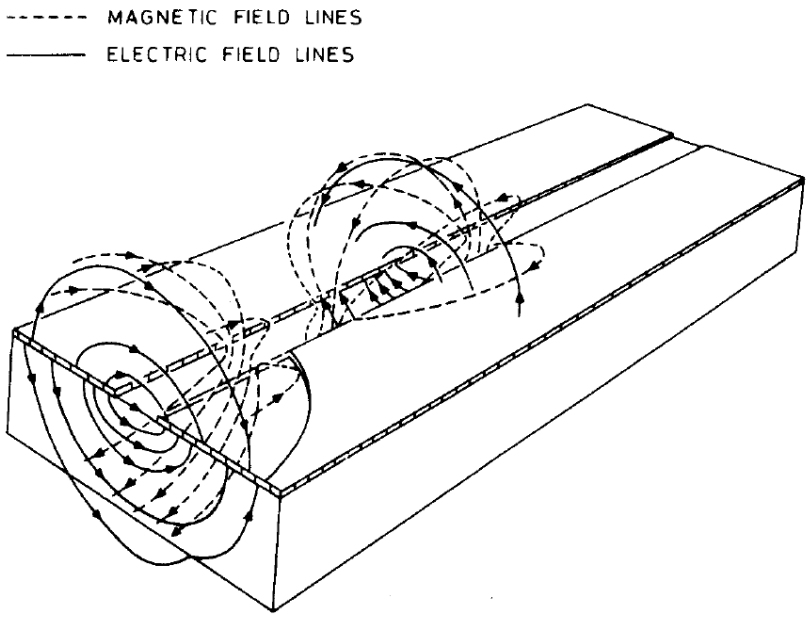

Figure 2.19: Quasi-TEM field distribution in a slotline. Reproduced by permission from [16]. © 1996 by Artech House, Inc.

Figure 2.20 illustrates a cross-section of a slotline with exaggerated dimensions. A typical requirement for a slotline is that $T \ll S \ll \lambda_0$; as T approaches S the slotline begins to resemble a parallel-plate waveguide with a dielectric interface on one side. Derivations for slotlines parameters (capacitance, inductance, etc) use the approximation that $T = 0$ [17] which is only valid when $T \ll S \ll \lambda_0$. An alternative case where $T \not\ll S \not\ll \lambda_0$ is examined by simulation in Section 2.4.6.

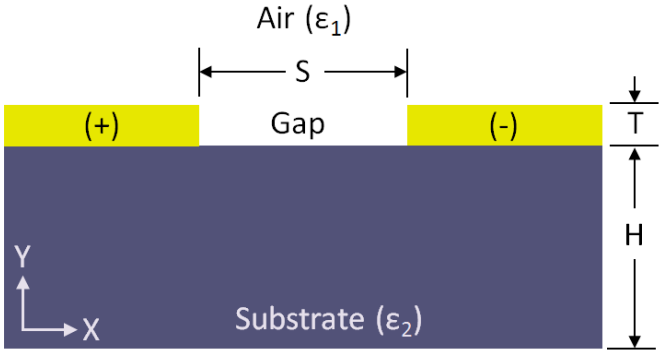

Figure 2.20: Slotline cross-section

Figure 2.21 plots the transverse electrostatic slotline field, $|E|$, for two different $\frac{S}{T}$ ratios; Figure 2.21a approximates a parallel-plate, Figure 2.21b approximates a

slotline. Comparison between the fields reveal that confinement is enhanced as $\frac{S}{T} \to 0$.

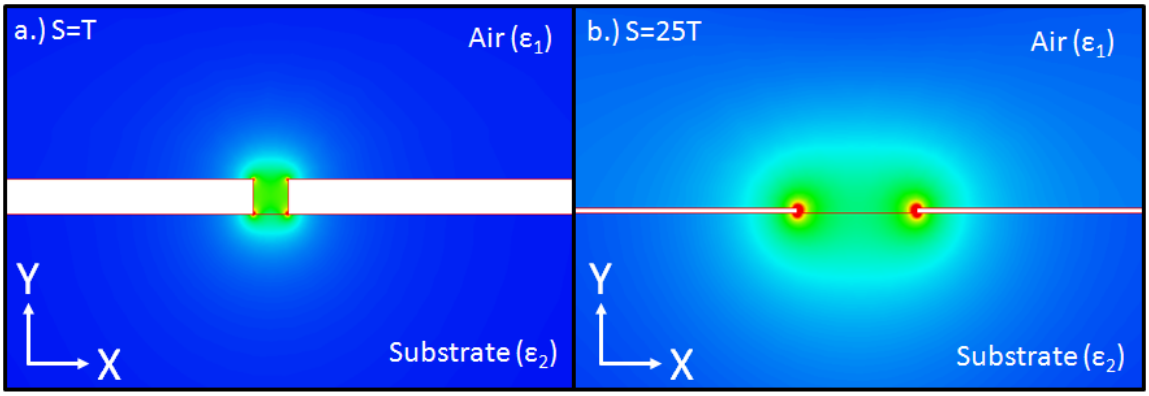

Figure 2.21: Transverse cross-section of the electrostatic slotline field, $|E|$ ($\epsilon_{r1} = 1$, $\epsilon_{r2} = 12.96$)

Losses

Slotlines are subject to losses through different mechanisms: conductor loss, dielectric loss, radiation loss, and surface wave losses. Unfortunately, due to the design of a slotline, closed-form expressions are not available for application in the THz region. This section will analyze the various loss sources using a Finite Element Method (FEM) simulation at 1 THz. To preview to the results, Figure 2.23 illustrates the relative contributions for all the loss sources.

Conductor Loss:

Conductor loss is a function of metal conductivity and surface current density. We expect high conductor losses when the field is highly localized on the waveguide conductor. For a slotline (T=0) the conductor loss is primarily dependent on S; small values of S imply large conductor losses due to large localized fields. A typical THz slotline (S=5μm) has a conductor loss in the $2dB/mm < \alpha_c < 10dB/mm$ range for $0.3THz < f < 1.5THz$, respectively.

Dielectric Loss:

Dielectric loss is dependent on the dielectric loss tangent and frequency. For our case, GaAs substrate given $f < 1.5THz$, the dielectric loss tangent is roughly $\tan\delta = 0.00085$. For these values the dielectric loss resides in the $\alpha_d < 0.5dB/mm$ range which is negligible in comparison to the other sources.

Surface Waves and Radiation Loss:

Parasitic surface waves limit the usefulness of the slotline waveguide on a dielectric substrate. Any surface current directed in the transverse direction will excite the many TE surface waves as discussed in Section 2.4.2 [18]. Excitation of these modes can be suppressed by introducing a superstrate on top of the slotline. This suppresses surface waves by increasing the propagation constant of the guided mode beyond that of the surface waves, $\beta > \beta_{SW}$ [19]; Figure 2.22 illustrates these concepts.

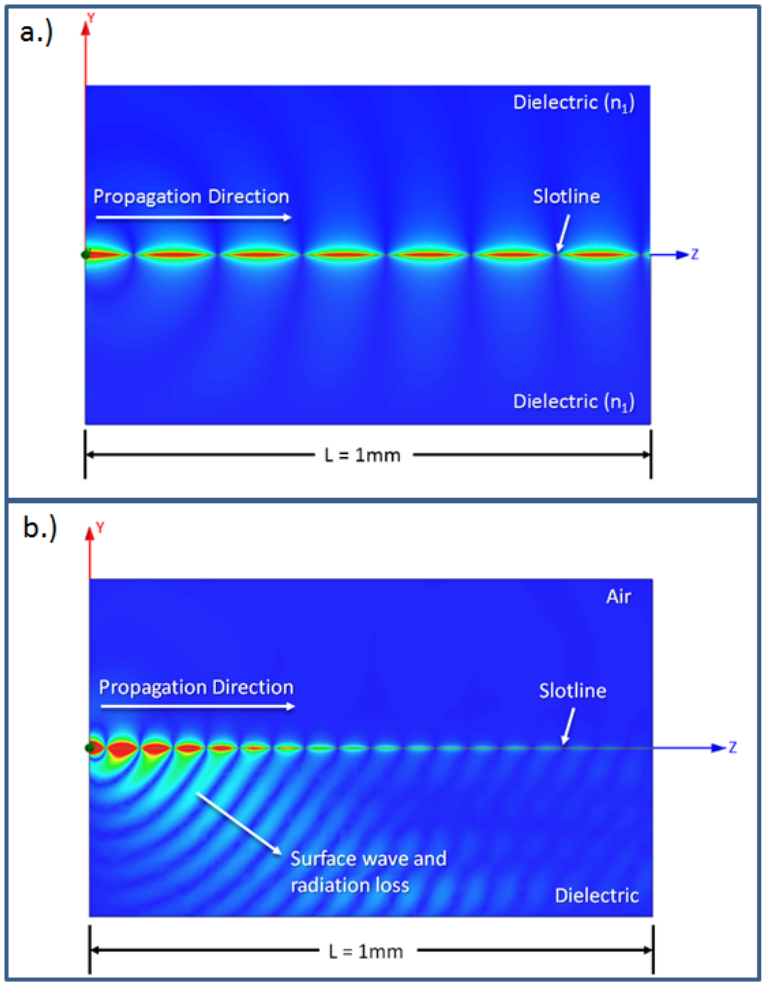

Figure 2.22: Guided mode and surface wave excitation. FEM simulation at 1 THz using planar PECs (T=0) and a gap separation of S=5μm. a.) surface wave suppression by a GaAs superstrate on a GaAs substrate, $n_1 = 3.6$ b.) surface wave excitation GaAs interface, $n_{air} = 1$ and $n_{GaAs} = 3.6$

Figure 2.22b illustrates that the majority of the loss occurs in the near vicinity

of the source. To retain half the power for broadband operation a superstrate needs to be placed close to the source ($< 40\ \mu m$). The superstate solution is not ideal for many reasons (practicality, reflections, and cavity effects); fortunately, the Coplanar Strip (CPS) waveguide discussed in the following section eliminates this issue without the need of a superstrate.

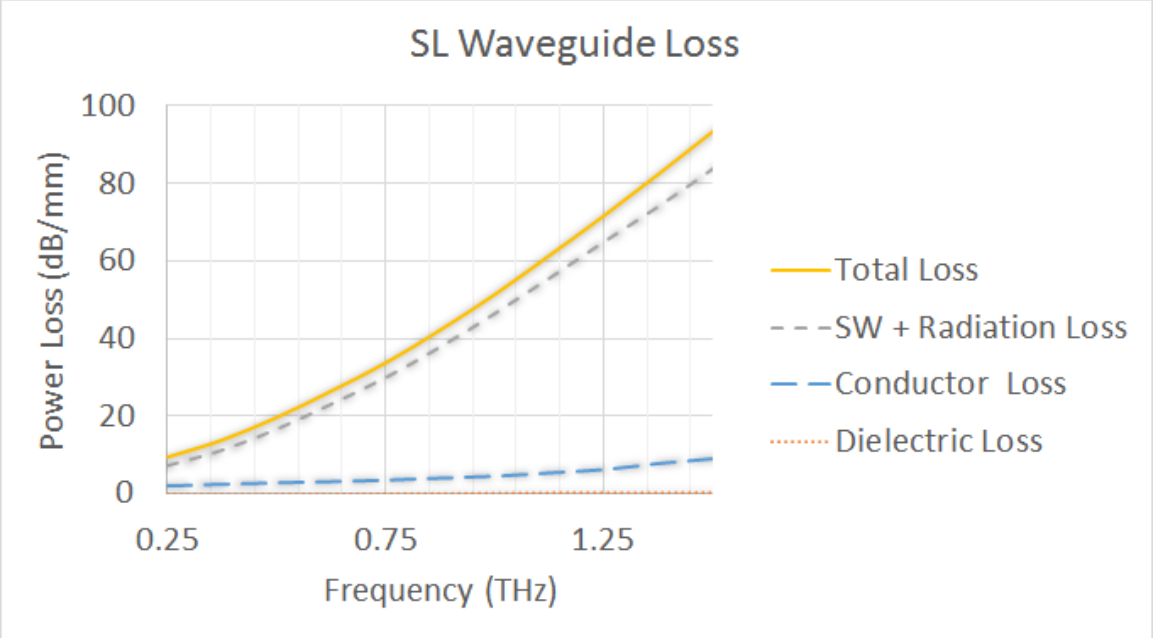

Figure 2.23: FEM simulation plotting the various power loss for a slotline waveguide on GaAs (no superstrate). $S = 5\mu m$.

2.4.4 Coplanar Strip Waveguide

Coplanar Strip (CPS) waveguides can be classified as a special case of a slotline waveguide. For a CPS waveguide, the in-plane metalization does not extend to infinity and is truncated at a finite width, W. Figure 2.24 illustrates the cross-section of a CPS waveguide.

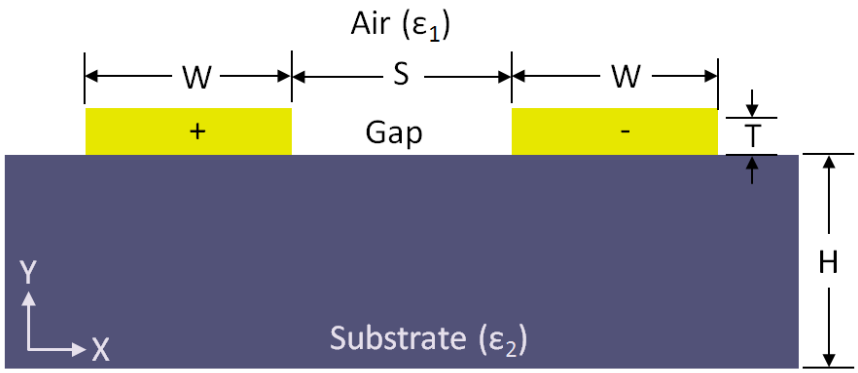

Figure 2.24: CPS cross-section

Unlike slotlines, closed-form expressions exist for CPS waveguides [16]. Two analysis techniques are available for the CPS waveguide: the quasi-static approximation [20], and full-wave analysis [21]. The closed-form full-wave equations presented in [16] are not applicable to THz region and should only be used as an initial approximation; a field solver is strongly recommended for detailed analysis.

Quasi-Static Approximation

The quasi-static approximation [20] gives an estimation for the capacitance and characteristic impedance for a CPS waveguide assuming the thickness, T, is 0:

$$C = \epsilon_0(\epsilon_1 + \epsilon_2)\frac{K(k_1')}{K(k_1)}\left[\frac{F}{m}\right] \tag{2.41}$$

$$Z_0 = \frac{\eta_0}{\sqrt{\epsilon_{re}}}\frac{K(k_1)}{K(k_1')}\,[\Omega] \tag{2.42}$$

where $\eta_0 = 376.730$, $k_1 = \frac{S}{S+2W}$, $k_1' = \sqrt{1-k_1^2}$, $\epsilon_{re} = \frac{\epsilon_1+\epsilon_2}{2}$, and K is the complete elliptic integral of the first kind. Figure 2.25 plots the capacitance and characteristic impedance for CPS waveguide.

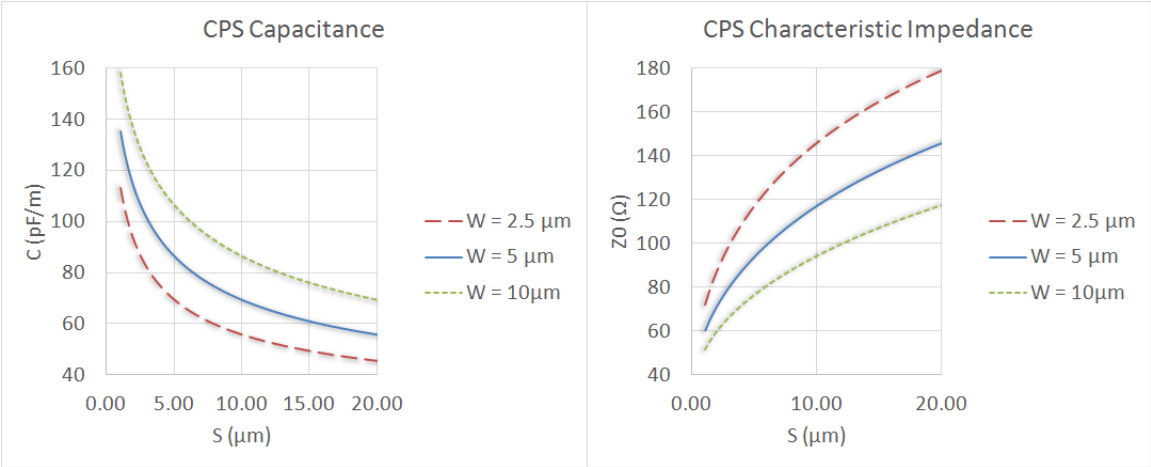

Figure 2.25: CPS unit capacitance and characteristic impedance given: $\epsilon_1 = 1$ and $\epsilon_2 = 12.96$

Fullwave Analysis

The fullwave analysis was accomplished using Ansys HFSS for determining frequency-dependent parameters such as waveguide dispersion and loss. Losses to be determined are the dielectric losses, conductor losses, radiation, and surface wave losses.

For THz applications we want the active area to be as small as possible to ensure sufficient free-carrier generation and minimal radiation. For these reasons the analysis will use the following parameters: S=W=5μm, H=350μm, and $T = 0$.

Dispersion

Guided mode dispersion is illustrated in Figure 2.26 by plotting the effective refractive index, $n_e = \beta/k_0$. Referring to Figure 2.26, n_e increases rather linearly with respect to frequency, which implies that surface waves are not heavily excited. To note, the previously specified quasi-static first-order approximation: $n_e = \sqrt{\frac{\epsilon_1+\epsilon_2}{2}} = 2.64$, is relatively close to the simulated values.

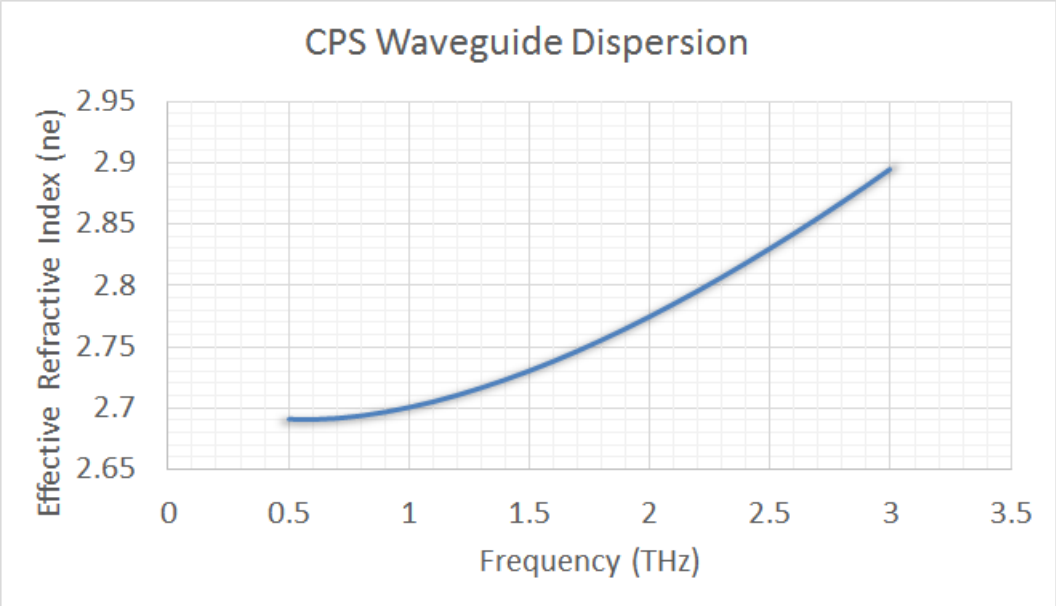

Figure 2.26: Dispersion obtained from FEM simulation for CPS waveguide on GaAs substrate. $\epsilon_r = 12.96$, S=W=5μm, H=350μm, and $T = 0$

Losses

The CPS waveguide is subject to four types of losses: conductor losses, dielectric losses, surface wave losses and radiation losses. We are concerned with the $f = 0.3THz \rightarrow 3THz$ range on a GaAs substrate ($\epsilon_r = 12.96$), the guided wavelength will reside in and around the $\lambda_g \approx 300\mu m \rightarrow 30\mu m$ range. To preview to the results of the following discussions Figure 2.27 illustrates the relative contributions for all the loss sources.

Conductor Loss:

As with all metallic waveguides, conductor loss is primarily dependent on the material conductivity and surface current density. Analysis of the S/W ratio is required to determine the minimum conductor loss, according to [16] this optimum value is roughly S=3W. Our design utilizes S=W; therefore we have a slightly higher conductor loss, but a much smaller radiation loss.

Dielectric Loss:

As with the slotline, the dielectric loss is dependent on the dielectric loss tangent and frequency. For our case, GaAs substrate given $f < 1.5THz$, the dielectric loss

tangent is roughly, $\tan\delta = 0.00085$. For these values the dielectric loss resides in the $\alpha_d < 0.5dB/mm$ range which is negligible in comparison to the other sources.

Surface Waves and Radiation Loss:

The CPS waveguide has finite width conductors which ensures the surface current is directed in the propagation direction. This results in minimal surface wave excitation and radiation. This is the key benefit of the CPS waveguide and will be discussed in the next section.

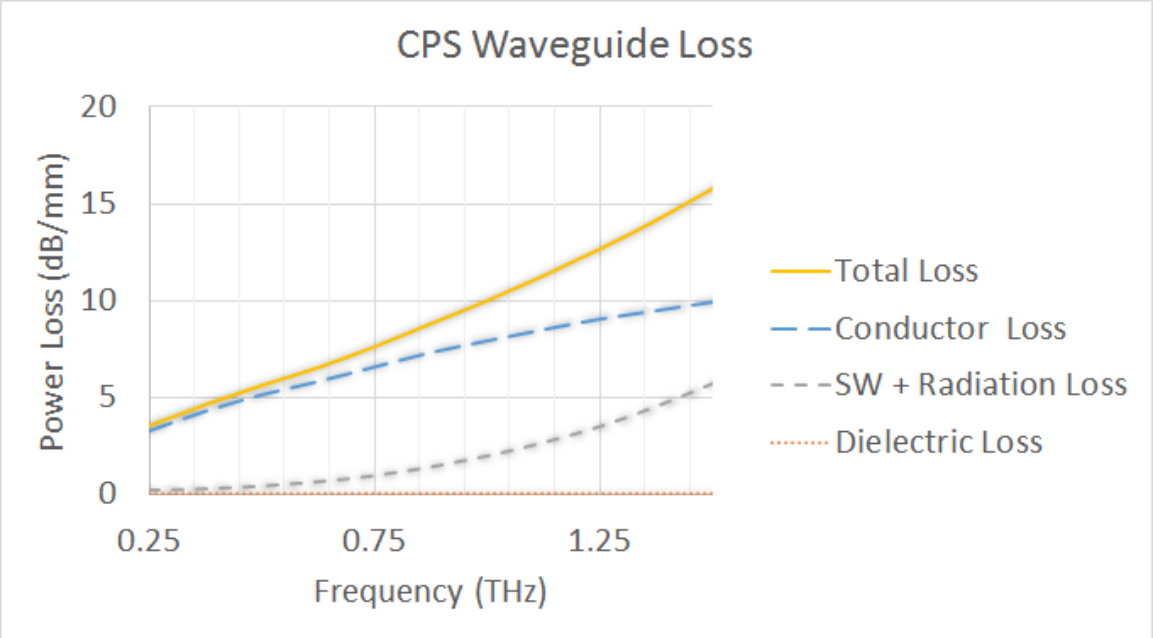

Figure 2.27: Summary of CPS waveguide loss sources with the following parameters: $S = W = 5\mu m$, $T = 0$, $H = \infty$, and $\epsilon_r = 12.96$.

2.4.5 CPS and Slotline Waveguide Comparison

Both the Slotline (SL) and Coplanar Strip (CPS) waveguide are capable of transmitting THz signals using a single-sided metalization on a dielectric substrate. As discussed in the previous sections both waveguides are subject to losses: conductor loss, dielectric loss, radiation and surface wave loss. We will investigate the differences between the two waveguides; the results will show that the CPS waveguide is superior when operated on a dielectric substrate, and due to practical reasons, a slotline is superior when the dielectric substrate is absent.

The CPS waveguide is superior to a slotline due to minimal surface wave and radiation loss. It has been proven by [18] that TE surface waves cannot be excited in the absence of a transverse surface current component (J_x in Figure 2.28). Comparison of Figure 2.28a and Figure 2.28b reveals that the slotline will have the larger J_x component; therefore, it is susceptible to exciting the lossy TE surface modes. Figure 2.29 illustrates the simulated surface current vector to complement Figure 2.28.

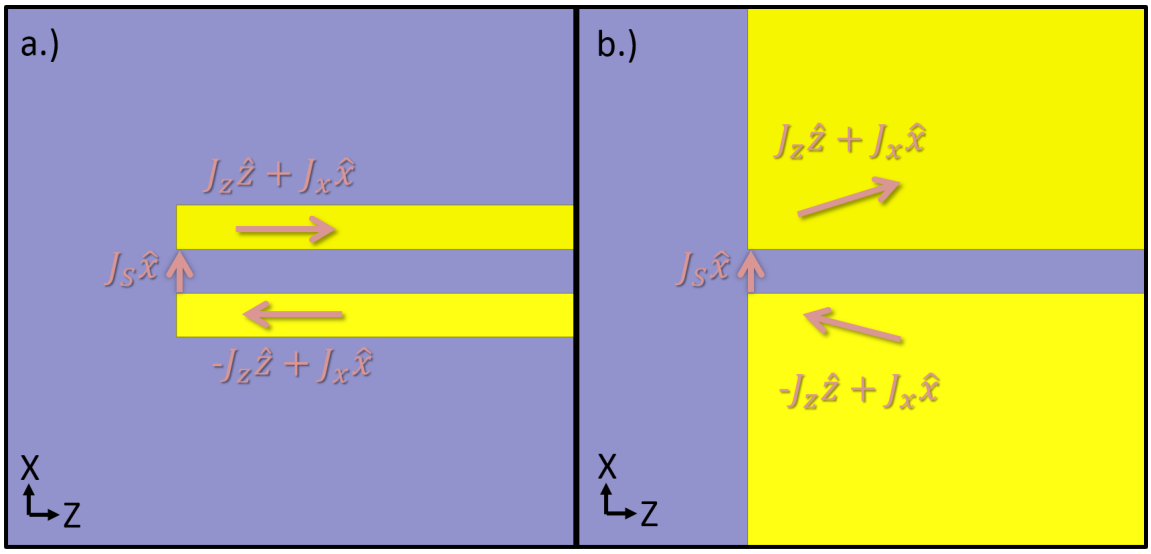

Figure 2.28: Surface current definitions, top down view of: a.) a CPS waveguide b.) a slotline

Figure 2.29b illustrates that the surface current is directed away from the source resulting in $J_x \approx J_z$. This results in coupling to surface modes, therefore energy is lost and unavailable to the guided mode. Figure 2.29a illustrates the CPS waveguide, observation reveals that J_x is minimal in comparison to the slotline and therefore with $J_x \approx 0$. Figure 2.29 plots the total loss for both the slotline and CPS waveguide obtained by FEM simulation. The CPS waveguide is more efficient than a slotline on a dielectric substrate: at f = 1 Thz, $\alpha_{CPS} = 9.8dB/mm$ and $\alpha_{SL} = 53.7dB/mm$.

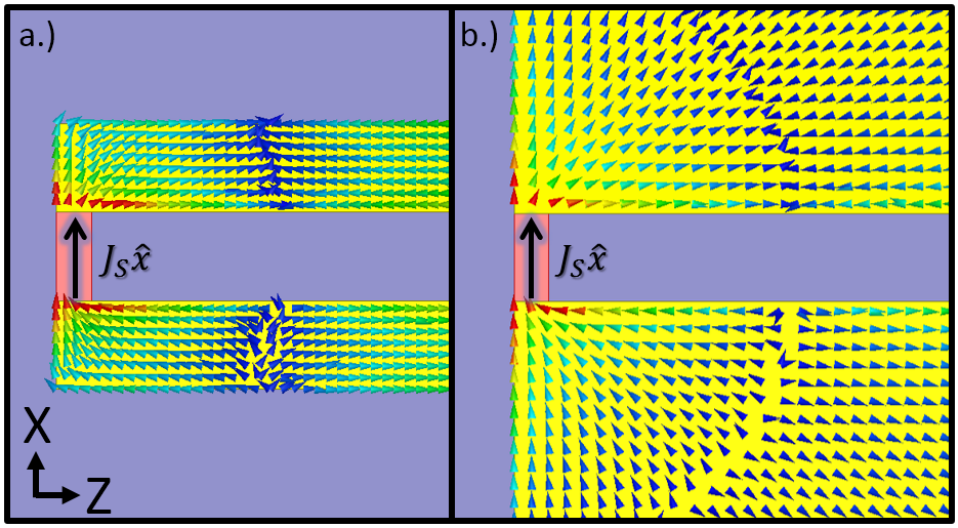

Figure 2.29: FEM simulation illustrating $\vec{J}_{surf}$ at f = 2 THz on GaAs ($\epsilon_r = 12.96$) for a: a). CPS waveguide b.) slotline

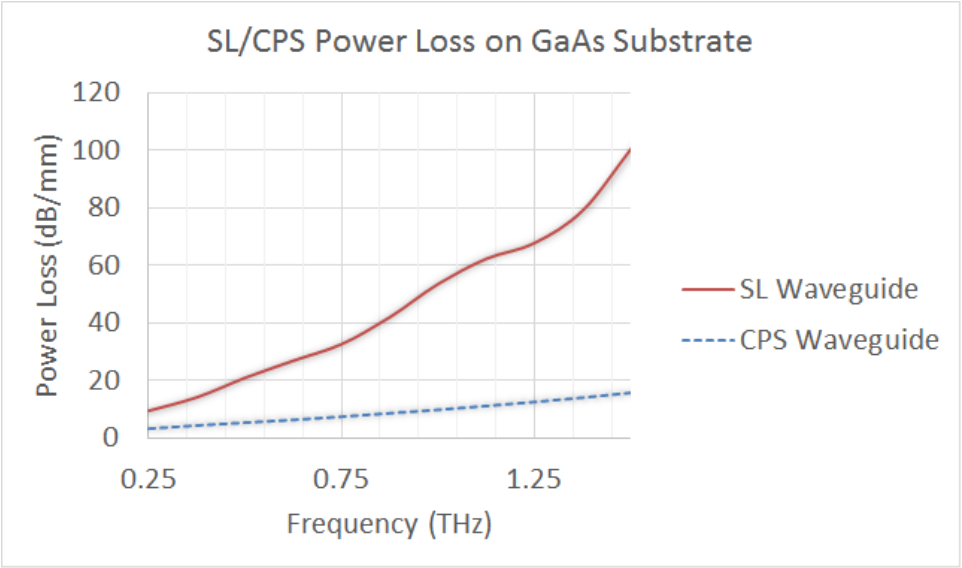

Figure 2.30: FEM power loss simulation for slotline and CPS waveguide on GaAs substrate ($\epsilon_r = 12.96$) given $S = W = 5\mu m$ and $T = 0$

Surface modes and substrate radiation do not exist when a dielectric substrate is absent, therefore the slotline and CPS waveguides will have comparable losses. Figure 2.31 illustrates the slotline and CPS waveguide power losses in the absence of a dielectric. The slotline waveguide power loss is still slightly more than the CPS

waveguide's, this occurs because the slotline surface current distribution is highly localized on the edge of the conductor. The CPS waveguide has a more distributed current density (across W) and therefore we expect a lower conductor loss.

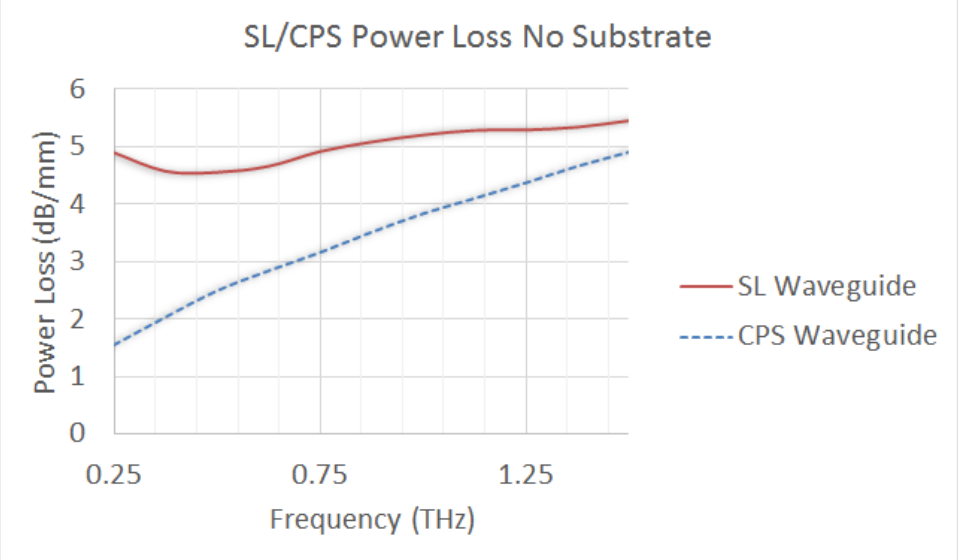

Figure 2.31: FEM power loss simulation for slotline and CPS waveguide without a substrate ($\epsilon_r = 12.96$) given $S = W = 5\mu m$ and $T = 0$

In free-space we obtain comparable power losses between the slotline and CPS waveguide; therefore we may choose to substitute one for the other depending on the situation. For practical reasons slotlines are easier to manufacture because they can be built by etching a gap into a planar conductor; for example, a standard copper sheet can be etched by femtosecond laser micromaching to design a THz slotline waveguide.

2.4.6 Thick Slot Waveguide

Figure 2.20 illustrates a cross-section of a slotline with exaggerated dimensions. A typical requirement for a slotline is that $T \ll S \ll \lambda_0$; the thick slot waveguide does not satisfy these conditions.

The thick slot waveguide can be classified in-between a parallel-plate waveguide and a SL waveguide. This design is desirable in applications where a low-loss free-space slotline-like waveguide can be used. The primary reason for investigating a thick slot waveguide is because it can be manufactured using femtosecond laser microma-

chining. A structure similar to the thick slot waveguide has been investigated by [22] where the edge of a cleaved, polished, gold plated Si wafer served as the waveguide conductors.

The thick slot waveguide is not susceptible to dielectric or surface wave losses because it not operated on a dielectric substrate. Therefore conductor and radiation losses dominate waveguide loss. Conductor loss can be minimized by increasing the separation, S, between the waveguide conductors. Figure 2.32 illustrates the power loss for the thick slot waveguide for various slot aspect ratios (S/T) at 1 THz. For small values of S/T, conductor loss dominates which is modeled using the equation for parallel-plate waveguide conductor loss:

$$\alpha_c = \frac{R_s}{\eta S}. \tag{2.43}$$

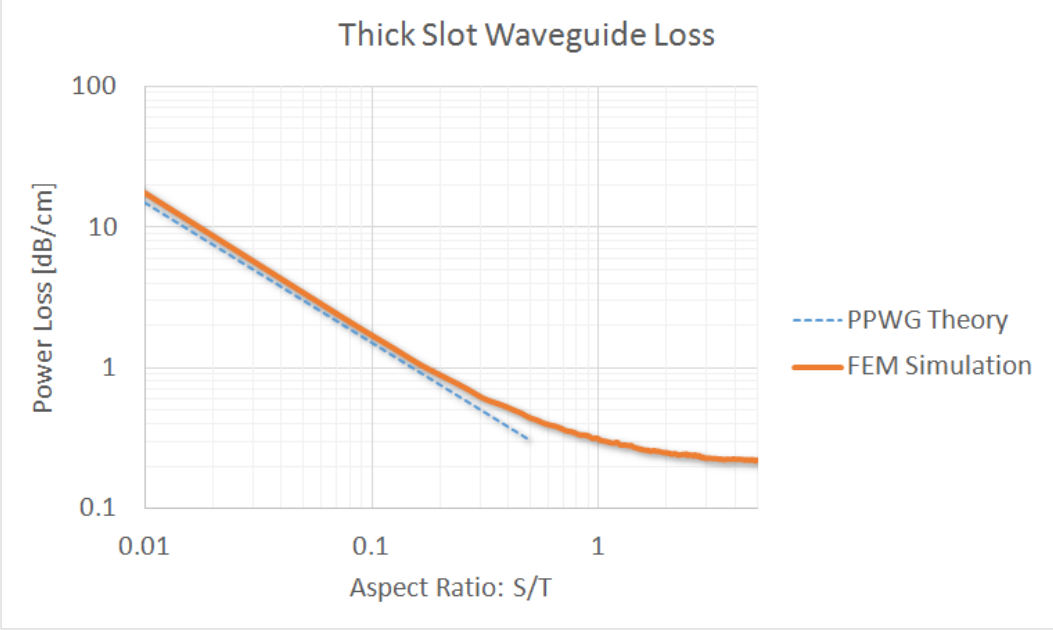

Figure 2.32: Power loss for a thick slot waveguide for various S/T ratios at 1 THz (T=400μm)

Referring to Figure 2.32, we conclude that for S/T $>$ 0.2, the power loss will be less than 1dB/cm at 1 Thz which is much less than is achievable when a substrate is present. The thick slot waveguide is not modeled analytically because most approximations are invalidated by its S/T aspect ratio. For the purpose of this thesis FEM simulations are used to determine the thick slot waveguide parameters.

Chapter 3

THz Field Enhancement by Antenna Coupling to a Tapered Thick Slot Waveguide

This chapter is a reformatted copy of [1]. See [1] for the published paper.

Author Contribution - My contribution to the following paper includes: inventing the idea along with Dr. Darcie; conducting the experiments and simulations; writing the manuscript with exception of Section 3.4.1 which was written by F. Ahmed, and two paragraphs in the introduction which were written by Dr. Darcie.

Abstract - *We demonstrate experimentally the coupling of a THz beam into a laser-machined double-tapered thick slot waveguide operating between 0.3 and 2 THz. Simulation reveals that the THz field generated by a standard photoconductive antenna coupled to an undoped aspheric HRFZ-Si focusing lens can be enhanced by 30dB in the 40 μm taper waist, relative to a traditional Gaussian beam waist (at 1 THz). Analysis of the 8 dB insertion loss reveals positive implications for coupling between THz transceivers and in-plane-emitting antennas or low-loss THz waveguides.*

3.1 Introduction

Optical guiding and focusing mechanisms are commonly used in the Terahertz (THz) frequency domain. Reflective (metallic) or transmissive (typically silicon or Teflon) lenses are generally used in commonplace THz time-domain spectrometers to focus the

THz beam into a sample region. More recently, it has become desirable to increase THz field intensity beyond that which can be obtained using traditional Gaussian beam optics for sensitive spectroscopy and non-linear THz applications [23]. Previous studies have investigated tapered parallel-plate waveguides where the field confinement geometry is well defined [24, 23, 25] as a means of achieving sub-wavelength beam dimensions and hence high field intensities. For plate separations of 40 μm, enhancements of approximately 30 dB have been demonstrated [24].

Parallel-plate waveguides show promising characteristics, but they suffer due to complex construction and implementation. Parallel-plate waveguides are usually implemented by translating one or both waveguides plates using a micrometer stage, a technique that requires significant interaction and could not be simply integrated into a turn-key system. The thick slot waveguide presented here is capable of attaining similar performance, but with significant ease of construction.

Adiabatic field compression and expansion of parallel-plate waveguides has been demonstrated by others. Zhang, *et al.* [26] investigated a double-tapered parallel-plate waveguide which utilizes Si lenses to couple the THz field in and out of the waveguide. While the approach shows good results, it is subject to reflective losses at the lens interfaces and challenging alignment. Shutler, *et al.* [27] have developed a double-tapered parallel-plate waveguide without THz lenses utilizing cylinders. In this work we use a thick slot waveguide rather than a parallel-plate waveguide. Our structures can be manufactured easily with other planar circuit elements (resonators, filters, etc).

The novelty of the work presented in this paper is primarily associated with the simplicity and effectiveness of the tapered thick slot waveguide. Using femtosecond laser micromachining, efficient tapered thick slot waveguides can be accurately constructed and implemented.

In addition to enhancing the strength of the THz field, adiabatic waveguide tapers may provide other useful functions. Typical semiconductor THz sources and receivers have dimensions of typically a few μm. For example, a typical photoconductive antenna (PCA) has a gap width of less than 5 microns [28]. Active circuits operating at THz frequencies [29] use extremely small features sizes such that these oscillators or mixers are much smaller than the wavelengths of the signals to be generated. However, as has been demonstrated through numerous recent studies, low-loss waveguide propagation requires waveguide dimensions more comparable to the wavelength (i.e. 1 mm at 1 THz). Two-wire or parallel-plate waveguides of these dimensions are ca-

pable of propagation loss at 1 THz of less than 0.087 dB/cm [30, 31], substantially lower than for any waveguide with dimensions comparable to transceiver dimensions. Waveguide tapers offer an attractive means for coupling into and out of low-loss THz waveguides.

Another application for tapers is antenna coupling. A conventional PCA places the photoconductive gap at the center of a planar dipole or other planar antenna. Resulting radiation is emitted normal to and into the semiconductor surface and collimated or focused typically using a silicon lens at the back of the substrate. An alternative is to define an antenna aperture at the output of a slotline taper and to capture the emission in the plane of the semiconductor. Such in-plane-emitting antennas offer a wealth of design possibilities with potentially significantly reduced beamwidths, as demonstrated in many examples at microwave frequencies [32].

Similar taper structures are required for all three applications discussed above; enhancing field intensity, matching between small sources and larger waveguides, and defining in-plane antennas. Enhancing field intensity requires a two-sided taper to compress and re-expand an incident THz beam. The other two applications require just an expansion taper, which is just one half of the two-sided taper. Ideally, structures would convert between a photoconductive gap of a few microns and an aperture width or waveguide conductor separation of several millimeters. In the previously explored parallel-plate structures, the plate thickness is greater than the plate separation. While performance is potentially good, these structures are rather difficult to manufacture and implement into a system. Our preference is to consider a planar structure fabricated using a standard thin ($\approx 400\mu$m) copper sheet and laser machining to define the thick slot waveguide taper with high precision.

Section 3.2 will describe the individual components associated with developing a practical waveguide. Section 3.3 will describe the simulation techniques and results obtained for the waveguide taper. Section 3.4 will describe our experimental procedure and analyze the results. Section 3.5 discusses our results which exhibit good agreement between simulation and experiment. Section **??** concludes the paper with a brief summary and a forecast of the impact that this waveguide can have on other THz applications.

3.2 Tapered Thick Slot Waveguide

This section explains the design philosophy behind our tapered thick slot waveguides. After an introduction to slotlines waveguide (3.2.1) and the photoconductive antennas used to generate and detect the THz signals in our experiment (3.2.2), the design and fabrication of our waveguide is described.

3.2.1 Slotline Waveguide

A slotline waveguide is a printed or etched metalization on a dielectric substrate which is commonly used at microwave frequencies. A slotline is typically used since it only requires a single-sided metalization on a substrate. Alternatives, such as microstrip waveguides operate on a dielectric with a two-sized metalization. For most THz applications, fabrication, coupling, and loss (conductor and dielectric) limit the usefulness of microstrips. The slotline also has the added benefit that it doesn't require the field to exist in the dielectric because the field can exist in the air between the two metalizations; although, to note, the field fringes into the substrate. Slotlines on dielectric substrates are prone to high-frequency dielectric losses which originate from leaky-wave (or shock-wave) radiation; to mitigate the leaky-wave radiation loss, the slotline can be sandwiched between two identical dielectric substrates [31].

3.2.2 Photoconductive Antenna Basics

PCAs are one of the simplest and cheapest methods to generate broadband THz signals. In essence a PCA is a metalization on a high-mobility photoconductive substrate - typically GaAs, LT-GaAs, or InAs. Most commercial THz PCAs are constructed using LT-GaAs where the sub-ps carrier lifetime allows for use as either a transmitting or receiving antenna. The metalization is used to supply charge to the antenna that will be impulsed by a femtosecond laser which in turn emits a broadband THz field. Upon generation of the THz field, most of the radiation is transmitted pseudo-omnidirectionally into the substrate due to comparatively high dielectric constant. At the substrate/air interface at the back of the substrate a THz lens must be used to maximize useful power by overcoming the total internal reflection condition at the interface. The THz lens can either be focusing, collimating, or diverging. Figure 3.1 illustrates a typical THz transmitter mounted to a focusing lens.

This work uses commercially available PCAs coupled to an aspheric focusing lens as a source and detector of THz radiation. The source radiation is coupled into and received from the laser-machined tapered thick slot waveguide. Consideration is made, as discussed below, to match the taper aperture to the THz beam profile from the PCA.

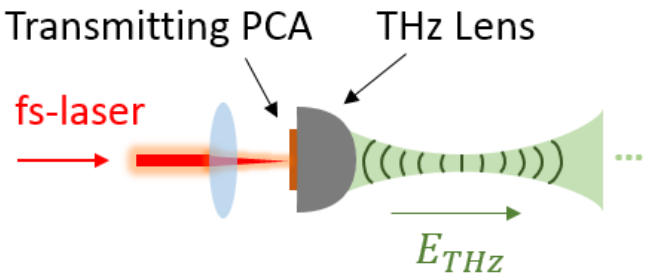

Figure 3.1: A THz field is generated by pulsing a biased PCA with a femtosecond laser. The transmitted field profile of the THz beam is dependent on the aspheric focusing Si THz lens.

3.2.3 Thick Slot Waveguide Tapers

Slotline tapers for THz applications have been analyzed in detail [33], but in the absence of strong experimental results publication of these analytical and simulation results is limited [34, 35]. Based on these prior findings, Figure 3.2 illustrates the tapered waveguide structure used in the current work. The waveguide consists of a planar input and output taper which are designed to match to the convergence angle of the PCA's Si focusing lens to optimize coupling. The waveguide's plate separation, $d(z)$, tapers from $5mm$ to $40\mu m$ and then tapers back to $5mm$. The waveguide was constructed using a high conductivity copper sheet with a thickness, w, of 0.4mm. The waveguide tapers were machined using a femtosecond laser as discussed later.

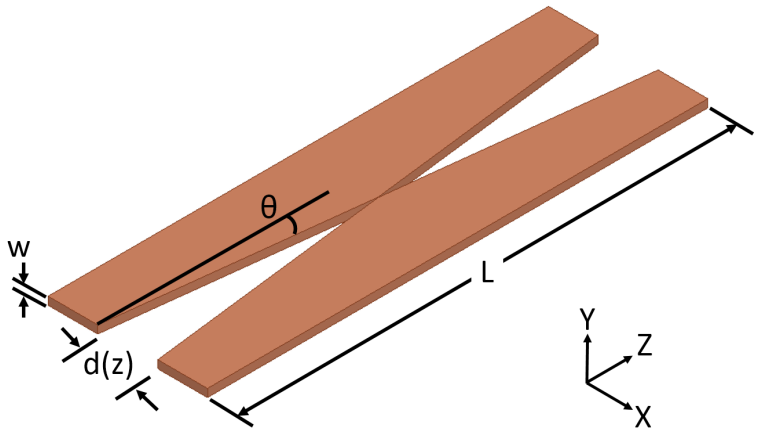

Figure 3.2: Overview of the thick slot waveguide structure used in the experiments. For our experiments: $d_{max} = 5mm$, $d_{min} = 40\mu m$, $w = 400\mu m$, $L = 40.4mm$, and $\theta = 7°$.

Waveguide dimensions have been selected to provide significant field enhancement and to minimize the frequency dependent conductor loss. Conductor loss has been estimated by Eqn. 3.1 [10] and Figure 3.3 illustrates the total integrated conductor loss for the entire waveguide. It can be observed that the loss is low and therefore should not pose significant detrimental effects to the waveguide's performance.

$$\alpha_c = \frac{R_s}{\eta_0 d(z)} = \frac{1}{\eta_0 d(z)} \sqrt{\frac{\omega \mu_0}{2\sigma_{Cu}}} \tag{3.1}$$

Our design differs from a slotline waveguide because the thickness of the metalization exceeds the wavelength for frequencies greater than 0.75 THz; hence the name, *thick slot waveguide*. Closed form solutions are not readily available for analysis of such a structure. Others who have investigated the effect of metal thickness on slotline operation have concluded that the metal thickness does not significantly affect the propagation constant[36]; this is consistent with the attenuation and pulse distortion seen in our experimental results discussed later.

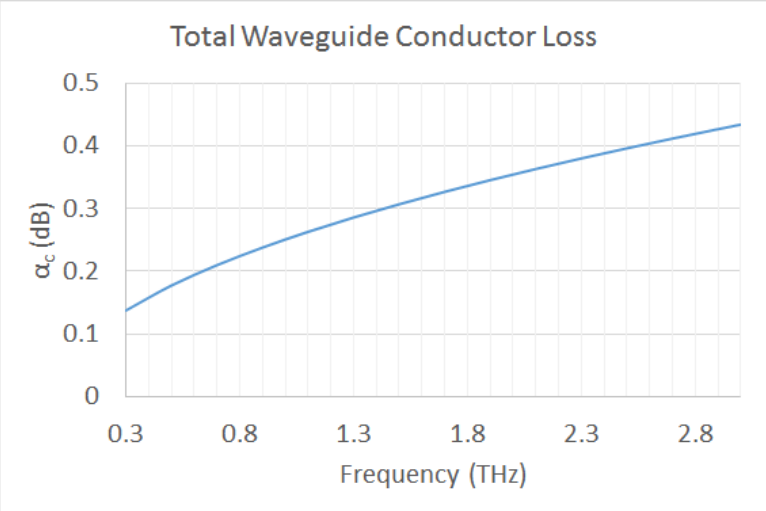

Figure 3.3: Worst case integrated conductor loss along the length of the waveguide modeled using the equation for a TEM parallel plate waveguide.

To mechanically support the structure illustrated in Figure 3.2 a Teflon brace was used which is illustrated in Figure 3.4; the bolts fastening the structure have been omitted for clarity.

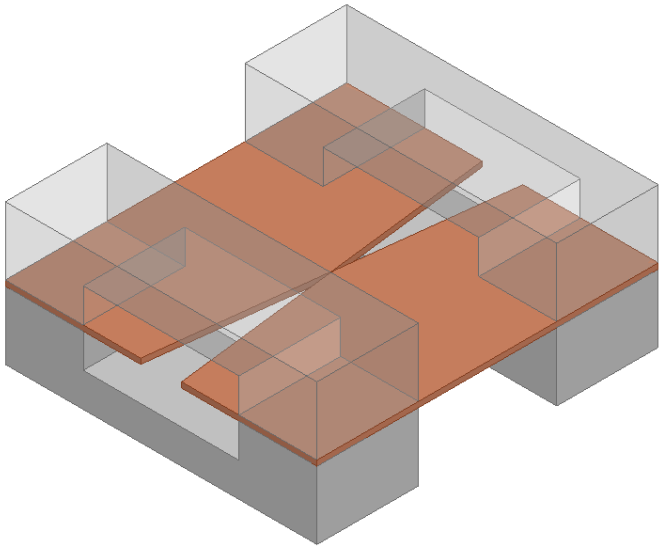

Figure 3.4: Copper tapered thick slot waveguide supported by two Teflon braces. Braces are bolted together (not shown) though the conductors.

3.3 Simulation

Simulations of the tapered waveguide structure were completed using Ansys HFSS with a combination of solution techniques; standard frequency domain Finite Element Method (FEM) and the transient analysis which utilizes the Discontinuous Galerkin Finite Element Method (DGTD). These solution types were selected due to their ability to accurately model geometries and closely model a THz pulse in the time domain.

The simulations were excited using various sources depending on the goal. Waveport excitation was used when well-defined conductor geometry permitted it. Incident wave (plane, Gaussian, spherical) excitation was used when it would closely model the experiment. Terminal excitations were used for transient simulations. Simulation boundaries were commonly set to PML regions due to their ability to minimize reflections.

Simulation validation was performed by comparing the solution to calculated parameters [10, 16] for simplified similar structures. For example, a comparison was made between analytical calculations for parallel-plate waveguide and the thick slot waveguide for small aspect ratios, $\frac{S}{T}$ (see Figure 2.32).

3.3.1 Field Coupling

Figure 3.5 illustrates the idealized field profile at the focal point of the THz lens which is representative of the maximum field intensity attainable. Figure 3.6 plots the Gaussian beam waist size, w_0, vs frequency using a THz lens with a convergence angle of 7°. Figure 3.7 illustrates the waveguide's TE field profile for a few discrete values of $d(z)$.

Optimum coupling exists between the Gaussian beam and the waveguide when the field overlap is maximized. The overlap integral (Eqn. 3.2 [3]) can be interpreted visually by overlaying Figure 3.5 onto Figure 3.7a and approximating the similarities between the two field profiles.

$$\eta = \frac{|\int \vec{E}_1^* \vec{E}_2 dA|^2}{\int |\vec{E}_1|^2 dA \int |\vec{E}_2|^2 dA} \tag{3.2}$$

Our estimation for sufficient coupling was to locate the focal point where the plate separation was equal to the beam diameter, $d(z) = 2w_0(2THz)$. This estimation could be enhanced by vigorous analysis and optimization of Eqn. 3.2 and the respective

co-directional and counter-directional coupled-wave equations. For this initial proof of concept design we did not deem this necessary due to the various complicated relationships which exist between the frequency dependent Gaussian beam wavefront and the fringing fields of the waveguide.

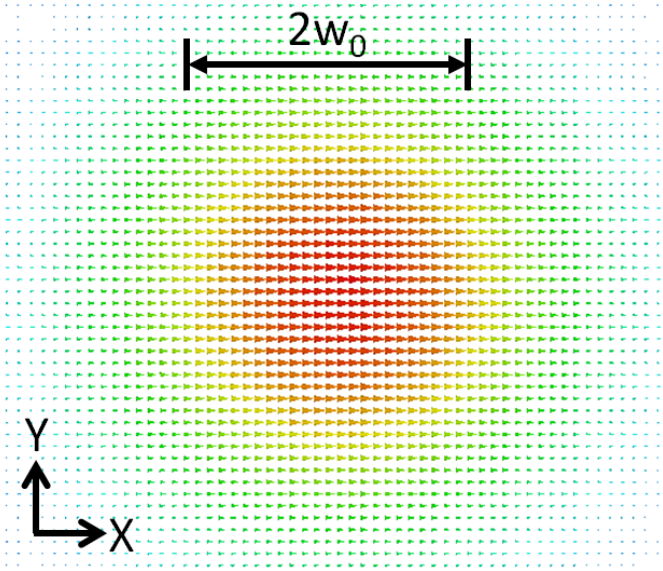

Figure 3.5: Ideal Gaussian beam E-field profile at the waist of the THz beam.

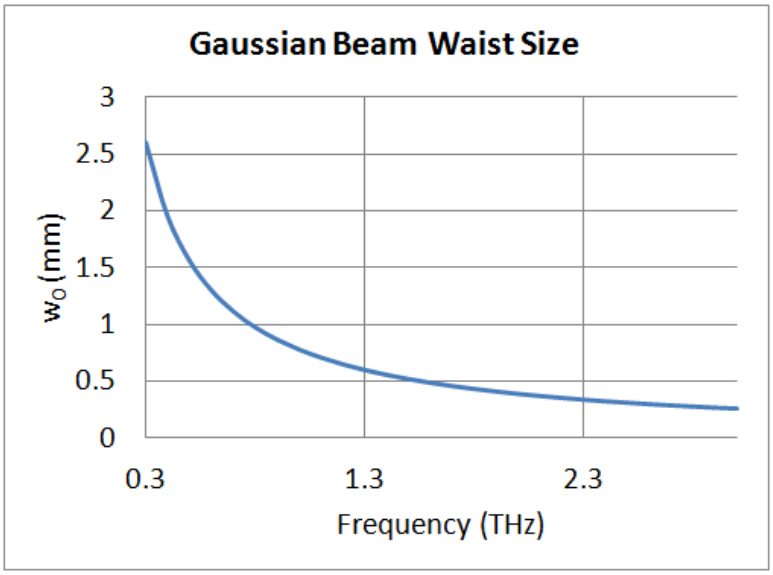

Figure 3.6: Gaussian beam waist size (w_0) vs frequency. Referring to Figure 3.5 it becomes apparent that as the frequency increases, the THz waist intensity increases.

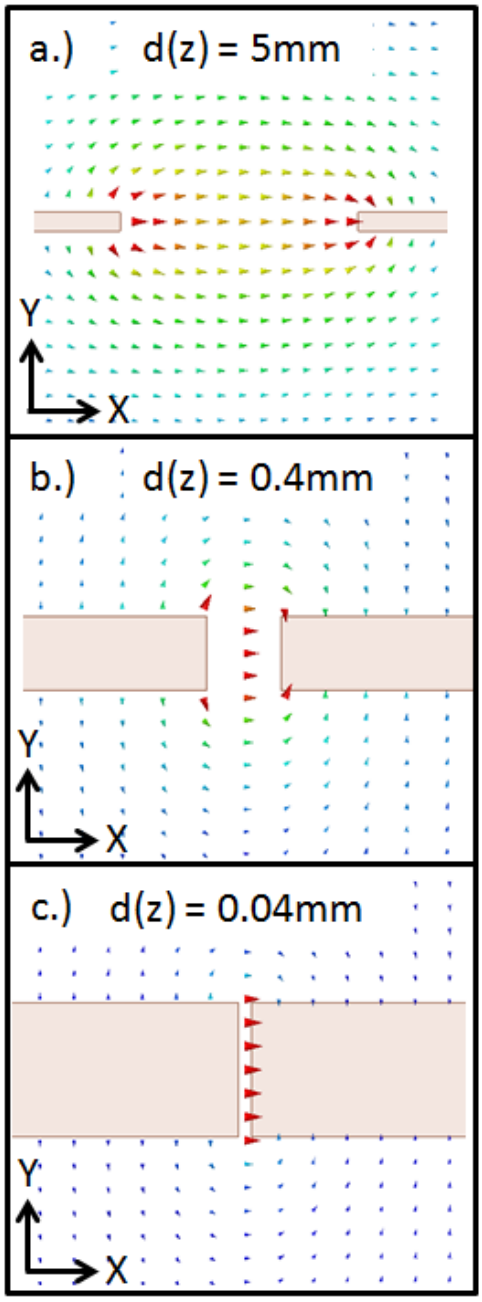

Figure 3.7: The E-field profile for various plate separations, d(z), which correspond to different locations within the taper. It can be seen from these plots that field confinement is dependent on the d(z). Also to note is that a.) and b.) are better approximations to the Gaussian field plotted in Fig 3.5, hence coupling is dependent on d(z).

3.3.2 Field Enhancement

Using techniques similar to [23, 24] we can provide field enhancement by coupling the radiated field into an adiabatic taper. For the waveguide, maximum field intensity occurs when the plate separation is at a minimum; similarly, for maximum field enhancement we want $d(z)$ as small as possible. Using laser micromachining techniques it is possible to obtain a minimum plate separation of around $20\mu m$, although for our initial experiments we used a plate separation of $40\mu m$.

Figure 3.8 pictorially illustrates the E-field enhancement achieved by the adiabatically tapering conductors. To provide a measure of achievable field enhancement the waveguide was implemented in a FEM simulation with a planewave excitation. Upon completion of the simulation Eqn. 3.3 was solved numerically where E_{in} and E_{out} represents the field at d_{max} and d_{min}, respectively.

$$\frac{E_{out}}{E_{in}} = \frac{V_{out}/d_{min}}{V_{in}/d_{max}} = \frac{d_{max}}{d_{min}} \frac{\int_{l_{out}} \vec{E}_{out} \cdot dl}{\int_{l_{in}} \vec{E}_{in} \cdot dl} \tag{3.3}$$

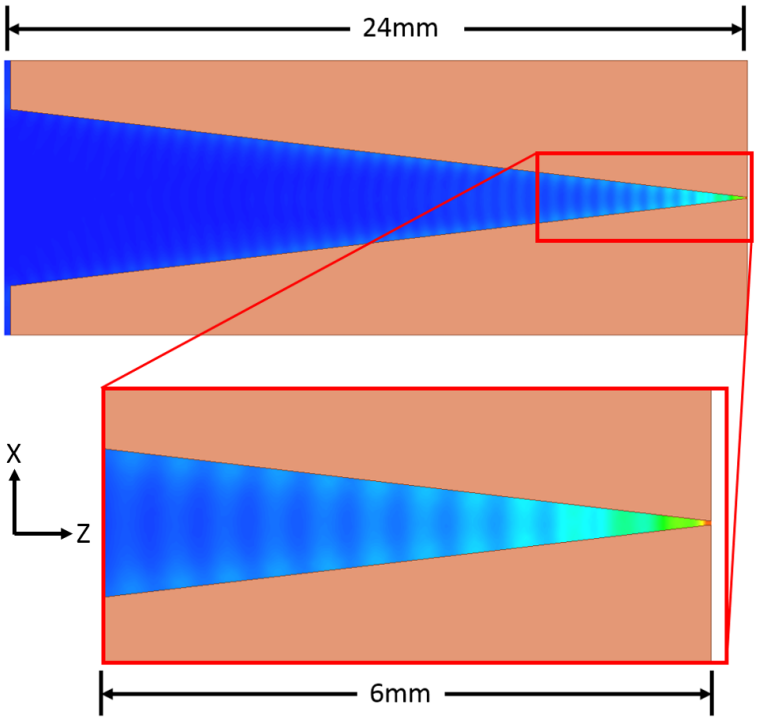

Figure 3.8: FEM simulation which demonstrates the E-field enhancement for f=0.3THz. Note that this illustration only shows half the waveguide structure.

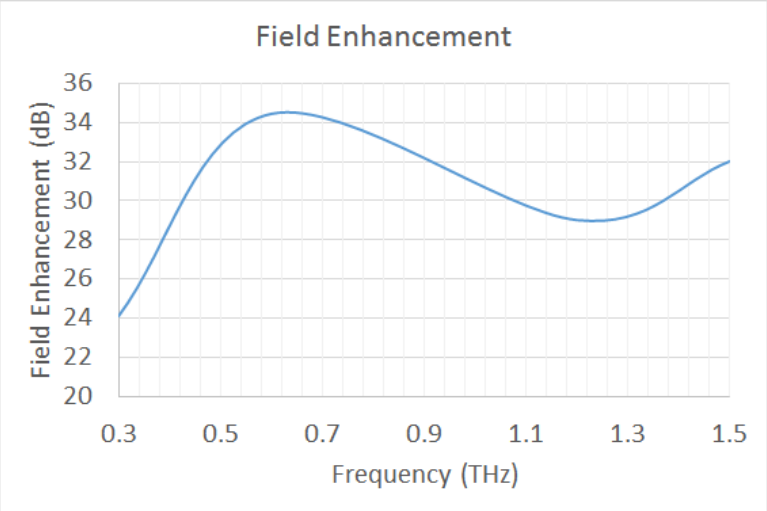

Figure 3.9: FEM field enhancement simulation for f=0.3-1.5 THz for $d_{max} = 0.5mm$.

Due to the extremely large mesh sizes required to simulate the waveguide in its entirety, the simulation was truncated to $d_{max} = 0.5mm$, where in reality $d_{max} = 5mm$. This truncation means the simulation is simply an approximation, but it should not result in any significant errors since the quasi-TEM field profile is well defined between the conductors. Figure 3.9 plots the simulated results representing Eqn. 3.3, the average field enhancement is 30dB. Referring to Eqn. 3.3 the enhancement scales with d_{max}, so it can be assumed that the structure likely provides a greater field enhancement than the simulation suggests.

3.3.3 Radiation Pattern

The waveguide has similar characteristics to the Gaussian beam since the input and output taper angles are matched to the respective convergence and divergence angles. Also to note, it is rather important to maintain the divergence angle to ensure adequate focusing of the THz beam onto the receiver PCA. The main observable difference in the waveguide arises from the planar confinement geometry which doesn't affect the radiated field much, providing the waveguide width, $d(z_{out})$, is sufficient.

To demonstrate this idea, Figure 3.10 plots the simulated radiation patterns in the YZ-plane for a couple different values of the plate separation at the output. For values of $d(z_{out}) < w$ the radiation pattern is not as focused as for larger values where $d(z_{out}) > w$. Therefore a rather simple criterion exists: $d(z_{out}) \gg w$; for our experiments examined in the next section, $d(z_{out}) \approx 12.5w$. Due to the existence

of the bounding conductors, the radiation pattern in the XZ-plane (not illustrated) doesn't show similar beam deformation.

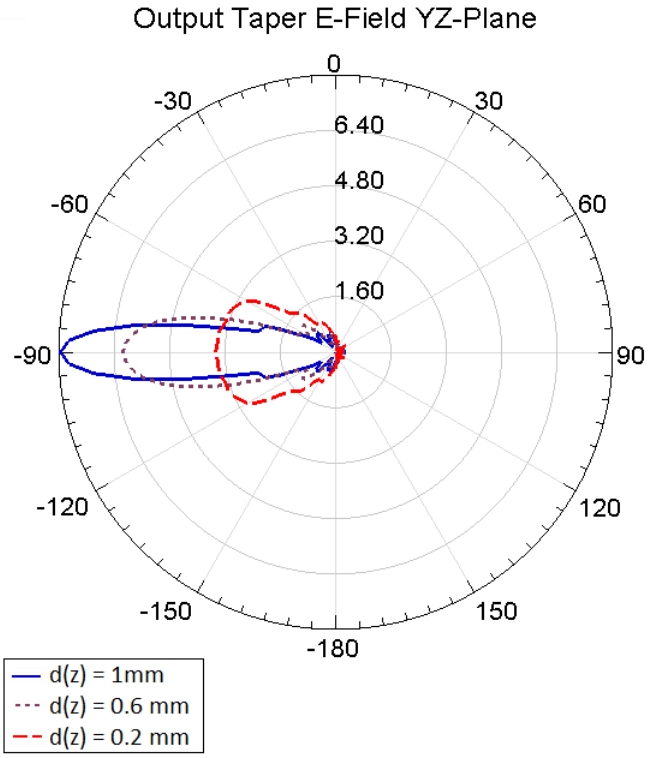

Figure 3.10: Radiation patterns at f=1 THz for various plate separations at the output taper. The plotted radiation patterns conclude to a rather intuitive result: the output taper should be designed to provide adequate directivity. This can be accomplished by tapering the conductors such that $d(z_{out}) \gg w$

3.4 Experiment

3.4.1 Waveguide Fabrication

A femtosecond laser (Spectra-Physics Ultrafast Ti: Sapphire laser) was used to fabricate the tapered waveguide structure on a 0.4 mm thick copper sheet. The kilohertz ultrafast laser operating at 800 nm has the pulse duration of 120 femtosecond and a maximum average output power of 1 watt. A computer controlled electronic shutter and a motorized power attenuator was used to deposit adequate pulse energy into the work piece. To reduce the heat-affected zone and restrict the width of the laser cut within 20 μm, the beam diameter was reduced from 6 mm to 2 mm using an iris

diaphragm. The laser beam was focused using a microscope objective lens (magnification: 20X, numerical aperture: 0.42). The sample was mounted on a computer controlled 3-axis stage and the software, LaserCAM, was used to generate scanning path of the laser head. The waveguide fabrication was done with an average laser power of 0.3 watts (pulse energy of 300 μJ) and scanning speed of 100 μm/sec using 20 passes, each vertically offset by 20 μm. To ensure desired machining accuracy, the micromachining process was monitored in-situ using a CCD camera.

3.4.2 Waveguide Testing

Figure 3.11 illustrates the experiment setup. We start by splitting a mode-locked femtosecond laser pulse into two paths; one for the transmitter, the other for the receiver. The transmitter path passes through an optical delay line which becomes translated to obtain the THz pulses temporal response. The receiver path is directed to the receiver PCA to gate the antenna; the output of the receiver PCA is connected to current input on a lock-in amplifier.

For our experiments copper plates were placed perpendicular to the waveguide to scatter surface waves potentially excited by the Gaussian beam, thereby ensuring our experimental measurements were the result of the confined waveguide fields.

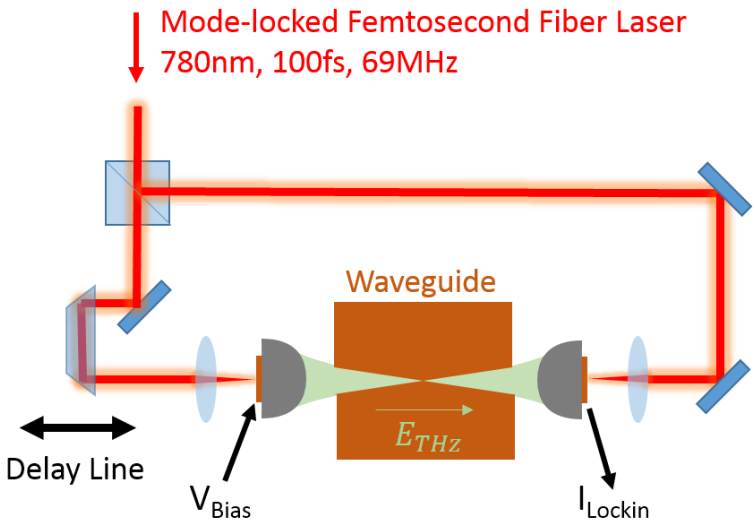

Figure 3.11: The experimental setup used is similar to a typical THz-TDS setup, a key benefit for the tapered thick slot waveguide. To test the waveguide, it is simply placed in between two PCA's with Si focusing lenses and then translated and rotated to achieve maximum transmission.

The experimental spectral response for the waveguide in Figure 3.12 demonstrates that the waveguide gives minimal pulse distortion and acceptable insertion losses ($\approx$ 8dB) when measured from peak THz current. As a speculation the majority of the loss likely occurs from sub-optimal coupling and scattering at the input and output of the waveguide. Coupling loss could be decreased by increasing the waveguide thickness, w. The coupling enhancement would originate from greater field matching in the overlap integral (Eqn. 3.2). Although greater coupling can be achieved, it comes at expense of decreased laser machining accuracy and more difficulty in integrating with small terahertz transceivers, trade-offs that require further consideration in future work. Even with an 8dB insertion loss, the waveguide is capable of providing a localized 30dB field enhancement which can be utilized to mitigate some of this loss irrespective of the coupling losses.

The dips in the spectral response in Figure 3.12 correspond to water vapor absorption peaks; out of convenience we typically do not run experiments in a purged environment unless doing sensitive spectroscopy. These peaks are useful to precisely calibrate our spectral response by correlating with data obtained from the HITRAN database [37].

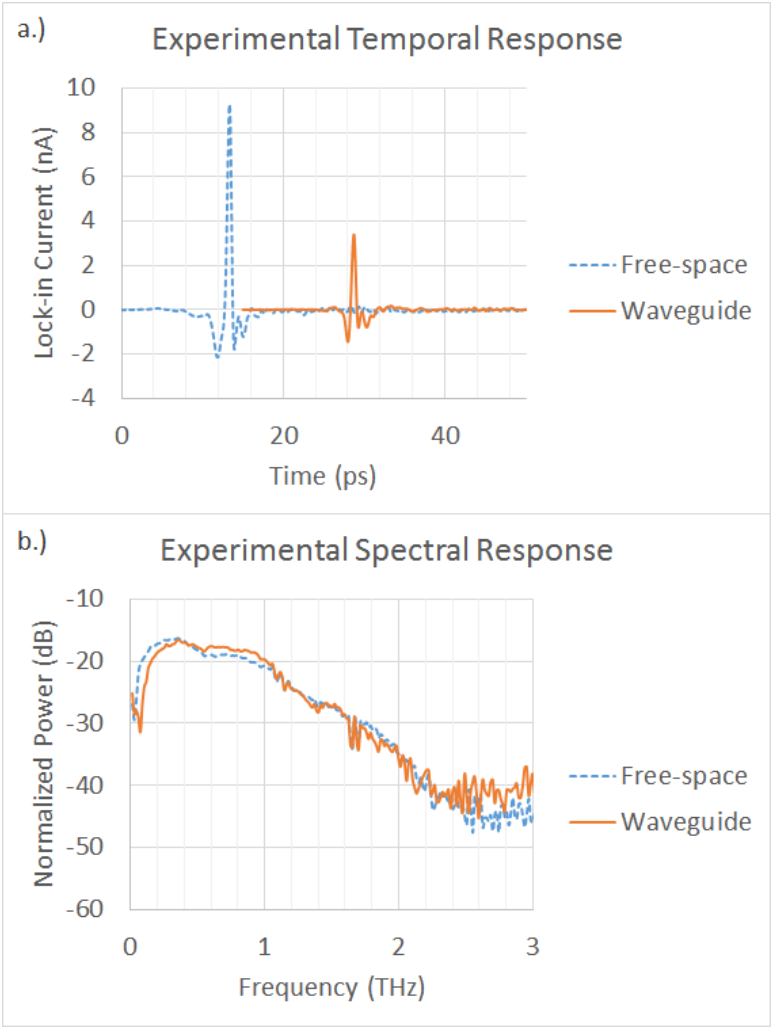

Figure 3.12: Experiment: The received pulse when transmitted though free-space as a reference, and the received pulse when transmitted though the thick slot waveguide.

A comparison between the experiment and simulation results is seen by inspecting Figure 3.12 and Figure 3.13. The main point to observe is that pulse broadening and ringdown are minimal in both experiment and simulation. This concept illustrates negligible dispersion and higher-order mode excitation; other literature [38] which focuses on exciting higher-order modes clearly illustrates the ringdown effect.

The differences between the experimental and simulation responses are attributed to different excitation sources and detection mechanisms. Due to software limitations the excitation source for the DGTD simulation is a Gaussian monopulse with a uniform wavefront; a cylindrical wavefront would provide a better approximation to the experiment. Experimental detection of the THz field is given by:

$\widetilde{J}(\nu) = \widetilde{\sigma}_s(\nu)\widetilde{E}_{THz}(\nu)$, where $\widetilde{J}(\nu)$, $\widetilde{\sigma}_s(\nu)$, and $\widetilde{E}_{THz}(\nu)$ are the Fourier transforms of the photocurrent, surface conductivity, and THz field [7]. The simulation directly measures $\widetilde{E}_{THz}(\nu)$ and is unaffected by the transient surface conductivity of the detector; thus a direct comparison cannot be made.

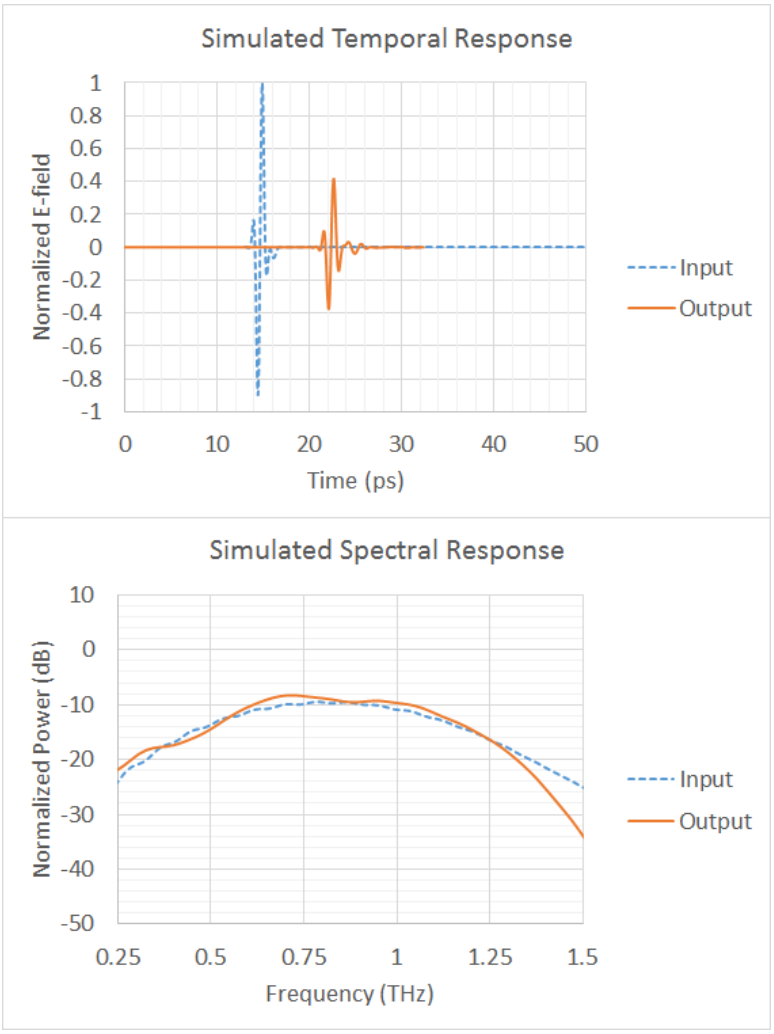

Figure 3.13: DGTD simulation: The pulse at the input to the waveguide as a reference, and the pulse at the output of the thick slot waveguide. The spectral response is normalized to one for both the input and output pulse.

3.5 Discussion

Using the tapered thick slot waveguide in combination with commercial PCAs enables a simple method to generate high THz field intensities. A number of applications

exist which can be enhanced by using this technique; such as spectroscopy, biomarker detection, non-linear THz applications, or high resolution surface imaging.

The results presented in this work show good agreement with theory; we have been able to successfully transmit THz pulses through laser machined waveguides. During the experiments it was found that alignment was simple in comparison to the free-space optics which we use regularly. This is likely due to the directive nature of the output taper as plotted in Figure 3.10. In the free-space optical setup two PCAs are roughly aligned onto one another, then carefully tilted and adjusted to maximize the THz signal. Introduction of the waveguide allowed us to steer the THz beam by gently tilting the waveguide without need of realigning the laser on the receiving PCA.

Figure 3.10 illustrates that the tapered thick slot waveguide can operate similar to an antenna. For our proof of concept design we didn't do any extensive antenna optimization or beam shaping since we wanted broadband operation. Future tapered thick slot waveguides designed for continuous wave (CW) operation could shift the focus towards antenna design where existing frequency dependent antenna theory could be utilized.

Using a similar concept to the previous paragraph, frequency-dependent waveguide structures could be machined into the tapered thick slot waveguide. For example, referring to the position of minimum plate separation, d_{min}, it can be found for similar geometries ($d(z) \ll w$) that eigenmodes are defined simply by existing parallel plate waveguide theory. Using mode-matching theory highly efficient filters, resonators, and power splitters can be machined into the waveguide and impedance matched to the tapered thick slot waveguide/antenna. Using a combination of these techniques antenna arrays can be developed to provide THz beam steering capabilities.

3.6 Conclusion

We have demonstrated experimentally our goal of coupling a commercial PCA to a tapered thick slot waveguide; the waveguide provides significant field enhancement over a simple silicon lens according to theory and simulation.

The tapered thick slot waveguide was designed specifically for field enhancement and coupling into and out of a commercial PCA [28]. Therefore this waveguide may not operate identically across all manufacturers' designs, but the design process demonstrated in the work can be easily adjusted for other THz optics.

The tapered thick slot waveguide simply consists of two tapers: adiabatic compression and expansion. This was done to provide a simple qualitative measure to the concept of planar waveguide structures. More advanced designs can be easily laser machined into planar conductors such as a filters or resonators. Using this waveguide in combination with microfluidic channels which traverse through the high field region could allow for simple small signature detection of both gas and liquid phase samples in a spectroscopy application.

Chapter 4

In-Plane Photoconductive THz Coupling to a Thick Slot Waveguide

4.1 Limitations of PCA Systems

Section 2.1.1 discussed THz generation utilizing a Photoconductive Antenna (PCA). The technique relied on radiating a field by generating a unidirectional current surge though planar conductors on a photoconductive substrate [8]:

$$E_{THz}(r,t) = \frac{A}{4\pi\epsilon c^2 r}\frac{\partial J(t)}{\partial t} \tag{4.1}$$

Inherently radiation is inefficient at transmitting energy between points. An analogy can be discussed: which works better, a cable or free-space radio transmission? Simply stated, they both have their benefits. Cables are used for efficient energy transmission, whereas, radio signals are useful when a direct or constant transmission path cannot be established. Certain THz applications, such as spectroscopy, do not require the benefits of a radiating source, therefore it would be beneficial to utilize a low-loss cable (or waveguide).

Current THz waveguides do not show exceptional transmission and coupling characteristics. Others investigated THz waveguides using plastic ribbons which experience dispersion resulting in significant pulse distortion [39]. Photonic crystal fibers have been investigated which experience similar pulse distortion characteristics [40]. Metallic structures such as two-wire [41, 30], single-wire [42], and parallel-plate

[13] waveguides have all been investigated which show promising loss characteristics ($< 0.7dB/cm$) and minimal pulse distortion, but they suffer due to poor coupling.

PCAs are inefficient; for an ideal setup, such as the one illustrated in Figure 4.1, at most, only ≈4.8% (or ≈13.2dB loss) of the generated THz power is transferred to the load antenna [43]. Ideal alignment is difficult and requires around $\approx 10\mu m$ translational accuracy as well as two-plane rotational accuracy at both the transmitter and receiver. Slight misalignments ($\approx$ 20 μm) will amplify the loss to undetectable levels (>100dB). In the presence of more advanced THz optics the alignment process becomes even more difficult.

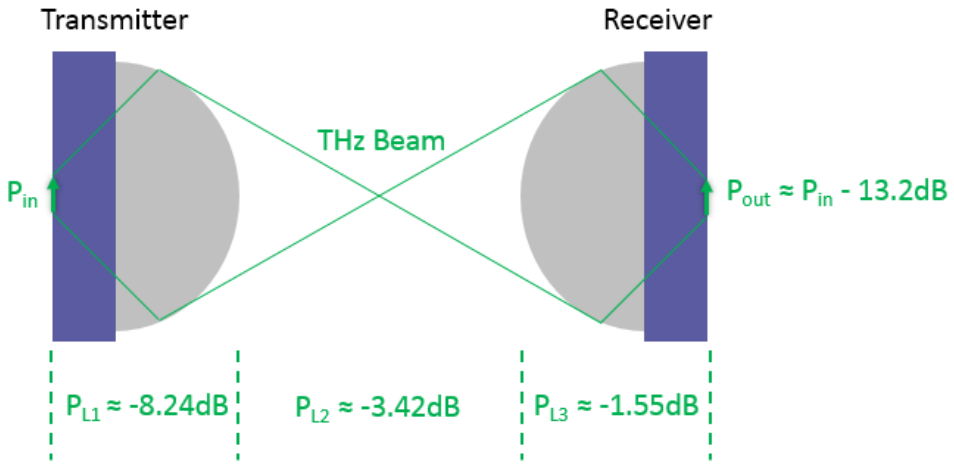

Figure 4.1: Optical loss associated with THz optics

PCAs are not well understood; most research surrounding PCAs is discussed in terms of relative differences. When absolute power measurements are performed (bolometer, golay cell) the frequency dependence is lost. The exact value of P_{in} in Figure 4.1 is almost always unknown, only estimations can be made using the equations discussed in Section 2.1.1. The accuracy of the approximation is limited by many factors: femtosecond carrier dynamics, optical coupling, lens aberrations and diffraction, contact resistance, THz beam alignment and interference, etc. If a transmission line is used in-place of a PCA, exact measurements are more viable and could provide greater insight into system parameters.

For sensitive spectroscopy and non-linear THz applications increased THz field intensity is desired. Using conventional THz beam optics the maximum field intensity is limited by inflexible lens parameters. A standard PCA HRFZ-Si focusing lens has a convergence angle of $\theta \approx 7°$; at 1 THz this corresponds to a Gaussian beam

waist size of 1.23mm. Therefore, at most, the THz field can be confined to an area of 4.76mm^2 limiting the maximum THz intensity. We will investigate thick slot waveguide coupling as a means to reduce the field confinement area to increase the THz intensity.

4.2 In-Plane Photoconductive THz Coupling to a Thick Slot Waveguide

The goal of this section is to develop a THz transmission line that efficiently transfers energy from a photoconductive THz source (not a PCA) to a detector. We will accomplish this task by utilizing in-plane photoconductive THz coupling to a low-loss thick slot waveguide.

In-plane photoconductive THz coupling expands and compresses the field from micrometer to millimeter scales using a waveguide. The waveguide should exhibit low-loss over its entire frequency range (0.3 - 3 THz) therefore frequency-dependent structures are avoided. Adiabatic tapering of conductors is utilized to provide smooth transitions at component interfaces to minimize localized field perturbations and radiative losses.

Figure 4.2 provides an overview of the THz waveguide structure which will be investigated. The structure consists of 6 main components: THz source, field expander, transmission waveguide, field enhancer, THz detector, and ceramic mount. The field expander, transmission waveguide, and field enhancer are machined from the same piece of copper, but their purposes differ so they have been separated into individual components.

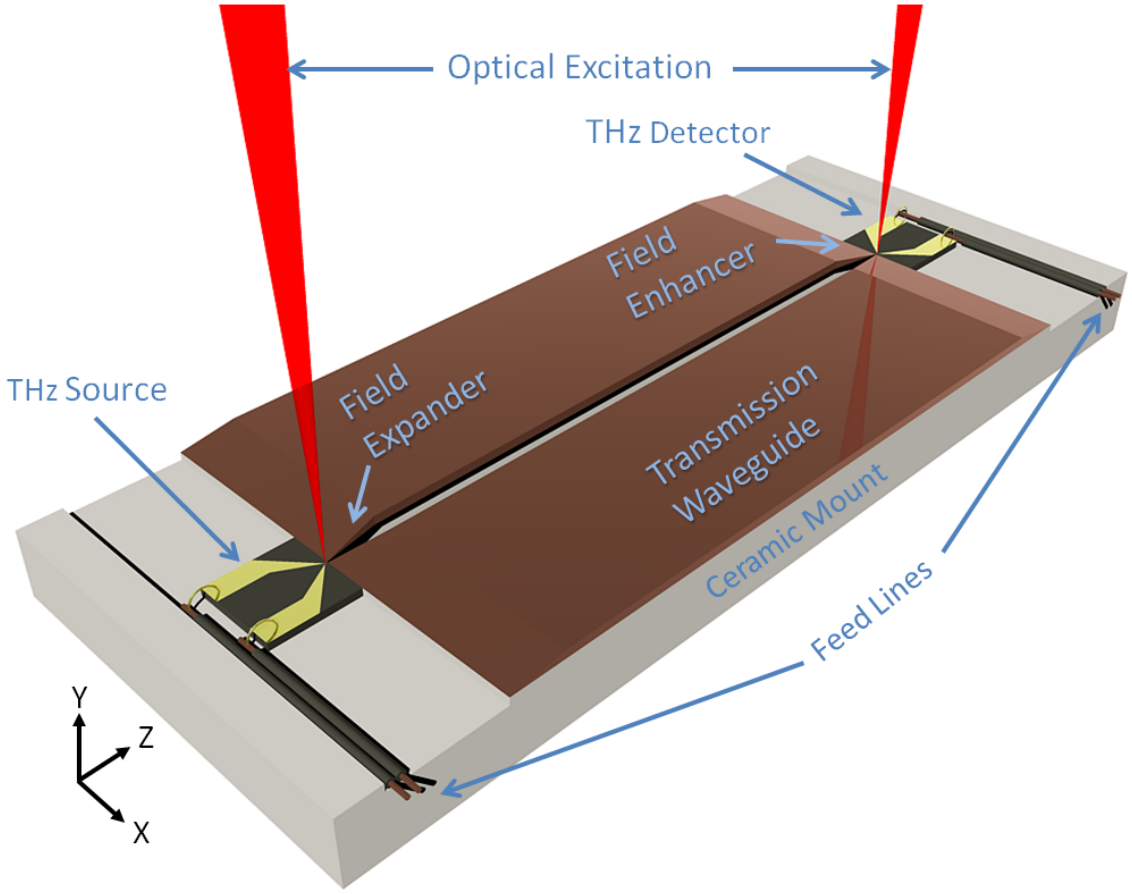

Figure 4.2: In-plane photoconductive source coupled to a thick slot waveguide

It is highly inefficient to transmit THz waves using waveguides on dielectric substrate due to the losses as explained in Section 2.4.5. To minimize the waveguide losses we can use the thick slot waveguide. The field expander, transmission waveguide, and field enhancer utilize a thick slot waveguide for this reason. The need for a dielectric substrate is eliminated by overhanging the edge of the waveguide in free-space (see Figure 4.3) while using the ceramic mount for mechanical stability.

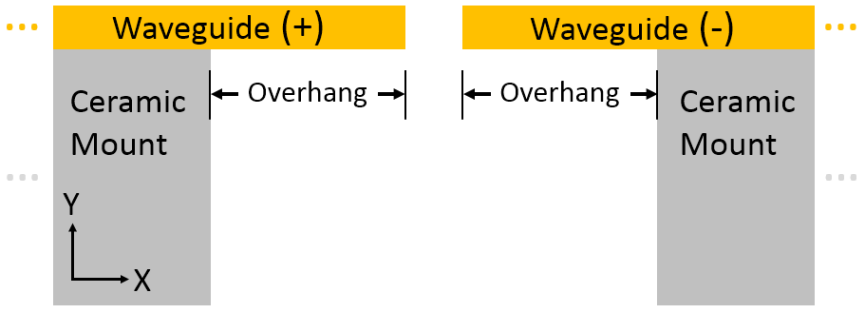

Figure 4.3: Thick slot waveguide overhang using the ceramic mount in the transverse plane

Figure 4.4 illustrates the operation principle behind the structure discussed in this section. The operation is similar to existing PCAs except the field is coupled to an in-plane low-loss thick slot waveguide instead of radiating into the substrate.

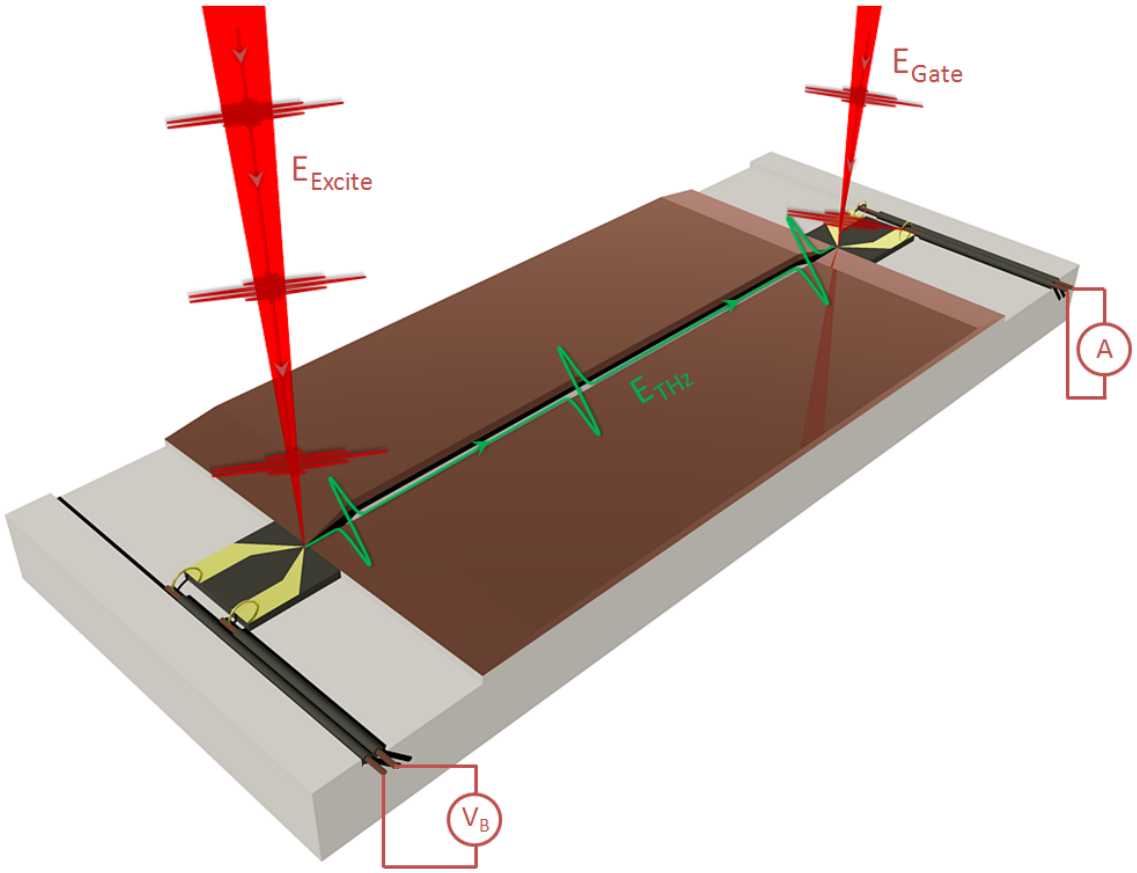

Figure 4.4: Principle of operation (pulse duty-cycle not to scale)

The waveguide structure components and respective interconnections can significantly affect the efficiency of the system. In the following sections an individual assessment of each component using FEM simulation will be performed.

As mentioned in Section 3.3, simulations in this chapter were also validated against analytical calculations for simplified similar structures. No simulation results are included in this thesis without basic validation.

4.2.1 THz Source

Figures 4.5 and 4.6 illustrate the THz source; the source is a biased photoconductive switch similar to the PCAs discussed in Section 2.1.1. The THz source presented here is designed to minimize the radiated fields by reducing the antenna length, S_A. The THz source operates as follows: a static field exists between the conductors due to an applied voltage (V_B), when excited by a femtosecond laser the active area resistance is decreased substantially ($R_{dark} \approx 2M\Omega \rightarrow R_{photo} \approx 10\Omega$) and quickly ($\Delta t_{R_{dark} \rightarrow R_{photo}} \ll 1ps$). This generates a voltage impulse on the conductors occurring at time scales proportional to THz frequencies.

Referring to Section 2.4.4 the CPS waveguide loss is in the order of $10dB/mm$ at 1 THz (see Figure 2.27); in other terms, half the power is lost in $300\mu m$. Therefore it is important to minimize L_1 (and S_{min}); in practice we select S_{min} based on femtosecond micromaching laser tolerances, which, for our substrate ($350\mu m$ thick GaAs) is $S_{min} = 20\mu m$. The E-field expansion angle (θ) is matched to the E-field expansion angle later discussed in Section 4.2.2; in short, we select $\theta \approx 10^\circ$. Using the $S_{min} = 20\mu m$ and $\theta = 10^\circ$ we find that $L_1 \approx 42\mu m$; therefore, we can expect a 0.42dB loss. As discussed earlier, this is better than the PCA THz generation output (15% or $P_L = 8.24dB$).

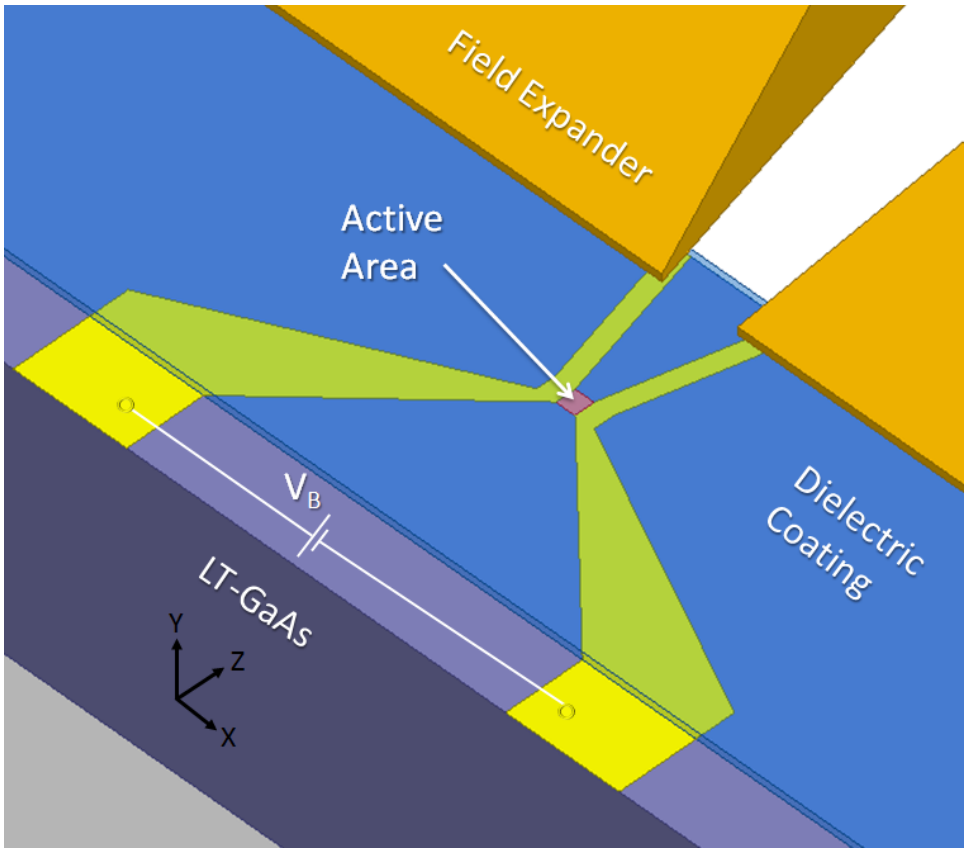

Figure 4.5: THz source

The dielectric coating on the LT-GaAs substrate serves two purposes: operation as a Direct Current (DC) block and an Anti-reflection (AR) coating. A DC block is required to pass THz frequency components while blocking the DC components supplied by the bias source. Referring to Section 2.1.4, a single layer dielectric interface can act as an AR coating to increase the optical transmission into the substrate.

The selected dielectric coating was 950 Poly(methyl methacrylate) (PMMA) [44] because it can be spin-coated over a large range of thicknesses ($20nm < T_{dielec} < 2\mu m$) on the substrate. After the PMMA is spin-coated on the substrate it is annealed to provide a rigid layer. The optical properties for PMMA ($n = 1.4846$ at $\lambda = 780nm$) are not ideal for an AR coating on GaAs although it is still capable of offering a transmission enhancement opposed to the absence of an AR coating (T=0.68). A $\frac{\lambda_d}{4}$ dielectric coating corresponds to a thickness of 131nm for a maximum transmission coefficient of T=0.96. Accurately spin-coating 131nm is difficult without extensive experimentation; therefore we will assume a ±30nm tolerance which corresponds to a minimum transmission coefficient of T ≈ 0.9.

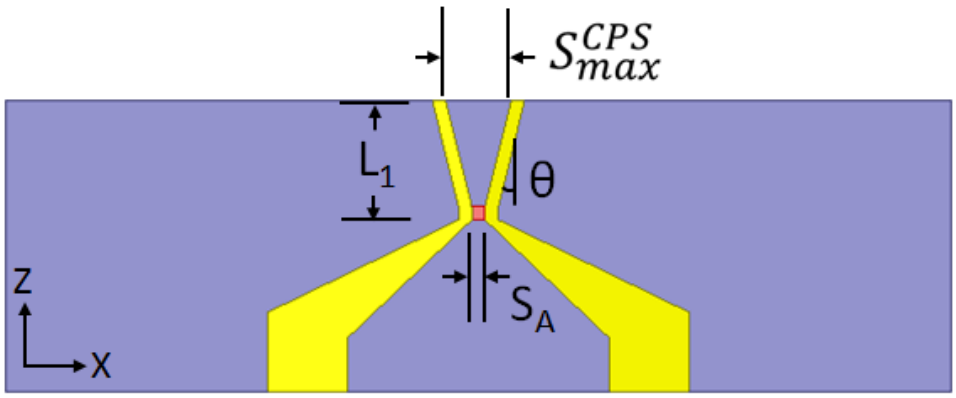

Figure 4.6: THz source dimensions (dielectric coating not illustrated)

Figure 4.7 illustrates the equivalent circuit for the THz source (ignoring capacitance) and R_A is the radiation resistance of the source.

$$i(t) = \frac{G(t)V_B}{G(t)R_A + G(t)Z_{in} + 1}, \tag{4.2a}$$

$$v(t) = i(t)Z_{in} = \frac{G(t)Z_{in}V_B}{G(t)R_A + G(t)Z_{in} + 1}, \tag{4.2b}$$

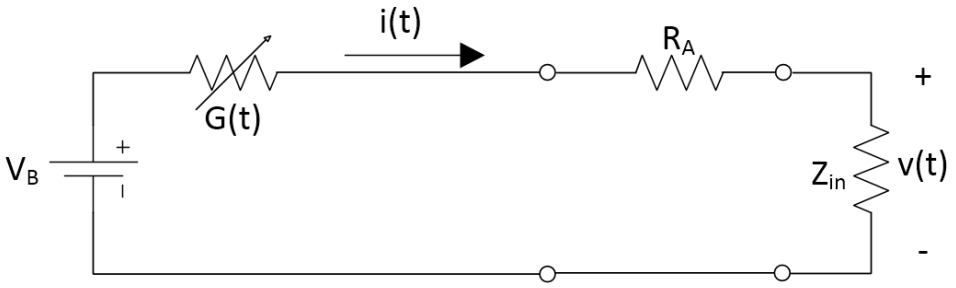

Figure 4.7: THz source equivalent circuit

The power delivered to the load is represented by rms current driving the waveguide, $i_{rms}^2 Z_{in}$. This equivalent circuit best describes CW THz, but can be used for pulsed THz as well. Simple conclusions for good power transfer can be obtained, such as: $R_A \ll Z_{in} \approx G_0^{-1}$, where G_0^{-1} is the inverse of the average photoconductance. Due to the extreme broadband nature of pulsed THz signals, the circuit model is not fully investigated as it only provides limited information.

4.2.2 Field Expander

Figure 4.8 illustrates the field expander used to adiabatically transform the THz field generated by the THz source from micrometer to millimeter scale dimensions. The purpose of this transformation is to ensure that the conductor loss in the transmission waveguide is insignificant.

Previous work has investigated adiabatic tapering for 2D slotlines [33] where the transverse E-field profile was tapered. They concluded that the E-field taper expansion angle (θ) should reside in the $10° < \theta < 40°$ region to provide significant CW power transmission at 1 THz. We investigate 3D tapering where both the transverse E-field and H-field profiles are transformed. We will analyze the simulated broadband transient response for both the E-field taper expansion angle (θ) and the H-field taper expansion angle (ϕ). Figure 4.9 plots the temporal and spectral response for various values of θ; where ϕ is given by Equation 4.3. It becomes apparent that smaller values of θ are desired due to lower losses and minimal pulse distortion. For larger values of θ undesirable effects can occur, such as excess radiation losses and possible excitation of higher order modes.

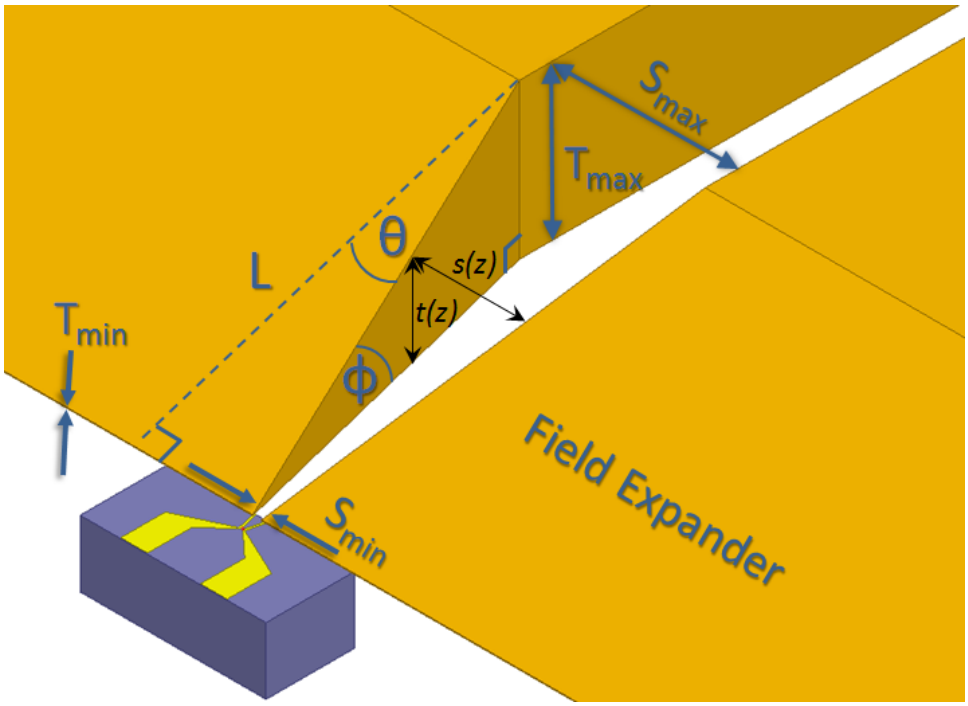

Figure 4.8: THz field expander

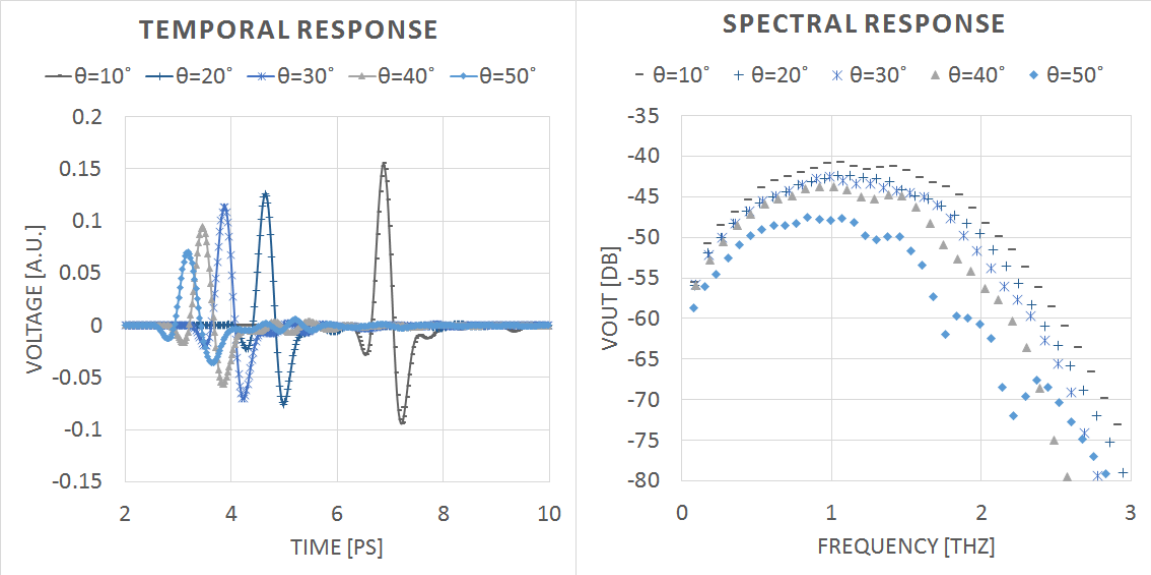

Figure 4.9: E-Field expansion angle analysis simulation results

For Figure 4.9 the H-field expansion angle is related to the E-field expansion angle by:

$$\phi(\theta) = tan^{-1}\left(\frac{2\Delta T tan(\theta)}{\Delta S}\right), \tag{4.3}$$

where: $\Delta T = T_{max} - T_{min}$ and $\Delta S = S_{max} - S_{min}$.

Referring to Figure 4.8 we define the plate separation and thickness by the following equations:

$$s(z) = S_{min} + 2z\,tan\theta, \tag{4.4a}$$

$$t(z) = T_{min} + z\,tan\phi, \tag{4.4b}$$

where: $S_{max} = s(L)$ and $T_{max} = t(L)$; $S_{min} = s(0)$ and $T_{min} = t(0)$.

To achieve a constant wave impedance along the length of the taper it may seem desirable to fix the $\frac{s(z)}{t(z)}$ ratio. This requires two separate taper lengths which can cause issues. For example, the introduction of another discontinuity along the length of the waveguide will increase radiative losses. For our initial experiments we will not attempt to maintain a constant wave impedance and select ϕ using Equation 4.3.

4.2.3 THz Source to Field Expander Coupling

Efficient coupling between the THz Source and Field Expander is desired to maximize the power transfer in the system. The maximum coupling efficiency occurs when the CPS and thick slot waveguide fields are closely matched. The coupling efficiency is determined by measuring the power transferred from the CPS waveguide to the thick slot waveguide using an FEM simulation. To simplify the coupling efficiency analysis the taper angles are ignored ($\theta = 0°$ and $\phi = 0°$) in the coupling region; Figure 4.10 illustrates the varied parameters in the optimization. Key parameters are $T_{dielectric}$, S_{max}^{CPS}, S_{min}, T_{min}, and L_C.

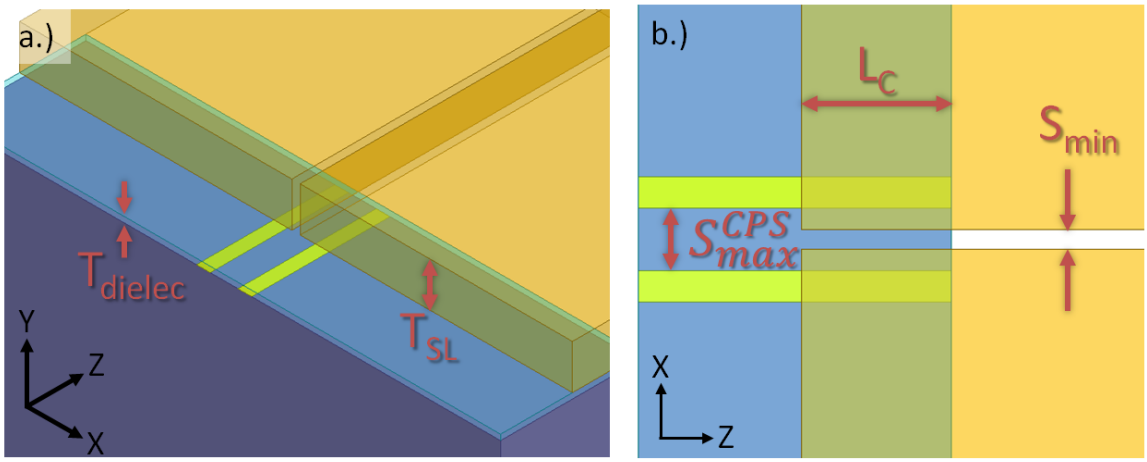

Figure 4.10: Coupling region definition

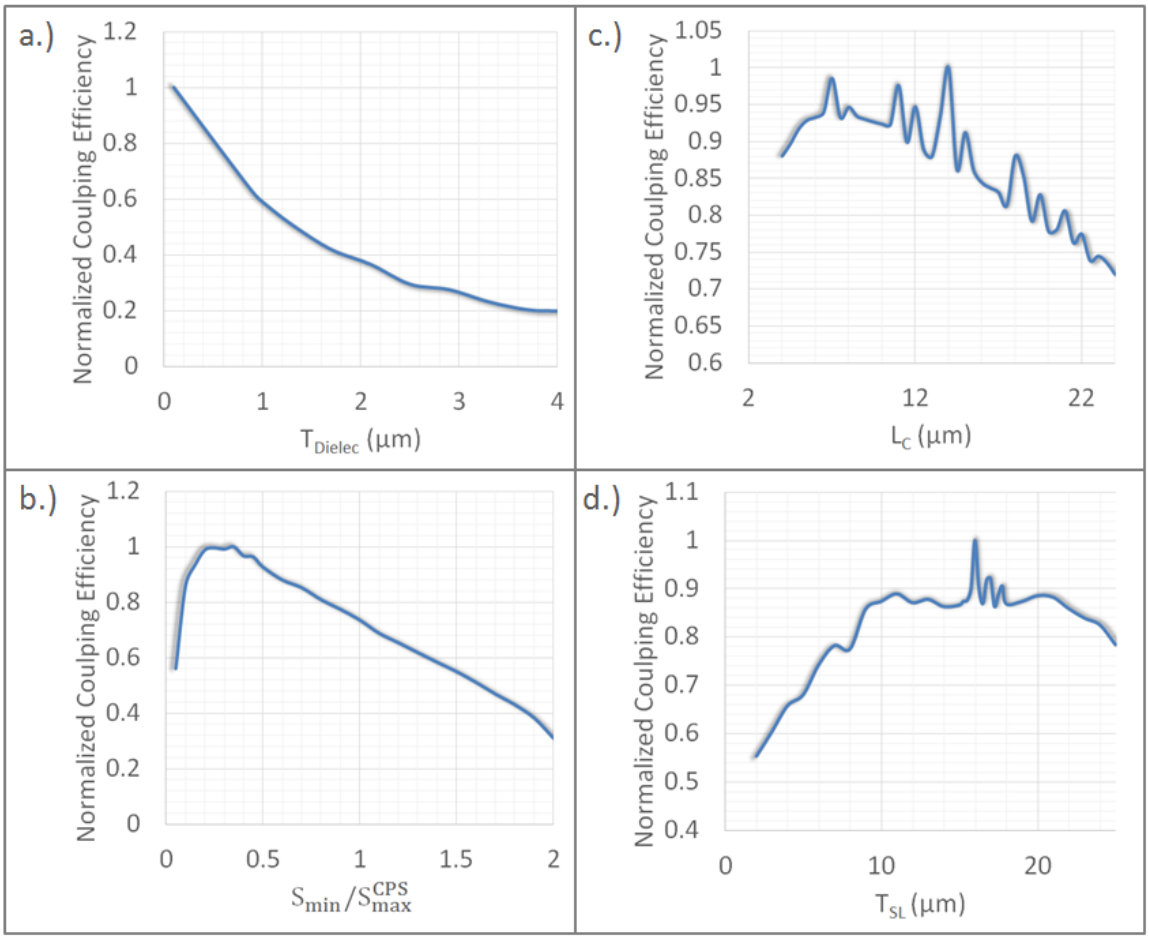

Figure 4.11: Coupling parameter optimization for 1 THz

Figure 4.11 plots the effect for each coupling parameter, the observed spikes correspond to frequency-dependent resonances. In CW THz, these spikes can be exploited to maximize coupling efficiency at a single wavelength. Here we are interested in the broadband pulse operation, therefore we are only concerned with the baseline coupling efficiency.

For the dielectric coating to operate as an anti-reflection coating we want $T_{dielec} = 131nm$. Referring to Figure 4.11a, we obtain high coupling efficiency for small values of T_{dielec} which coincides with our desired coating thickness.

Figure 4.11b plots the coupling efficiency as a function of the S_{min}/S_{max}^{CPS} ratio. To note, the maximum coupling efficiency does not occur when $S_{min}/S_{max}^{CPS} = 1$; instead, maximum coupling occurs closer to $S_{min}/S_{max}^{CPS} \approx 0.25$.

Figure 4.11c plots the coupling efficiency as a function of the coupling length, L_C. Varying the coupling length shows spikes in transmission profile; this occurs because

the coupling section acts as a matching waveguide (similar to an AR coating). When the propagation constant of the CPS waveguide, $\beta_{CPS} = n_e^{CPS} k_0$, becomes efficiently coupled to the thick slot waveguide, $\beta_{TSWG} = k_0$, a transmission peak will occur. Using the same concept as an AR coating, frequency-dependent transmission can be maximized if the coupling section has a propagation constant of $\beta_C = n_e^C k_0$ where $n_e^C = \sqrt{n_e^{CPS}}$ for an odd multiple of $\lambda_C/4$. We select $L_C \approx 10\mu m$ for the proof of concept.

Figure 4.11.d plots the coupling efficiency as a function of the thick slot waveguide's starting thickness, T_{SL}. As with the coupling length frequency-dependent peaks are visible; T_{SL} is selected in a similar manner to L_C by selecting the maximum baseline in the transmission spectrum. We select $T_{SL} \approx 15\mu m$ for the proof of concept.

4.2.4 Transmission Waveguide

Figure 4.12a illustrates a cross-section of the transmission waveguide constructed of copper. The waveguide is used to transfer the THz field in a low-loss state over a number of centimeters where it is free to interact with the surrounding medium (i.e. air). The waveguide type is not well-defined; depending on exact dimensions it falls in-between a slotline and parallel-plate waveguides.

Practically we are limited when selecting the conductor thickness (T); typical values for copper sheets are around $T \geq 400\mu m$. In Section 4.4.2 we will discuss our machining technique that utilizes a femtosecond laser, which imposes a restriction on the copper thickness, so, we select $T = 400\mu m$. Values for S are flexible; using laser machining we can achieve $20\mu m \leq S \leq 80mm$ accurately.

To select a viable $\frac{S}{T}$ ratio we need to analyze the loss (α). Existing analytic methods can be used to estimate α at the parallel-plate extreme of the structure, but above a certain threshold (when $0.2 < \frac{S}{T}$) the techniques become undefined. The thick slot waveguide was analyzed in Section 2.4.6 where Figure 2.32 plots the waveguide loss as function of $\frac{S}{T}$ throughout this undefined region.

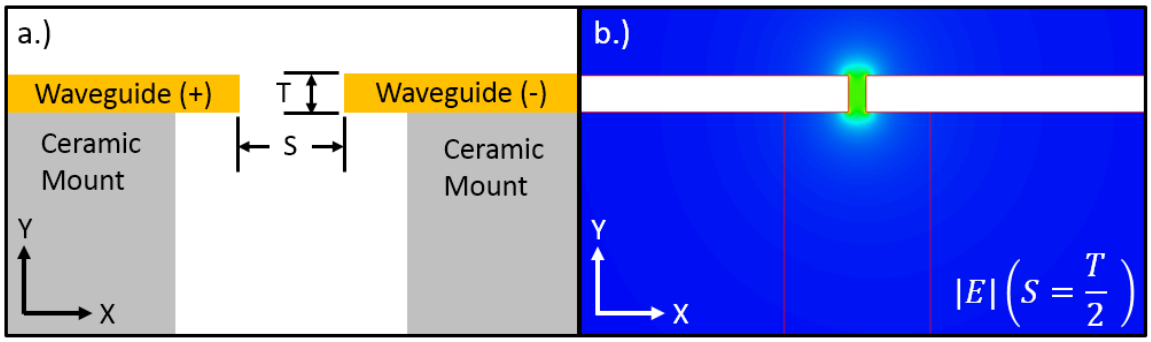

Figure 4.12: a.) Transmission waveguide in transverse plane b.) $|E|$ in a parallel-plate like configuration ($S = \frac{T}{2} = 200\mu m$)

For our experiments we will select S=0.4mm and T=0.4mm, referring to Figure 2.32 this corresponds to a waveguide loss of $\alpha \approx 0.3dB/cm$ at 1 THz.

4.2.5 Field Enhancer

The field enhancer is used to refocus the guided THz wave onto the THz detector. This is analogous to the receiver's HRFZ-Si focusing lens in a conventional THz-TDS setup. The key benefit of the field enhancer is discussed in [1]; paraphrased, it states the thick slot waveguide is not limited by diffraction, thus a larger localized field is focused onto the THz detector. The primary difference between [1] and here is that the field enhancer includes a H-plane field compression angle, also the excitation source is different. The addition of the H-plane compression angle does not significantly affect the field enhancement factor. FEM simulations revealed that a $\approx 30dB$ enhancement could still be obtained. Adiabatic compression of the field enhancer is necessary to ensure minimal back reflection into the transmission waveguide. The field enhancer is excited by a uniform wavefront. Therefore we should expect a higher back reflection than that observed in the experiments shown in [1] which was excited by a spherical wavefront with a matched convergence angle.

4.2.6 THz Detector

The THz detector is used for coherent detection of the wave generated by the THz source. The THz detector generates a current proportional to THz field and receiver conductivity [7]:

$$J(t) = \int_{-\infty}^{t} \sigma_s(t - t')E_{THz}(t')dt'. \tag{4.5}$$

Fourier transform:

$$\tilde{J}(\omega) = \tilde{\sigma}_s(\omega)\tilde{E}_{THz}(\omega) \tag{4.6}$$

Section 4.2.5 states the field enhancer is not limited by diffraction. Compared to a conventional THz-TDS setup which relies on THz optics we should expect an increase in detected current due to the enhanced localized field. Simulations have confirmed that the Field Enhancer provides gain similar to that reported in [1], therefore we can expect a ≈30dB field enhancement. Referring to Eqn. 4.6, a 30dB field enhancement will correlate to an increase of detected current, thus, improving the overall performance of the waveguide structure beyond that of a conventional THz-TDS system.

4.3 Experiments

The following sections illustrate the fabrication and testing methods.

4.4 Fabrication

Fabrication of the waveguide structure discussed in Section 4 requires a number of steps:

1. THz source and detector construction,
2. Copper waveguide construction.

This section will discuss each of these items in more detail.

4.4.1 THz source and detector construction

The THz source and detectors are constructed using the same method which comprises of the following steps:

1. Growth of LT-GaAs samples,
2. UV-photolithography,

3. Gold deposition and lift-off,

4. Femtosecond substrate cleaving,

5. PMMA coating.

Growth of LT-GaAs samples

A $3\mu m$ Low Temperature Grown Gallium Arsenide (LT-GaAs) layer is grown on a $0.5\mu m$ High Temperature Grown Gallium Arsenide (HT-GaAs) buffer layer (for smoothing) on a Semi-insulating Gallium Arsenide (SI-GaAs) substrate using Molecular Beam Epitaxy (MBE). The HT-GaAs layer is grown at $550°C$, then the LT-GaAs layer is grown at $234°C$. The wafer is then annealed in a Rapid Thermal Annealer (RTA) at $400°C$ for 39 minutes. Using these values we obtain a high resistivity and sub-picosecond carrier lifetime substrate, which is required for THz applications.

UV-photolithography

Ultraviolet (UV)-photolithography is used to pattern the metalization on the LT-GaAs substrate. Using this technique we can obtain feature sizes around $5\mu m$ which is suitable for our application. Alternatives, such as Electron Beam Lithography (EBL) or Focus Ion Beam (FIB) etching can be used if smaller feature sizes are desired.

The UV-photography process is described as follows: spin-coat the "positive" photoresist (AZ 5714E IR) at 4000rpm for 45 seconds onto the LT-GaAs wafer; softbake the photoresist for 60 seconds at 90°C; place the photomask onto the substrate and expose to UV light for 15 seconds; finally, develop for 1 minute and 40 seconds in a developer (AZ MIF 300) and then rinse with Deionized (DI) water.

Gold deposition and lift-off

Contact metalizations are added to the substrate using E-beam deposition. This process consists of placing the samples inside an E-beam evaporator chamber and then depositing an adhesion layer (5nm of titanium) followed by the metalization (100nm of gold). After deposition, the samples are removed from the deposition chamber and sonicated in an acetone bath to strip the metalization in select areas which results in the desired pattern.

Femtosecond substrate cleaving

Referring to Section 4.2.3, coupling between the THz source/detector and the transmission waveguide requires machining accuracy to the $10\mu m$ scale. This would be difficult to accomplish using a diamond scribe and imperfect mask alignment. We use a femtosecond laser to precisely cleave theLT-GaAs substrate along any crystal axis. This process is similar to the technique discussed in Section 4.4.2.

PMMA coating

PMMA is used to form the dielectric coating on the THz source and detector. According to [44], a ≈131nm layer requires a 3% 950PMMA Anisole solution to be spin-coated at 3500RPM for 45 seconds. After the substrate has been coated it is annealed on a hot-plate at 180°C for 5 minutes to provide a semi-rigid dielectric layer.

4.4.2 Copper waveguide construction

The a similar produce to the one documented in Section 3.4.1.

4.5 Equipment

We will discuss the equipment used in the proposed experimental evaluation.

Optical Source

The optical source is a PolarOnyx Mercury 780nm mode-locked fiber laser which is capable of outputting 50mW femtosecond ($<$ 100 fs) pulses at a repetition rate of 69.8MHz. We selected this laser in lieu of a standard Ti:Sapphire laser primarily because of practical reasons, such as smaller size, mechanical stability, lower cost, and simple turn-key operation.

The laser requirements in a THz system are governed by the photoconductive substrate material, which in our case is LT-GaAs. The laser wavelength must be less than the band-gap of substrate material ($E > 1.42eV$ or $\lambda < 871nm$).

The laser power is selected based on the optimization of THz output power which is a function of carrier-screening as explained in Section 2.1.2. In essence, the saturation induced by carrier-screening imposes a practical limit, which suggests that optical powers greater than 25mW do not result in appreciable gains in THz power [8].

The pulse width is selected to provide a broad spectrum of frequencies that extend into the THz region. To estimate of the spectral bandwidth of an unchirped Gaussian pulse one can divide the Gaussian time-bandwidth product (≈ 0.44) by the pulse width. For example, a 100 fs pulse can have up to $\Delta f \approx 0.44/100fs = 4.4THz$ of bandwidth.

The laser pulse repetition rate is determined by the round trip time of the resonator. The repetition rate of the laser is important to the system because it relates the average power to the peak power. For example, an average power of $P_{avg} = 50mW$ with a pulse width of $\tau_p = 100fs$ at a repetition rate of $f_{rep} = 69.8MHz$ results in a peak power of:

$$P_{peak} = 0.94\frac{P_{avg}}{f_{rep}\tau_p} = 0.94\left(\frac{50mW}{69.8MHz \times 100fs}\right) = 6.73kW, \tag{4.7}$$

where the 0.94 factor accounts for an assumed Gaussian pulse shape.

Lock-in Amplifier

A Stanford SR830 lock-in amplifier is used to detect the current induced by the THz signal in the receiver. In essence a lock-in amplifier is a frequency selective voltmeter or ammeter which is capable of measuring small signals (pV/pA range) which exist below the noise floor. To detect these small signals the lock-in amplifier utilizes a Phase Sensitive Detector (PSD) which operates on the principle of orthogonality [45]:

$$A_1A_2\int_0^T sin(\omega_1 t)sin(\omega_2 t)dt = 0, \quad \text{for} \quad \omega_1 \neq \omega_2. \tag{4.8}$$

Using orthogonality it becomes apparent that a "filter" can be designed providing that we mix two signals; for example, an experimental signal, $\omega_S = \omega_1$, and a reference signal, $\omega_R = \omega_2$. When the experimental signal is mixed with the reference signal a DC output proportional to the product will exist only when the two frequencies are identical.

PSDs are used in place of a typical bandpass filters because they are capable of achieving much higher Q-factors. For example, a high quality bandpass filter is capable of Q=100, whereas a PSD can accomplish frequency filtering equivalent to Q=1000000 [45]. The detection window is small enough that only the signal and a very small portion of the noise passes. At this point amplification can be applied because the Signal to Noise Ratio (SNR) has been significantly enhanced.

Software

The UVic Terahertz Spectrometry software (Figure 4.13) was written to control the interaction between 3 main components: the Thorlabs PT1-Z8 delay line, the National Instruments GPIB USB-HS device, and the Stanford SR830 lock-in amplifier. The goal of writing this software was to provide a simple 1-click operation that would coordinate the component interaction allowing for quick and accurate results.

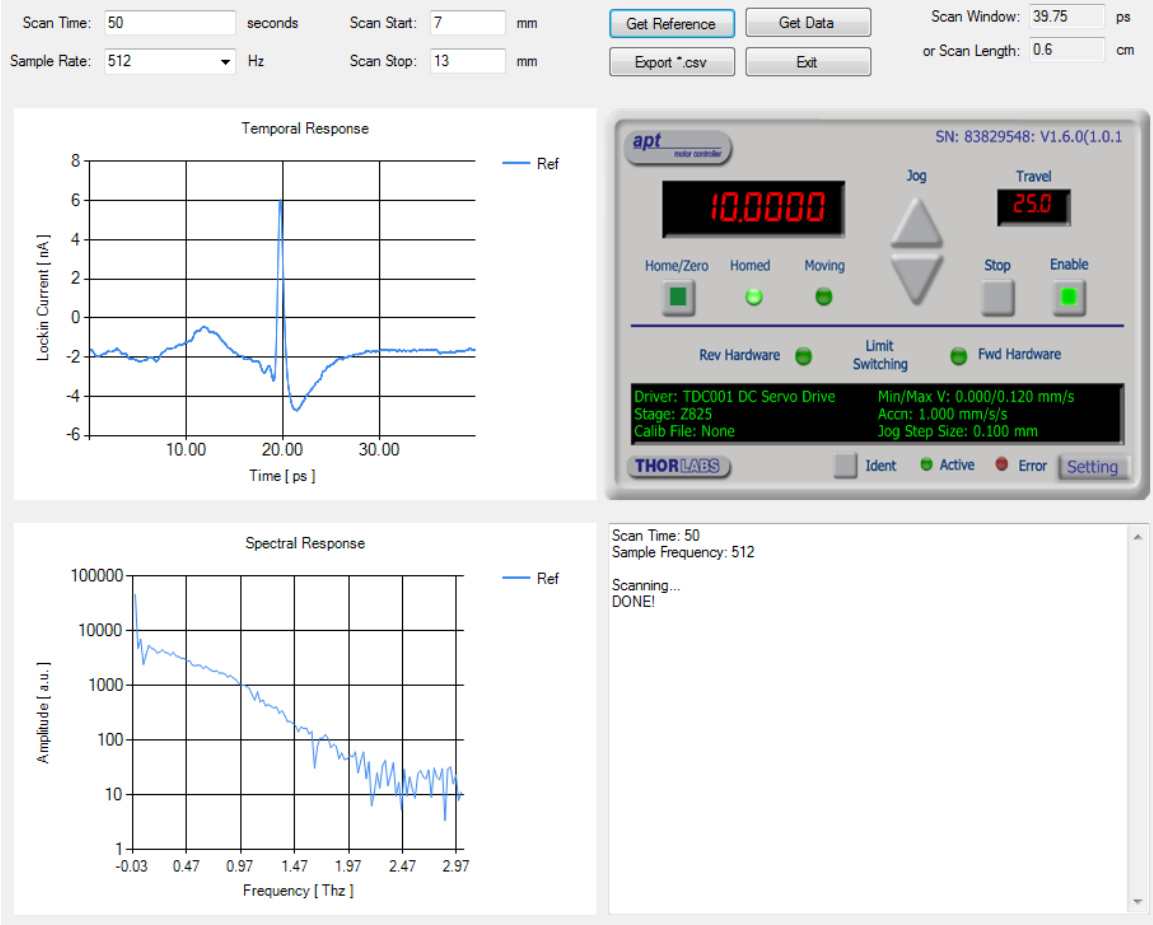

Figure 4.13: UVic THz Spectrometry Software Interface

The software was written in C++/CLI to allow for a simple integration onto other systems by using redistributable files and the managed .NET framework. At a high level the software operates quite simply by interfacing with the delay line through Thorlabs ActiveX controls and dlls. The interface with the lock-in amplifier requires GPIB drivers and dlls to handled. After all the connections are made the program calculates velocities, reads/writes data, and calculates the spectral response using the

FFT.

4.6 Terahertz Spectroscopy

A typical Terahertz Time Domain Spectroscopy (THz-TDS) setup which shares many similarities with the setup required for testing the waveguiding structure. The THz-TDS setup illustrated in Figure 4.14 consists of passive optical components (lenses, mirrors, and beam splitter), active components (laser, delay line, and THz PCAs), and electronic components (function generator, lock-in amplifier, and computer).

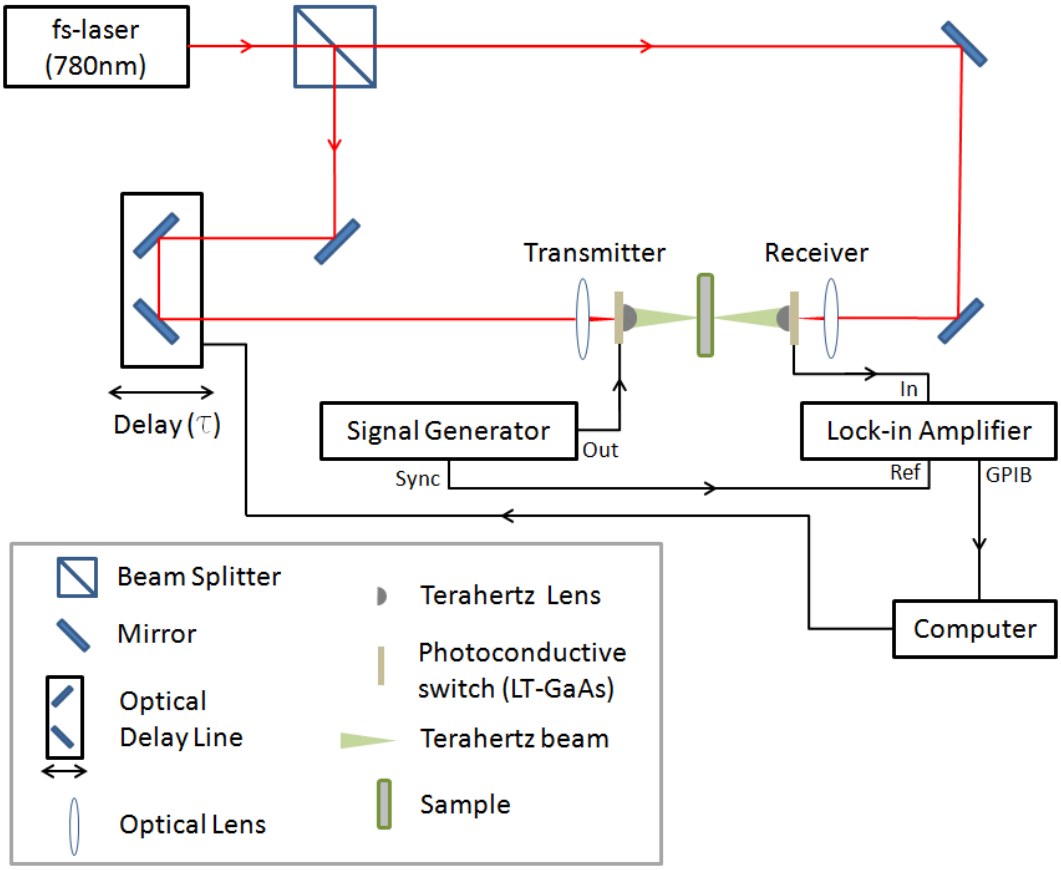

Figure 4.14: THz Spectroscopy Setup

The setup can be described as follows: the optical source (femtosecond laser) emits a beam which gets split into two separate paths; one for the transmitter PCA, the other for the receiver PCA. The transmitter path beam is used to generate the THz pulse; the receiver beam path is used to gate the receiver PCA, which allows for

coherent detection of the THz E-field. The E-field is plotted by linearly sweeping the physical position of the delay line in the transmitter path. This process results in a shift between the received THz pulse and the receiver's gating pulse.

4.7 Waveguide Testing

The waveguide operates on a similar principle to conventional THz spectroscopy, thus the experimental setup is similar. Figure 4.15 illustrates the setup used for testing the waveguide.

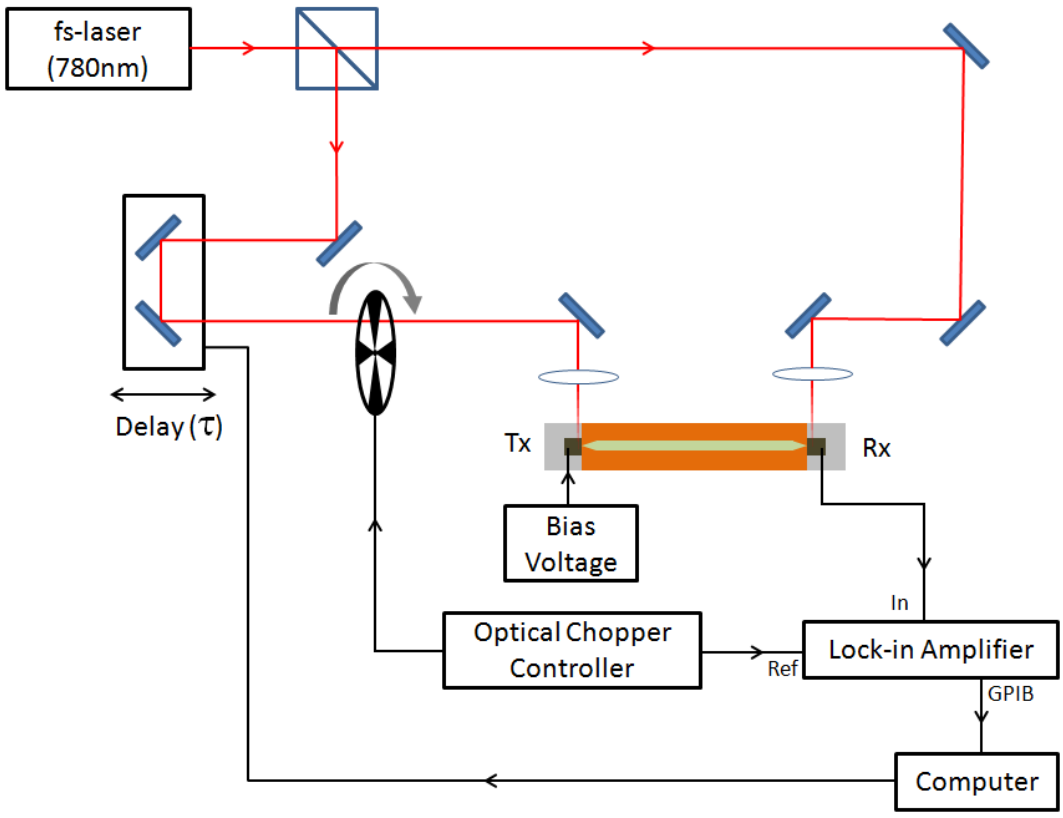

Figure 4.15: THz Waveguide Setup, for illustration purposes the waveguide is incorrectly orientated, realistically it should be rotated by 90° such that the excitation plane is normal to the incident laser beam

The primary difference between a conventional THz-TDS setup and the waveguide setup is the addition of the waveguide. An optical chopper is used in place of a signal generator because the low-frequency (1-10kHz) pulse train can saturate the lock-in amplifier. This occurs because the waveguide electrically connects the signal generator

to the sensitive lock-in amplifier current input. A conventional THz-TDS setup has no electrical connection between the transmitter and receiver therefore posing no issue. The optical chopper technique could be used in a conventional THz-TDS setup, but it is less convenient so a signal generator is commonly used.

4.8 Evaluation and Analysis

The chapter will investigate the performance of the in-plane waveguide introduced in Section 4.2. Evaluation of the in-plane waveguide includes a time-domain simulation illustrating the structure's performance as well as an experimental comparison against a typical THz-TDS system.

4.9 Simulation

The simulation of the in-plane THz waveguide is accomplished using Ansys HFSS. The transient simulation approximates reality by generating a broadband pulse as the excitation source. This provides insight into the wave parameters and coupling losses. The simulations in this section evaluate the performance of the entire structure as opposed to the individual components.

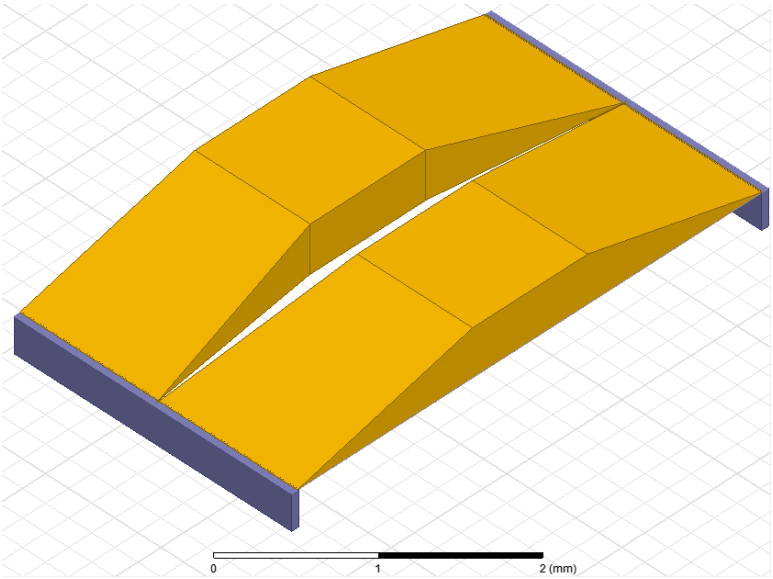

Figure 4.16: Simulated Structure

Figure 4.16 illustrates the simulated in-plane THz waveguide. The dimensions of the simulated structure are to scale with the exception of the thick slot waveguide length which was truncated from ≈ 4cm to 1mm. The truncation was implemented to reduce the simulation time. Referring to Figure 2.32, for S/T = 1, the loss is 0.3dB/cm. Therefore the implemented truncations should not significantly deviate the results from reality as the loss is already minimal.

Referring to the dimensions discussed in Section 4.2, the in-plane THz waveguide includes a large range of feature sizes (5 μm to 4 cm). To account for the broad range of feature sizes, user-defined meshing is required in the source and detector regions. Also, first-order basis functions were utilized to provide accurate solutions across a broad range of mesh element sizes. Substrate material parameters were specified using data obtained from [46], where $n_{GaAs} \approx 3.6$ and $\tan\delta \approx 0.0008$. The conductivity of the copper was set at $5.96 \times 10^7 S/m$.

Figure 4.17 illustrates the E-field of the propagating broadband pulse at different time steps. The pulse is generated at the current source illustrated in Figure 4.17a and detected at the load in Figure 4.17f.

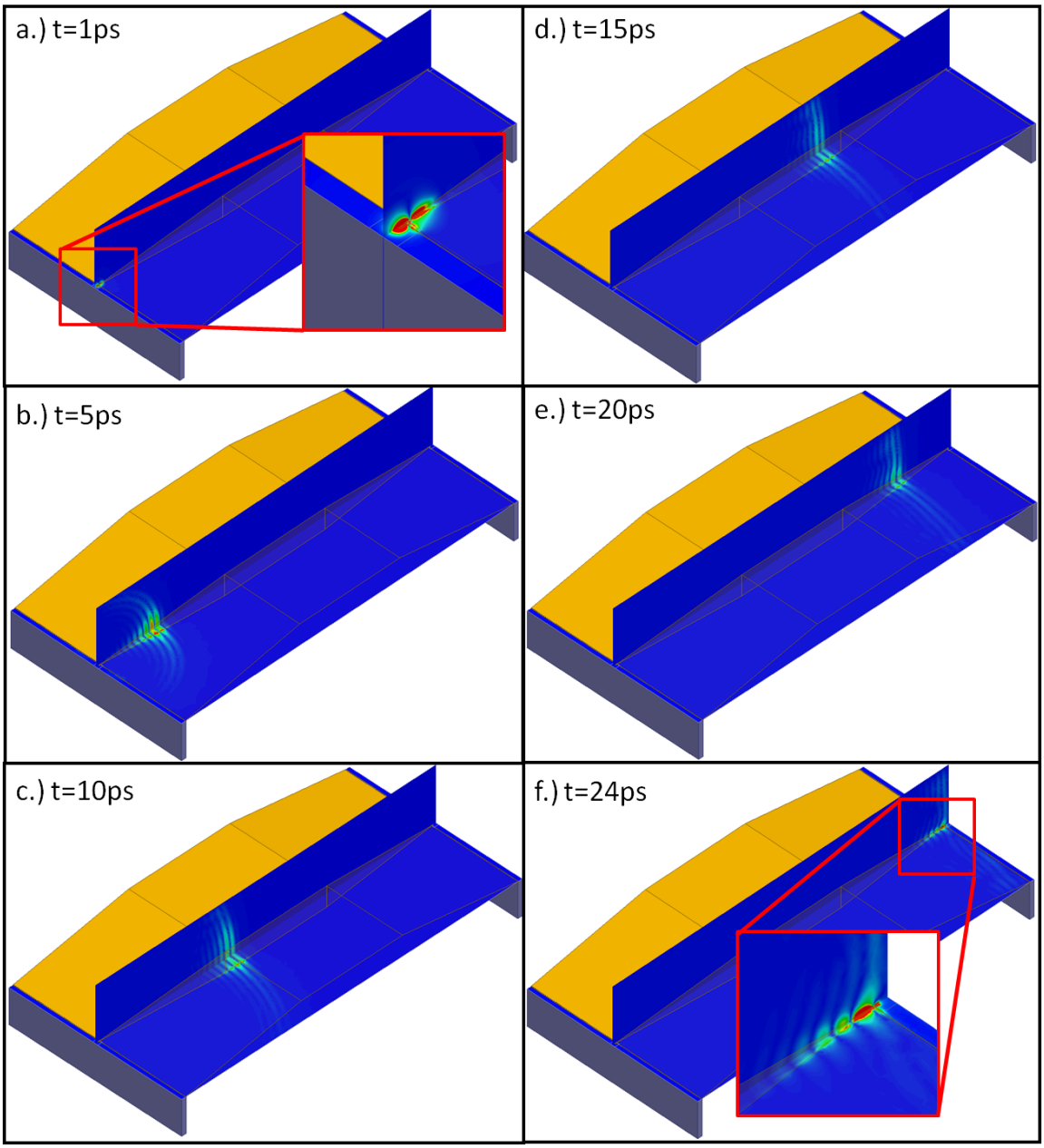

Figure 4.17: DGTD simulation illustrating E-field for broadband pulse propagation for the in-plane waveguide. a.) $\rightarrow$ f.) illustrate the pulse at different time steps

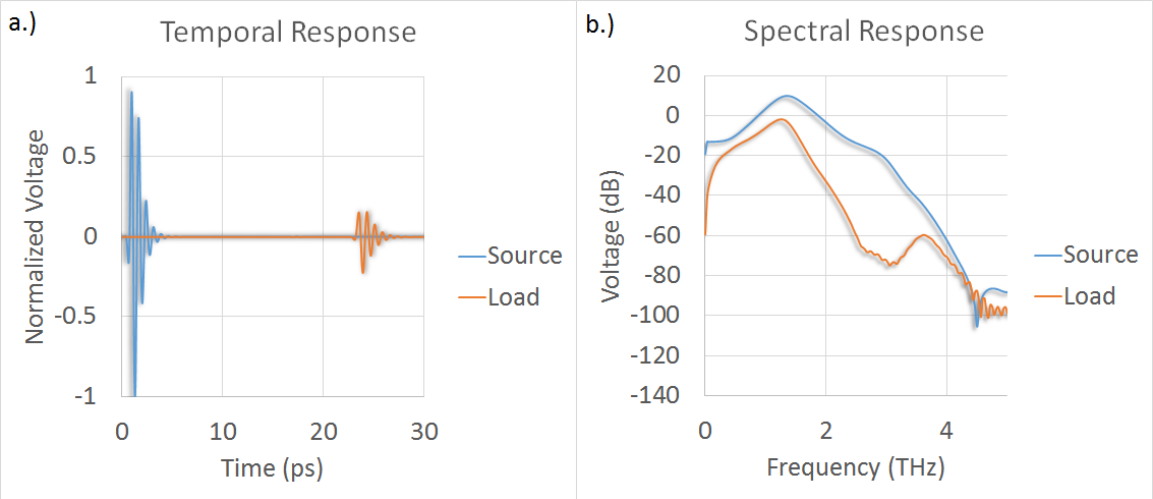

Figure 4.18: THz Pulse and Spectrum

Figure 4.18 plots the temporal and spectral profile of the pulse at the source and load. The difference between the spectral shapes are used to determine the overall performance of the system. The frequency-dependent loss ranges from 10-50dB where Figure 4.19 plots the relative contributions. We would like the loss to be low across the entire frequency range, but in practice this is difficult to achieve in a pulsed application. The analysis presented in Section 4.2 analyzed the waveguide using a single frequency source at 1 THz, this is not the case when the excitation source is a broadband THz pulse.

Figure 4.19 illustrates that the majority of the loss occurs from the field enhancer. This loss occurs due to modal back reflections during the field compression. This loss can be mitigated using engineering techniques that suppress the reflected waves. For the purpose of this thesis, this will be left as future work because the primary goal of this document is to illustrate the feasibility of in-plane coupling.

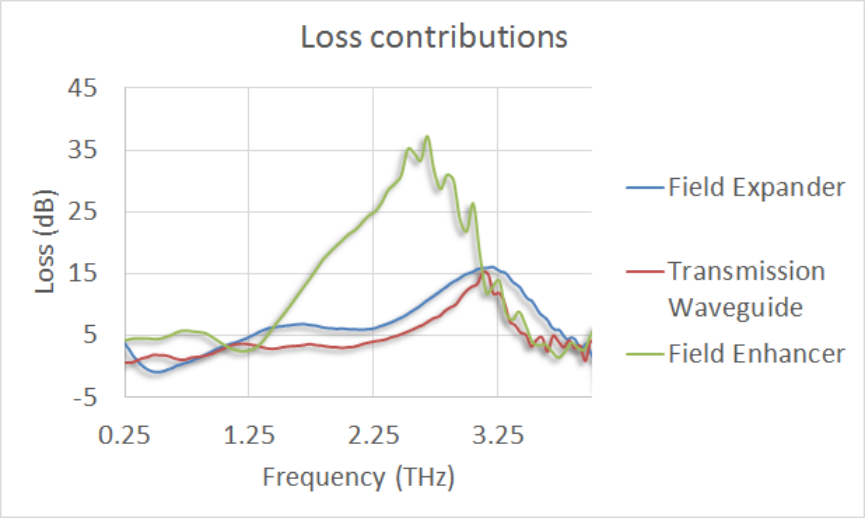

Figure 4.19: THz in-plane waveguide loss contributions

The simulation results adequately illustrate the concept of in-plane coupling to a thick slot waveguide. The total loss between 0.3 - 1.5 THz ranges from 5 - 13 dB which illustrates an enhancement over a perfectly aligned PCA THz-TDS setup.

The concept of in-plane coupling to a thick slot waveguide can be engineered to provide a different frequency response dependent on the thick slot conductor geometry. In-plane resonators and filters can be implemented into the thick slot waveguide using existing microwave engineering and femtosecond laser micromaching.

4.10 Conclusion

In-plane photoconductive coupling to a thick slot waveguide for low-loss transmission was demonstrated using Discontinuous Galerkin Time Domain (DGTD) simulation. In-plane coupling offers advantages over conventional THz-TDS systems for a number of reasons: simplified optical and THz beam alignment, super-focusing of THz beam, low-loss operation, minimal pulse dispersion, mechanical stability, frequency selective engineering possibilities, and system implementation feasibility.

For this thesis, in-plane photoconductive coupling to a thick slot waveguide was engineered to provide a proof of concept. Only basic optimizations were implemented and geometries were selected to be functional. The techniques developed in Section 4.2 are not ideal for all applications, but serve as a starting point for operation around 1 THz.

4.10.1 Future Work

By demonstrating the feasibility of in-plane photoconductive coupling to a thick slot waveguide many potential applications can be examined. Ultimately, the most important future work is the experimental evaluation of the structure.

The work presented in this thesis was focused on demonstrating feasibility; future work will involve optimization for specific applications. For example, spectroscopic characterization of molecules is dependent on detecting trace signatures at specific frequencies. Therefore the waveguide can be optimized to provide maximum sensitivity within a given range of frequencies for detection of a specific molecule.

Other future work addresses system implementation challenges. In comparison to conventional THz-TDS systems (which utilize PCAs), in-plane photoconductive coupling can be implemented into a more rugged system. This thesis utilized free-space optical excitation for convenience, but optical excitation can be achieved using fiber optic coupling to remove most of the alignment difficulties.

The analytic framework for component, and component interfaces needs to be fully developed. To the author's knowledge, the thick slot waveguide for THz applications has not been investigated analytically, but thick conductor slotlines have been investigated in [36].

To the author's knowledge, in-plane photoconductive coupling to a thick slot waveguide has not been previously demonstrated. A wealth of future possibilities exist, not all of which have been mentioned here.

Chapter 5

Summary

This thesis investigated the idea of Terahertz (THz) field transformations using tapered thick slot waveguides.

Chapter 3 examined THz field enhancement using radiative excitation from a PCA to a thick slot waveguide. The primary conclusions drawn from this chapter were that the overall field enhancement outweighs the detriment of the insertion loss. Further concluding statements from this chapter can be found in Section 3.6.

Chapter 4 investigated the new idea of in-plane photoconductive coupling to a thick slot waveguide using simulation. Conclusions drawn from this chapter reveal that the excitation technique and coupling mechanism allow for highly efficient THz waveguides. Further concluding statements from this chapter can be found in Section 4.10.

Literature Cited

[1] R. Smith, F. Ahmed, A. Jooshesh, J. Zhang, M. Jun, and T. Darcie. Thz field enhancement by antenna coupling to a tapered thick slot waveguide. *Journal of Lightwave Technology*, 32:15878, 2014.

[2] Ansys HFSS 13, http://www.ansys.com/.

[3] R. Paschotta. *Encyclopedia for Photonics and Laser Technology.* Wiley, 2014.

[4] E. Brown, F. Smith, and K. McIntosh. Coherent millimeter-wave generation by heterodyne conversion in low-temperature-grown gaas photoconductors. *Journal of Applied Physics*, 73:1480, 1993.

[5] I. Gregory, C. Baker, W. Tribe, I. Bradley, M. Evans, E. Lindfield, A. Davies, and M. Missous. Optimization of photomixers and antennas for continuous-wave terahertz emission. *IEEE Journal of Quantum Electronics*, 41:717–728, 2005.

[6] X. C Zhang and J Xu. *Introduction to THz Wave Photonics.* Springer, 2010.

[7] Y-H Lee. *Principles of Terahertz Science and Technology.* Springer, 2009.

[8] M. Tani, S. Matsuura, K. Sakai, and S.I. Nakashima. Emission characteristics of photoconductive antennas based on low-temperature-grown GaAs and semi-insulating GaAs. *Applied Optics*, 36:7853–7859, 1997.

[9] E. Castro-Camus, J. Lloyd-Hughes, and M. Johnston. Three-dimensional carrier-dynamics simulation of terahertz emission from photoconductive switches. *Physical Review B: Condensed Matter and Materials Physics*, 71:195301, 2005.

[10] D. Pozar. *Microwave Engineering, 4rd edition.* Wiley, 2011.

[11] A. Yariv and P. Yeh. *Photonics: Optical Electronics in Modern Communications.* Oxford University Press, 2007.

[12] P. Parsad. *Introduction to Biophotonics*. Wiley, 2003.

[13] R. Mendis and D. Grischkowsky. Undistorted guided-wave propagation of subpicosecond terahertz pulses. *Optics Letters*, 26:846–848, 2001.

[14] M. Nagel, PH. Bolivar, and H. Kurz. Modular parallel-plate thz components for cost-efficient biosensing systems. *Semiconductor Science and Technology*, 20:S281S285, 2005.

[15] S. Coleman and D.Grischkowsky. Parallel plate thz transmitter. *Applied Physics Letters*, 84:654–656, 2004.

[16] K. Gupta, R. Garg, I. Bahl, and P. Bhartia. *Microstrip Lines and Slotlines, 2nd Ed.* Artech House, 1996.

[17] J. Lee. Slotline impedance. *IEEE Transactions on Microwave Theory and Techniques*, 39:666–672, 1991.

[18] G. Ghione. A CAD-oriented analytical model for the losses of general asymmetric coplanar lines in hybrid and monolithic mics. *IEEE Transactions on Microwave Theory and Techniques*, 41:1499–1510, 1993.

[19] N. Das. Characteristics of modified slotline configurations. In *Microwave Symposium Digest*, pages 777–780, 1991.

[20] R Crampagne and G. Khoo. Synthesis of certain transmission lines employed in microwave integrated circuits. *IEEE Transactions on Microwave Theory and Techniques*, 25:440–442, 1977.

[21] D.S. Phatak. Dispersion characteristics of optically excited coplanar striplines: comprehensive full-wave analysis. *IEEE Transactions on Microwave Theory and Techniques*, 38:1719–1730, 1990.

[22] M. Wachter, M. Nagel, and H. Kurz. Metallic slit waveguide for dispersion-free low-loss terahertz signal transmission. *Applied Physics Letters*, 90:061111, 2007.

[23] H. Zhan, R. Mendis, and DM. Mittleman. Superfocusing terahertz waves below $\lambda/250$ using plasmonic parallel-plate waveguides. *Optics Express*, 18:9643–9650, 2010.

[24] K. Iwaszczuk, A. Andryieuski, A. Lavrinenko, X.-C. Zhang, and P.U. Jepsen. Terahertz field enhancement to the MV/cm regime in a tapered parallel plate waveguide. *Optics Express*, 20:8344–8455, 2012.

[25] Hui Zhan, Rajind Mendis, and Daniel M. Mittleman. Characterization of the terahertz near-field output of parallel-plate waveguides. *JOSA B*, 28:558–566, 2011.

[26] J. Zhang and D. Grischkowsky. Adiabatic compression of parallel-plate metal waveguides for sensitivity enhancement of waveguide thz time-domain spectroscopy. *Applied Physics Letters*, 86:061109, 2005.

[27] A. Shutler and D. Grischkowsky. Gap independent coupling into parallel plate terahertz waveguides using cylindrical horn antennas. *Journal of Applied Physics*, 112:073102, 2012.

[28] Batop, www.batop.com, last accessed on August 2014.

[29] H. Kanaya, H. Shibayama, R. Sogabe, S. Suzuki, and M. Asada. Fundamental oscillation up to 1.31 thz in resonant tunneling diodes with thin well and barriers. *Applied Physics Express*, 5, 2012.

[30] H. Pahlevaninezhad, T. Darcie, and B. Heshmat. Two-wire waveguide for terahertz. *Optics Express*, 18:7415–7420, 2010.

[31] H.Pahlevaninezhad, B.Heshmat, and T. Darcie. Efficient terahertz slot-line waveguides. *Optics Express*, 19, 2011.

[32] K. Wong. *Planar Antennas for Wireless Communications*. Wiley, 2002.

[33] Hamid Pahlevaninezhad. *Design and implementation of efficient terahertz waveguides*. PhD thesis, University of Victoria, 2012.

[34] H. Pahlevaninezhad, B. Heshmat, and T. Darcie. Advances in terahertz waveguides and sources (invited paper). *IEEE Photonics Journal, Brakethrough in Photonics*, 3:307–310, 2011-2012.

[35] B. Vidal, T. Nagatsuma, N. Gomes, and T. Darcie. Photonic technologies for millimeter- and submillimeter-wave signals. *Advances in Optical Technologies*, 2012.

[36] T. Kitazawa. Slotline with thick metal coating. *IEEE Transactions on Microwave Theory and Techniques*, 21:580–582, 1973.

[37] HITRAN, http://www.cfa.harvard.edu/hitran/.

[38] R. Mendis and DM. Mittleman. Comparison of the lowest-order transverse-electric (TE1) and transverse-magnetic (TEM) modes of the parallel-plate waveguide for terahertz pulse applications. *Optics Express*, 17:14839–14850, 2009.

[39] R. Mendis and D. Grischkowsky. Plastic ribbon thz waveguides. *Journal of Applied Physics*, 88:4449, 2000.

[40] H. Han, H. Park, M. Cho, and J. Kim. Terahertz pulse propagation in a plastic photonic crystal fiber. *Applied Physics Letters*, 80:2634, 2002.

[41] K. Wang and D. Mittleman. Metal wires for terahertz wave guiding. *Nature*, 432:376–379, 2004.

[42] T. Jeon, J. Zhang, and D. Grischkowsky. Thz sommerfeld wave propagation on a single metal wire. *Applied Physics Letters*, 86:161904, 2005.

[43] M. Exter and D. Grischkowsky. Characterization of an optoelectronic terahertz beam system. *IEEE Transactions on Microwave Theory and Techniques*, 38:1684–1690, 1990.

[44] Microchem. *NANO^{TM}PMMA and Copolymer Data Sheet*, 2001.

[45] Model SR830 DSP Lock-In Amplifier. Technical report, Stanford Research Systems, 2011.

[46] D. Grischkowsky, S. Keiding, M. Exter, and C. Fattinger. Far-infrared time-domain spectroscopy with terahertz beams of dielectrics and semiconductors. *JOSA B*, 7:2006–2015, 1990.